UNIVERSITY OF SOUTHAMPTON

FACULTY OF PHYSICAL AND APPLIED SCIENCES

School of Physics and Astronomy

Hybrid nanomaterials for novel photonic devices

by

Peristera Andreakou

Thesis for the degree of Doctor of Philosophy

May 2012

UNIVERSITY OF SOUTHAMPTON

FACULTY OF PHYSICAL AND APPLIED SCIENCES

School of Physics and Astronomy

ABSTRACT

Doctor of Philosophy

HYBRID NANOMATERIALS FOR NOVEL PHOTONIC DEVICES

By Peristera Andreakou

This PhD thesis investigates the optical properties of colloidal semiconductor nanocrystals and evaluates concepts regarding the development of novel photonic devices. Spectroscopic studies of the exciton dynamics in colloidal lead sulfide (PbS) quantum dots (QDs) by tuning the temperature are presented. The lowest exciton splitting for a range of PbS QDs sizes is calculated and a transfer of the oscillator strength from dark to bright states as the size increases is demonstrated. Hybrid structures with PbS QDs deposited on silicon substrates were also studied in order to explore whether excitons can be created in this material by means of resonant energy transfer.

Furthermore, elongated asymmetric cadmium selenide/cadmium sulfide (CdSe/CdS) quantum rods are used as gain medium for the development of whispering gallery mode microlasers. Single-mode operation of hybrid lasers based on colloidal CdSe/CdS core/shell QRs in silica microspheres is for the first time reported. Laser-emission tunability over a range of 2.1 nm is also demonstrated, by heating the microsphere cavity with a 3.5-μm laser.

In the last part of this thesis, unstructured and micro-structured $LiNbO_3$ are presented as excellent substrates for cell culture. Two commonly used neuron-like cells have been successfully proliferated and differentiated on both polar (±z) faces of $LiNbO_3$ crystal substrates. Spatially selective attachment of neuron-like cells onto the domain engineered micro-structured substrates is also shown, providing the opportunity for the development of functional materials for the study of neuronal networks.

UNIVERSITY OF SOUTHAMPTON

Notice of Intention to Submit a Research Thesis

All candidates are required to give at least 2 months' notice of their intention to submit a thesis (4 months' notice for candidates in the accredited colleges). Students wishing to graduate in person in July must give notice no later than 31 January.

I wish to give notice of my intention to submit a thesis for the degree of PhD

NAME OF CANDIDATE: Peristera Andreakou

SCHOOL: School of Physics and Astronomy

FACULTY: Faculty of Physical and Applied Sciences

MAIN SUPERVISOR: Prof. Pavlos Lagoudakis

TITLE OF THESIS: Hybrid nanomaterials for novel photonic devices

SIGNATURE: **DATE:** 12/05/2012

Acknowledgements

First and foremost, I would like to thank Prof. Pavlos Lagoudakis for the opportunity that he gave to me to come in UK and do my PhD using state of the art equipment. I am also grateful for the long nights and weekends that he spend with me in the lab transferring all his knowledge to me.

I am also obliged to Dr. Liberato Manna for the fabrication of CdSe/CdS quantum rods, as well as to Dr. Gerasimos Konstantatos and Dr. Maria Bernechea for the fabrication of PbS quantum dots. I am also pleased to Dr. Pengfei Wang, Dr. Ming Ding and Dr. Gilberto Brambilla for the fabrication of silica microsphere and fiber tapers. I would also like to thank Dr. Sakellaris Maillis for providing the lithium niobate substrates and Dr. Tracey Newman for introducing me to neuroscience world.

I am greatly indebted to my colleagues and specifically I would like to mention Dr. Christos Grivas, Mael Brossard, Junis Rindermann and Elena Kammann for the joyful hours working together until very late at night and the useful conversations we had about physics. My most heartfelt thanks go to my other colleagues Dr. Maria Maragkou, Dr. Peter Eldridge, Dr. Stefan Rohrmoser, Dr. Chunyong Li, Alexis Askitopoulos (for the free cigarettes ☺) and the other members of the group: Dr. Alaister Grundy, Dr. Hamid Ohadi, Nikolo Somachi, David English, Caryl Richard, Paqualle Cilibrizzi and Giuseppe Buscemi.

I would also like to thank Father Vasileios and Father Bartholomeos and my Greek friends Tassoula, Agathi, Giorgos, Ioanna, Alexandros, Simeon, Dimitrios, Athina, Areti, Georgia and etc for their support and being all the time next to me, even if I was always busy. I am pleased to my housemate and friend Lorena Pinilla for helping me so much the last months of my PhD and taking care my nutrition.

I must also thankful to my family and especially my parents for their support and for reminding me what is really meaningful in life. Last but not least, I am grateful to Thomas Esterle for his endless love and his magic way of putting colour and happiness into my life.

List of Publications

[1] "*Micro-structured ferroelectric substrates for neuro-photonics*",
P. Andreakou, S. Mailis, S. Sanchez, Y. J. Ying, S. Hands, T. A. Newman, and P. G. Lagoudakis, Oral presentation, EMRS 2012 Spring Meeting, Strasbourg, France, May 14 - May 18, 2012.

[2] "*Resonance energy transfer from PbS colloidal quantum dots to bulk silicon: A new aspect for hybrid photovoltaics*",
P. Andreakou, M. Brossard, M. Bernechea, G. Konstantatos, P. G. Lagoudakis, Oral presentation, EMRS 2012 Spring Meeting, Strasbourg, France, May 14 - May 18, 2012.

[3] "*Resonance energy transfer from PbS colloidal quantum dots to bulk silicon: The road to hybrid photovoltaics*",
P. Andreakou, M. Brossard, M. Bernechea, G. Konstantatos, P. G. Lagoudakis, Oral presentation, SPIE Photonics West, San Francisco, US, 21-26 January 2012.

[4] "*Tunable Near Field Dipole-Dipole Coupling Between CdSe/CdS Nanorods*",
P. Andreakou, J. J Rindermann, M. Zanella, L Manna, P. G. Lagoudakis, Poster presentation, *2011 Conference on Lasers & Electro-Optics Europe & 12th European Quantum Electronics Conference (CLEO EUROPE/EQEC)*, Munich, Germany, 22-26 May 2011.

[6] "*Tunable Near Field Dipole-Dipole Coupling Between CdSe/CdS Nanorods*",
P. Andreakou, S. Hands and P. G. Lagoudakis, Poster presentation, 2011 Conference on Lasers & Electro-Optics Europe & 12th European Quantum Electronics Conference (CLEO EUROPE/EQEC), Munich, Germany, 22-26 May 2011.

[7] "*Colloidal nanoprobe for the optical detection of ethanol*",
P. Andreakou, S. Hands and P. G. Lagoudakis, Poster presentation, EMRS 2008 Spring Meeting, Nice, France, 9-12 May 2011.

[8] "*Micro-structured ferroelectric substrates for neuro-photonics*",
P. Andreakou, S. Mailis, S. Sanchez, Y. J. Ying, S. Hands, T. A. Newman, P. G. Lagoudakis, submitted in the Applied Physics Letters.

[9] "*Detection of ultra-low refractive index variations with colloidal nanoprobes*",
P. Andreakou, S. Hands, P. G. Lagoudakis, Sensor & Actuator B 171-172, 1269-1271 (2012).

[10] "*Size and temperature dependent carrier dynamics in oleic acid capped PbS quantum dots*",
P. Andreakou, M. Brossard, M. Bernechea, G. Konstantatos, P. G. Lagoudakis, accepted in the Journal of Physical Chemistry C.

[11] "*Resonance energy transfer from PbS colloidal quantum dots to bulk silicon: The road to hybrid photovoltaics*",
P. Andreakou, M. Brossard, M. Bernechea, G. Konstantatos, P. G. Lagoudakis, SPIE proceeding, Paper No 8256 – 55, (2012).

[12] "*Hybrid lasers based on CdSe/CdS core/shell colloidal quantum rods on silica microspheres*",
C. Grivas, P. Andreakou, P. Wang, M. Ding, G. Brambilla, L. Manna, P. G. Lagoudakis, submitted in Nature Communications.

Table of Contents

List of Figures

List of Tables

Chapter 1: Introduction

Semiconductor nanocrystals are nano-crystalline particles that contain hundreds to thousands atoms with a lattice structure that is similar to the structure of the corresponding bulk semiconductor [1]. Semiconductor nanocrystals can be fabricated by wet-chemistry techniques (colloidal nanocrystals) and can have different sizes and shapes such as spherical (quantum dots), elongated (quantum rods) or more complex structures, like tetrapods [2,3]. Through the fabrication process, different materials can be combined leading to nanoscale heterostructured particles [2]. These heterostuctures allow the manipulation of electron and hole wavefunctions and consequently provide a method for engineering desired optical and electrical properties in the nanoscale level [1].

The size of colloidal semiconductor nanocrystals is comparable to the exciton natural spatial extension (Bohr radius a_B) with confinement being induced in three dimensions [4]. In this case, the electronic energies depend on the spatial confinement of the electronic wavefunctions, and consequently, on the size of the nanocrystals [1]. This effect provides tuneable electronic transitions that cover a wide spectral range from near infrared to visible. Due to the confinement, nanocrystals also exhibit discrete electronic transitions, which lead to a very narrow emission spectrum.

The last decade, a large amount of research has been devoted in understanding the size and shape dependence of their physical properties in order to potentially design and fabricate assembly of materials and devices with predictable behavior [5-12]. Potential applications of these materials include photovoltaics [13-15], light emitting diodes (LED) [16,17], photodetectors [18-21], gain material for microlasers [22], labeling and sensing of complex biological substances [23-28]. This PhD thesis discusses about the use of colloidal semiconductor nanocrystals in photovoltaics and microlasers and hence, a discussion about the state-of-the-art in these fields is also presented. A short review on nanomaterials and their potential use for interfacing electrical cell activity is included, as well.

1.1 Photovoltaic devices based on colloidal semiconductor nanocrystals

Conversion of solar energy to power in a material system can be divided into three physical fundamental steps [29]. Firstly, the material should absorb the solar photons and excitons should

thus be efficiently created into the material. Secondly, the exciton should be separated to individual hole and electron carriers, and thirdly the carriers should be extracted from their respective electrodes. The overall efficiency of a photovoltaic device is then dependent on the efficiency of these individual steps.

Semiconductor nanocrystals are promising materials for photovoltaic applications, as they can be engineered to absorb light ranging from the visible to the near infrared and single absorbed photon can generate multiple excitons [9,30-33]. However, these materials suffer from low carrier mobility, which severely limit the prospects of efficient charge extraction and carrier transport [34]. For this reason, photovoltaics based on semiconductor nanocrystals have efficiency no higher than 6 % [34].

The current photovoltaic market is dominated by crystalline silicon solar cells of thicknesses between 180 and 300 μm and efficiencies around 28 %. Silicon is the most established and widely used semiconductor for the development of photovoltaic cells and electronic devices. Most of the commercial solar cells take advantage of the well-studied p-n junction structure for the separation of carriers, which are produced by the absorption of sunlight. Thin film silicon solar cells are also extensively used in an effort to minimize the material cost [35]. Nevertheless, their relatively low absorbance of light and consequently the limited power conversion efficiency, especially for indirect band gap semiconductors such as silicon, is still an issue [36]. Therefore, structuring or combining different materials to improve the absorption efficiency of thin silicon films is crucial for the large-scale generation of electrical power from solar cell technology [34,37].

The combination of different materials for efficient photovoltaic devices was first realized by Dexter in 1979 [38]. He considered a structure which combines an organic material and a semiconductor. According to Dexter the organic material could work as an efficient solar absorber and excitons could be created in the semiconductor by means of fluorescent resonance energy transfer (RET). RET is a spectroscopic process, by which energy is passed non-radiatively between molecules [39]. The “donor” molecule, which should be a fluorophore,

absorbs a photon and transfers its energy to the "acceptor" molecule. The RET mechanism will extensively be explained in Chapter 2.

Experimental spectroscopic evidence for RET from lead sulfide (PbS) quantum dots (QDs) to epitaxial grown quantum well was demonstrated by Lu S *et al.* in 2007 [29]. The quantum well was a GaAs/[$(InAs)_1(GaAs)_2$]×8/GaAs short period superlattice buried below the sulfur-passivated GaAs surface. Two years later, Chanyawadee S. *et al.* [40] presented a hybrid photovoltaic device which takes advantage of the RET mechanism. This device was a patterned p-i-n structure consisting of multiple GaAs quantum wells with AlGaAs barriers in which channels were fabricated and filled with cadmium selenide/cadmium sulfide (CdSe/CdS) QDs. The authors combined spectroscopic evidence of RET and photocurrent measurements that showed a six-fold enhancement of the photocurrent in the patterned hybrid devices in comparison with the bare p-i-n structure.

Further evidence supporting the potential feasibility of the solar cell paradigm based on the RET mechanism from deposited PbS QDs on the top of silicon nanowires, was reported the same year by Lu S *et al.* [41]. Photocurrent time resolved measurements were performed and showed a clear increase in the photocurrent at delay times of ten to hundreds nanosecond in the case of the hybrid structure in comparison with the bare silicon nanowire structure.

Experimental demonstrations of RET into silicon substrate are under particular interest because they increase the possibility for the development of efficient thinner photovoltaic devices, which take advantage of the maturity of silicon technologies. Hybrid structures of silicon substrate and semiconductor quantum dots have the potential to improve the low absorption of silicon and lead to thinner efficient photovoltaics.

1.2 Colloidal semiconductor nanocrystals for laser applications

Colloidal nanocrystal QDs are excellent materials for constructing lasers due to the large separation between their discrete energy levels, which inhibits thermal depopulation of the lowest exciton transition, and results in narrow emission lines and high temperature stability

[42]. The stimulation emission from colloidal semiconductor nanocrystals has been widely studied using transient absorption technique and was concluded that gain can be achieved both in the multiexciton and single exciton regime [43-47].

Research in developing lasers based on colloidal semiconductor nanocrystals has experienced significant growth over the past decade. The incorporation of colloidal semiconductor nanocrystals into different types of cavities, such as spherical microcavities [48-50], microrings [42], distributed feedback resonators [51,52] and quantum wells [53], was exploited to provide optical feedback for laser applications.

Spherical and cylindrical microcavities are usually referred to as whispering gallery mode (WGM) resonators and their format is based on a dielectric spheroid structure [22,48,54-57]. This type of resonators can have extremely high Q factors, defined as

$$Q = \frac{\lambda}{\Delta\lambda}$$

where λ is the resonance wavelength and $\Delta\lambda$ the bandwidth of the cavity mode. Q factors may exceed 10^8, as a result of the strong confinement of photons within the modal volume.

Artemyev *et al.*, demonstrated in 2000 coupling between the electronic states of CdSe colloidal semiconductor nanocrystals and the photonic states of a micrometer side spherical microcavity [58]. One year later, the same group observed multimode lasing from heterostructured CdSe coated with zinc sulfide (ZnS) QDs [48]. Multimode lasing from close-packed films of CdSe QDs into micro-capillary tubes that act as cylindrical microcavities was also observed [42]; the lasing threshold was 1.25 mJ cm^{-2}. Both Schäfer J. *et al.* and Snee P. T. *et al.*, presented single and multimode lasing, few years later [49,55]. In one case, charged droplets containing CdSe/ZnS QDs were electrodynamically levitated and optically pumped resulting in single or multimode laser (depending on the size of the droplet) with a 44 mJ/cm^2 threshold [49]. In the other case, silica and polystyrene microspheres were coated with CdSe/CdZnS QDs and the lasing threshold varied from 8.1 mJ/cm^2 to 41.8 mJ/cm^2 depending on the size and the material of the microspheres [51].

1.3 Nanomaterials for neural interfaces

Nanomaterials are expected to have a high impact on biological sciences and medicine. This section is dedicated on describing advances and challenges on interfacing neuron cells.

Interfacing neural tissue is an especially challenging problem due to the following requirements: i) biocompatible electrodes are needed in order to detect electrical signals by a single neuron, ii) stimulation of neuron-cells is also required for the study of inter-neuron communication and the treatment of several diseases of the nervous system including chronic pain, hearing loss and obesity, iii) the monitoring of different substances such as gene expression and proteins is essential for the study of neuronal functions and iv) patterning of neurons is also crucial for the fundamental study of neurons behavior but also for guiding neurons on the surface of the electrode [59].

Colloidal QDs are photostable emitters and their optical properties can open very interesting perspectives as new spectroscopic tools in order to observe changes in membrane potential of neurons [59]. Nevertheless, the problem related to their toxicity requires further advances on their functionality with organic molecules.

Other techniques control neural interfacing through chemical and physical patterning. The topography of neurons can be controlled by chemical functionalization of the substrates with self-assembled monolayers [60-62]. The functionalized substrates inhibit cell adhesion to bind to hydrophobic domain, hence neuron patterning is achieved [63]. These types of chemical patterning become less effective over time and does not allow low density of cells to get patterned, hence cells do not retain the physiological properties that they exhibit in bulk culture [59].

The topographic effect was investigated for silicon and polymer demonstrating that directed growth of neurons could be achieved. Physical patterning of neurons can be easily accomplished by varying the surface roughness of the substrate or by creating column structures that promote cell adhesion [64]. Nano-gratings with 500 nm wide ridges and grooves were also used for the alignment of neuron [65].

Furthermore, field effect transistors have been fabricated for the study of signal processing in neural networks [64,66-69]. This method overcomes the limitations of membrane potential sensitive dyes and patch-clamp techniques. Potential sensitive dyes allow the voltage changes in the membrane of neurons to be recorded as emission spectral shifts from multiple sites. Potential sensitive dyes are, however, toxic and are not recommended for long-term recording [70-75]. Patch-clamp technique is another method, widely used for recording the potential of neurons. This technique requires the use of a glass pipette electrode which is in contact with the membrane of the cells while a second electrode is inside the solution. This invasive method does not allow the monitoring of the electrical activity of neurons for more than several hours due to the contact between the cell and the glass electrode [76,77].

In summary, several techniques have been developed for interfacing neural networks. However the complexity of neurons behavior requires the development of a non-invasive apparatus that offers spatial and temporal resolution for recording the electrical activity and patterning the neuron cells.

1.4 Overview of the thesis

The thesis deals with the study of the optical properties of QDs and rods and their interaction with other materials for the development of hybrid devices. It also explores the use of a photonic substrate for neural interfacing.

This thesis is structured into six chapters, the first of which is this introduction. In Chapter 2, the electronic structure of semiconductor nanocrystals is explained. The mechanism of RET which is also outlined here, allows energy to be transferred between two excitonic systems. The chapter ends with a brief description of the whispering gallery mode resonators properties.

Chapter 3 investigates the exciton dynamics of colloidal lead sulfide (PbS) QDs for a wide size and temperature range. Time resolved and integrated photoluminescence (PL) measurements for PbS QDs in solution and deposited on glass substrates are presented. The overall non-

monotonous behaviour of PbS QDs defines three different temperature regimes, which are explained by a simple model. This model interprets the carriers' dynamics and the behaviour of the surface states in oleic acid capped PbS QDs, while simultaneously allows for a quantitative estimation of the lowest splitting energy and dark- bright exciton lifetimes.

Having interpreted the exciton dynamics in oleic-capped PbS QDs, RET is studied from PbS QDs to bulk silicon. PbS QDs are placed onto silicon substrates with different thicknesses of silicon oxide grown on the top and the efficiency of RET is investigated. Finally, temperature measurements are also presented for PbS QDs deposited on silicon oxide/silicon samples in order to compare the efficiency of RET mechanism at low and room temperatures.

In Chapter 4, the development of a single mode laser based on 8 μm silica spheres coated with CdSe/CdS core/shell QRs by pumping through tapered fibers is demonstrated. Multimode lasing is also showed from larger silica spheres coated with the gain medium. Tunability of the laser wavelength, within a wavelength range that includes approximately 30% of the free spectra range of the microsphere, is achieved.

Chapter 5 is focused on the biocompatibility and the spatially selective attachment of neuron cell lines onto lithium niobate ($LiNbO_3$) substrates. The differentiation and proliferation of two different neuron-like cell lines on both polarizations of $LiNbO_3$ substrates are presented and compared with cell lines on glass substrate. Preferential growth of both cell lines on ferroelectric-engineered micropyramids is also demonstrated indicating patterning of neuron cells.

This thesis concludes with a summary of the work presented here and an outlook for future work that will allow us to apply the finding of this thesis for the development of novel photonic devices.

Chapter 2: Theoretical Background

2.1 Electronic structure of semiconductor nanocrystals

2.1.1 Concept of quasiparticles: electrons, holes and excitons

Electrons in the conduction band of a crystal are particles with charge –e, spin ½, mass m_e*, quasi-momentum $\hbar k$ and their properties result from the interactions in a many-body system consisting of a large number of positive nuclei and negatively charged electrons [78]. This large number of interacting particles can be replaced by a number of non-interacting quasi-particles. Within the framework of this consideration, an electron in the conduction band is approached as a primary elementary excitation of the electron subsystem of a crystal. The other elementary excitation is a hole, which is a quasi-particle relevant to an ensemble of electrons in the valence band from which one electron is removed. Holes are characterized by the positive charge +e, spin 1/2, effective mass m_h* and proper quasi-momentum. The effective mass of a hole m_h* is usually larger than the electron mass m_e*.

Within the framework of the elementary excitation, the ground state of a crystal is described as a vacuum state where neither an electron nor a hole exists in the conduction or valence band, respectively [79]. In the first excited state, an electron-hole pair is created. The transition from the ground to the first excited state occurs due to external perturbation such as photon absorption with respect to the energy and momentum conservation

$$\frac{\hbar c}{\lambda} = E_g + E_{e\,kin} + E_{h\,kin} + E_{Coulomb} \tag{2.1}$$

where λ is the wavelength, E_g the band-gap, $E_{e\,kin}$ the kinetic energy of the electron and $E_{h\,kin}$ the kinetic energy of the hole, $E_{Coulomb}$ is the Coulomb interaction and c is the speed of light. The band-gap energy is the minimum required energy for the creation of one electron-hole pair. The reverse process is also possible and describes a downward radiative transition equivalent to annihilation of the e-h pair and creation of a photon. The distribution of electrons and holes is described by the Fermi-Dirac statistic:

$$f(E) = \frac{1}{exp\frac{E-E_F}{K_B T}+1} \tag{2.2}$$

where K_B is the Boltzmann constant, E_F is the chemical potential commonly referred to as the Fermi level, and T is the absolute temperature and E the energy.

Electrons and holes, being charged particles, interact via Coulomb interaction and form the electron-hole pair, which is commonly called exciton. The exciton is characterized by the exciton Bohr radius which represents its natural spatial extension after its creation until its annihilation and this radius is calculated by the equation:

$$a_B = \frac{\varepsilon \hbar^2}{\mu e^2} \tag{2.3}$$

where ε is the dielectric constant of the crystal and μ is the electron-hole reduced mass given by $\mu^{-1} = m_e^{*-1} + m_h^{*-1}$. The exciton Rydberg energy ($R_y{}^*$) or exciton binding energy is given by

$$R_y{}^* = \frac{e^2}{2a_B} \tag{2.4}$$

and corresponds to the ionization energy of the lowest state [80]. The value of the Bohr radius for common semiconductors varies between 1 and 10 nm while the exciton Rydberg energy values range from 1 to 100 meV.

An exciton behaves as a single particle and its motion is described by its center of mass, $M = m_e^* + m_h^*$. The dispersion relationship can be expressed as

$$E_n(K) = E_g - \frac{R_y^*}{n^2} + \frac{\hbar^2 K^2}{2M} \tag{2.5}$$

where K is the exciton wave vector. If an exciton is created by the absorption of a photon, the total energy E_{exc} can be derived by the equation:

$$E_{exc} = E_g - \frac{R_y^*}{n^2} \tag{2.6}$$

2.1.2 The particle in a sphere model

The simplest way to approach what happens to electrons, which are in a quantized structure, is to consider the behaviour of an electron in a box. The Schrödinger equation in one spatial dimension reads:

$$\frac{\hbar^2}{2m_e}\frac{d^2\psi}{dx^2} + V(x)\psi = E\psi \tag{2.7}$$

where $V = \begin{cases} 0, & 0 < x < a \\ \infty, & x \leqslant 0, x \geqslant a \end{cases}$ is the potential, E is the electron energy, m_e is the mass of the electron, and ψ the wavefunction of the electron. The solution of this differential equation is described by the form $\psi(x) = Ae^{ikx} + Be^{-ikx}$. If it is assumed that the potential is infinitive

high at the border regions, then, the boundary conditions are: $\psi(0) = 0$ and $\psi(a) = 0$ where a is the length of the infinitive well. These conditions describe that the wavefunction vanishes at the boundaries. The solution of the Schrödinger equation for $\psi(0) = 0$ leads to B= -A, and so the wavefuction is written as $\psi(x) = Csin\,(kx)$. The second boundary condition is satisfied for $Csin(ka) = 0 \Rightarrow k = \frac{n\pi}{a}$ where $n \in$ N*. The discrete energy levels are then given by

$$E_n = \frac{\pi^2\hbar^2}{2ma^2}n^2 \tag{2.8}$$

The expression (2.8) shows that the energy is quantized and inversely proportional to the square of the size of the box.

In the case of the spherical particles, spherical coordinates can be used and the energy of the particle $E_{n,l}$ is given by:

$$E_{n,l} = \frac{\hbar^2 {k_{n,l}}^2}{2\,m_o} \tag{2.9}$$

The eigenfunctions are atomic-like orbitals, which are characterized by three quantum numbers *n*, *l*, *m*. The energies are identical with the kinetic energies of a free particle with the only difference that the wave-vector $k_{n,l}$ is quantized by the spherical conditions. So far, it is assumed that the particle is inside an empty sphere. The required assumptions need to be explained in order to approach the case where the sphere is filled with semiconductor atoms. For the bulk materials, the electronic wavefunctions can be written as:

$$\Psi_{nk}(\vec{r}) = u_{nk}(\vec{r})\,\exp\,(i\vec{k}\vec{r}) \tag{2.10}$$

where $u_{nk}(\vec{r})$ is the Bloch function describing the periodicity of the crystal lattice and is labelled by the band index *n* and wave vector $\vec{k}$. The energies of these wavefunctions can be described by a band diagram, which is a plot of energy versus the wave vector. In general, these band diagrams are complex plots and difficult to calculate. According to the effective mass approximation, bands are assumed to have parabolic forms near the extrema of the band diagram and the energy of the conduction (E_k^c) and valence bands (E_k^v) are calculated as:

$$E_k^c = \frac{\hbar^2 k^2}{2m_{eff}^c} + E_g \tag{2.11}$$

$$E_k^v = -\frac{\hbar^2 k^2}{2m_{eff}^v} \tag{2.12}$$

respectively, where m_{eff}^{c} , m_{eff}^{v} are the conduction and the valence effective mass, respectively. The effective masses approximation is based on two important assumptions: i) the semiconductor atoms in the lattice to be completely ignored and ii) the electron and hole can be treated as free particles with different masses.

The effective mass approximation is also adopted in the case of nanocrystals where it is assumed that the electron and hole wavefunctions can be described by using Bloch functions. This approximation is called envelope function approximation and is valid only when the size of the nanocrystals is much larger than the lattice constant of the material. Hence, the single particle wavefunction Ψ_{sp} is given by:

$$\Psi_{sp}(\vec{r}) = \sum_k C_{nk} u_{nk}(\vec{r}) \exp(\vec{k}\vec{r}) \tag{2.13}$$

where C_{nk} are expansion coefficients which ensure that the sum satisfies the spherical boundary condition of the nanocrystal. If we further assume that the Bloch functions are not strongly dependent on the wave vector k, then

$$\Psi_{sp}(\vec{r}) = u_{n0}(\vec{r}) \sum_k C_{nk} \exp(\vec{k}\vec{r}) = u_{n0}(\vec{r}) f_{sp}(\vec{r}) \tag{2.14}$$

where $f_{sp}(\vec{r})$is the single-particle envelope function. The function $u_{n0}(\vec{r})$ can be determined as the sum of atomic wave functions over the lattice sites, therefore the nanocrystal problem is reduced to calculate the envelope functions $f_{sp}(\vec{r})$ exactly as addressed in the beginning of this section.

Finally, the Coulomb attraction between the electron and the hole should be taken under consideration. The Coulomb interaction is inversely proportional to the radius of the nanoparticle and this term can be added as a first-order energy correction.

2.1.3 Quantum confinement in low dimensions

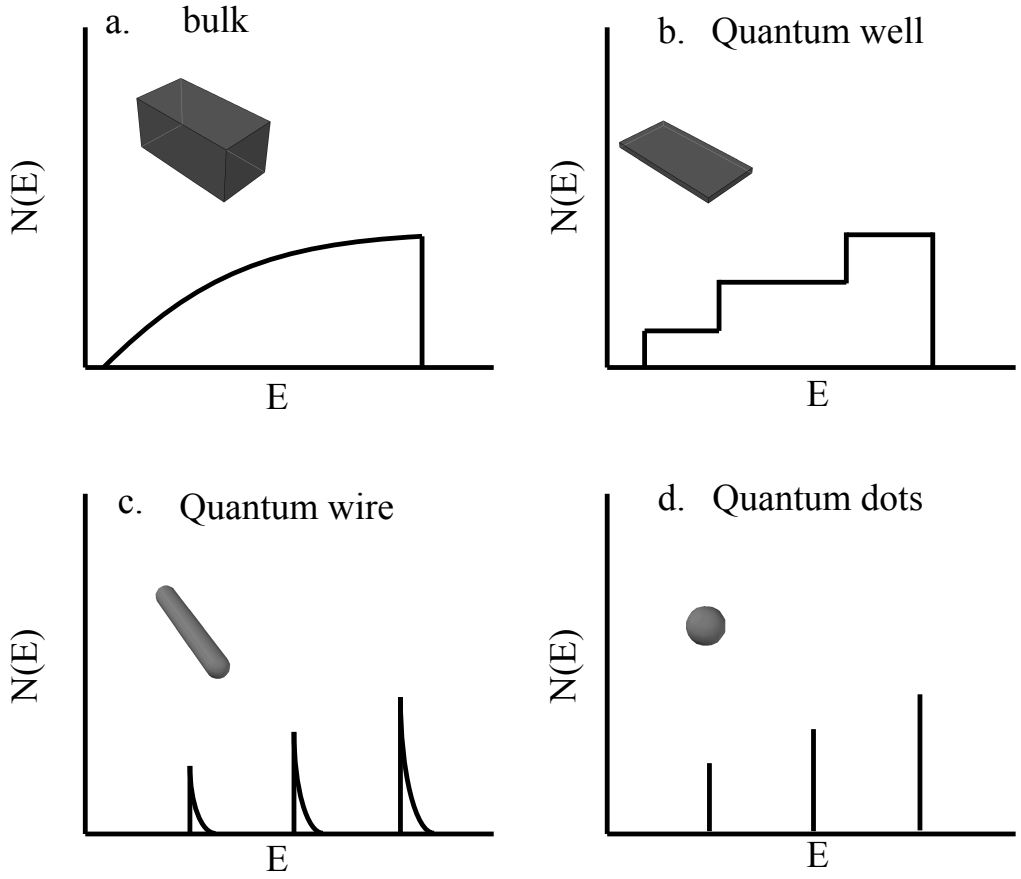

Figure 2.1: The density of states for a) bulk semiconductor, b) quantum well, c) quantum wire, and d) QDs

If the size of a semiconductor nanocrystal is in three dimensions comparable to or less than the Bohr radius, but larger than the lattice constant α_L, is called quantum dot (QD). In these zero dimension structures, excitons experience quantum confinement along the three axes. The density of electron and hole states in these structures can be expressed by

$$\rho(E) \propto E^{\frac{d}{2}-1}, \text{ d=1,2,3} \qquad (2.15)$$

where d is the dimensionality and is equal to zero for the case of the QDs, and E is the energy measured from the bottom of the conduction band for electrons and from the top of the valence band for holes [81]. Figure 2.1 illustrates the density of states in a bulk, two dimensional (quantum well), one dimensional (quantum wire) and zero dimensional (quantum dot) structures [4]. In the case of zero dimension structures a number of discrete energy subbands emerge.

The quantum confinement of the electron and the hole in a zero dimensional structure such as semiconductor nanocrystal can be categorized by comparing the size of the quantum dot to the exciton Bohr radius. Three different regimes can then arise, the weak ($\alpha \gg \alpha_B$), the intermediate ($\alpha \approx \alpha_B$) and the strong confinement regime ($\alpha < \alpha_B$).

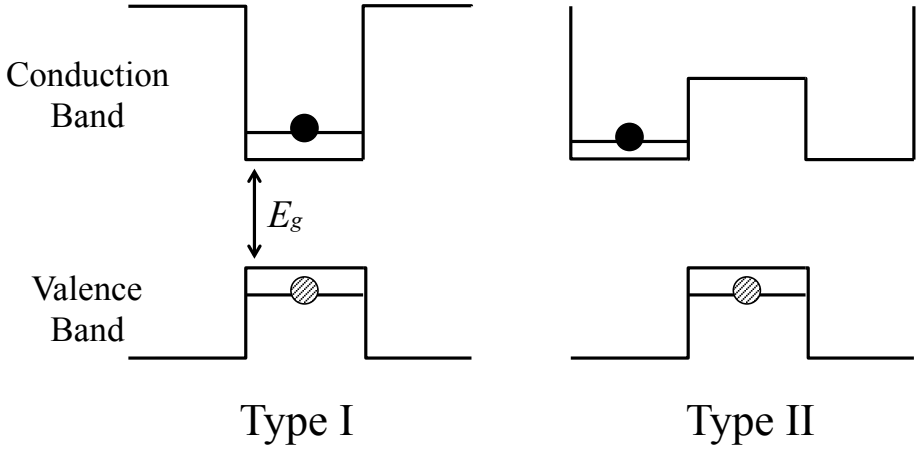

Figure 2.2: The carriers are confined in the same volume in Type I nanocrystals, while in Type II, the carriers are spatially separated

In the weak confinement regime the Coulomb interaction between holes and electrons is strong and the kinetic energy associated with the centre of mass motion of exciton increases. In the intermediate regime the system can behave in different ways, depending on the ratio of the radii of the nanocrystals with the Bohr radii of electrons (α_e) and holes (α_h) respectively. The two different types of confinement for QDs in the intermediate regime are shown in Figure 2.2. In Type I confinement, the conduction and valence band minima are in the same material and hence, electrons and holes are confined in the same volume. In Type II, the conduction and valence band minima are located in different materials and therefore, spatial separation of electron and hole occurs. In the strong confinement regime the uncorrelated motion of an electron and a hole may be considered as a first approximation [81].

The Hamiltonian that governs the envelope function for electrons and holes for the general case is:

$$H = \frac{-\hbar^2}{2m_e^*}\nabla_e^2 - \frac{-\hbar^2}{2m_h^*}\nabla_h^2 + V(r_e) + V(r_h) - \frac{e^2}{\epsilon|r_e - r_h|} \quad (2.16)$$

where $V(r_i)$ is the potential experienced by the localized electron or hole, and r_e and r_h are the position coordinates of the electron and hole respectively in the solid and e is the charge of electron and hole. The energy of the exciton ground state can be described by

$$E_{1S} = E_g + E_{quantisation} + E_{Coulomb} = E_g + \frac{\hbar^2\chi_{10}^2}{2\mu a^2} - 1.786\frac{e^2}{4\pi\epsilon a} \quad (2.17)$$

The Coulomb interaction is dominant in the weak confinement regime. Although, in the strong confinement regime the last term that describes the Coulomb interaction can be ignored.

Furthermore, quantum confinement has an important effect on the oscillator strength, *f,* of the optical absorption due to the increased overlap between the electron and hole wavefunctions. The oscillator strength of exciton absorption per unit volume is proportional to the transition dipole moment and the probability of finding an electron and a hole at the same site. The oscillator strength is given by the expression

$$f = \frac{2m_e^*}{\hbar^2}\Delta E|M_t|^2\left|U_{(o)}\right|^2 \quad (2.18)$$

where ΔE is the transition energy, M_t the transition dipole moment and $\left|U_{(o)}\right|^2$ is the probability of finding an electron and a hole in the same site- this corresponds to the overlap of electron and hole wavefunction [79]. As the volume of the nanocrystals decreases, the overlap of electron and hole wavefunctions increases and hence $\left|U_{(o)}\right|^2$ and the oscillator strength also increases.

2.1.4 Absorption and emission of photons in zero dimension structures

The absorption of a photon by the nanocrystal occurs if its energy is higher than the bandgap and results in the formation of an exciton. As shown in the Equation (2.8), the energy levels in the nanocrystals form at higher energies when the size of the nanocrystal is decreased, and hence the absorption onset exhibits a blue shift. An absorption feature near the absorption onset corresponds to the excitonic peak with the lowest energy transition and the highest oscillator strength (Figure 2.3).

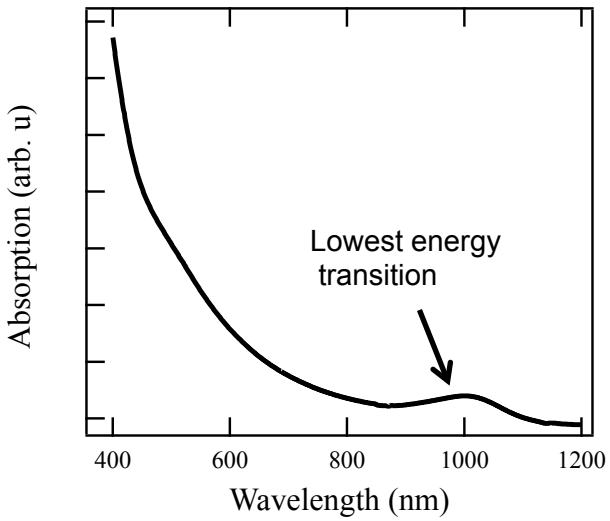

Figure 2.3: Absorption spectrum of PbS QDs. The absorption peak at 1000nm corresponds to the lowest energy transition

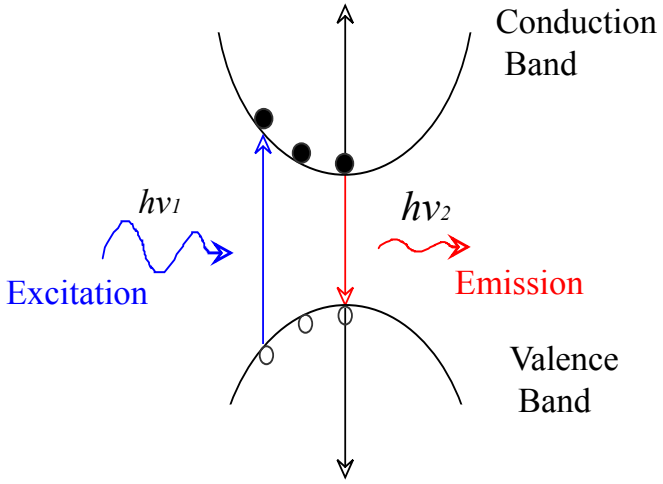

Figure 2.4: Schematic representation of the different exciton states in QDs and the involved absorption and emission processes

The probability of making an optical transition from the ground state $|\psi_0\rangle$ to a particular excited state is calculated by the dipole matrix element [79]

$$P = \left|\langle\psi_{ehp}|\vec{e}\hat{p}|\psi_o\rangle\right|^2 \tag{2.19}$$

where $\vec{e}$ is the polarization vector of the light and $\hat{p}$ is the momentum operator. In the case of the strong confinement regime, only transitions between electron and hole states of the same main and angular moment quantum number are allowed ($\Delta n=0$ and $\Delta L=0$).

The annihilation of an exciton results in the emission of a photon. The absorption and emission processes are schematically shown in Figure 2.4. A photon with an energy hv_e larger than the bandgap is absorbed and consequently creates one or more excitons (electron-holes pairs). The carriers, then, relax to the lowest excited state after their interaction with phonons and finally, recombine by emitting a photon. The energy of the emitted photon is lower than the initial energy of the absorbed photon and corresponds to the band gap of the nanocrystal. It has been observed that the maximum of the emission peak is red-shifted compared to the excitonic peak in the absorption spectrum. This phenomenon is due to the fine-structure of the exciton energy levels inside the nanocrystals and is called Stokes shift [80].

2.1.5 Exciton fine structure in zero dimensions

In order to describe the nature of the emitting exciton state, three limits are considered: i) the effect of anisotropy of the crystal lattice, ii) the non-perfect-spherical shape of the semiconductor nanocrystal and iii) the electron-hole exchange interaction.

2.1.5.1 Crystal field splitting

In our discussion so far, it was assumed that simple parabolic bands approximate the valence and conduction bands. Nonetheless, the real band structure is more complicated and the valence band cannot be described by the effective mass approximation due to the spin-orbit coupling [1,79]. In an ideal diamond-like structure, the strong spin orbit interaction splits the valence band into the fourfold degenerate heavy hole and light hole bands, which are generally referred to as A and B subband and the split-off band, which is usually called C subband (Figure 2.5). In the case of CdSe QDs, the crystal field arising from the hexagonal lattice lift the degeneracy of the A and B subbands at k=0. This crystal splitting is 25 meV in the bulk CdSe and is usually neglected [79].

These A and B subbands do not produce their own independent ladder of hole states but exhibit hole state mixing.

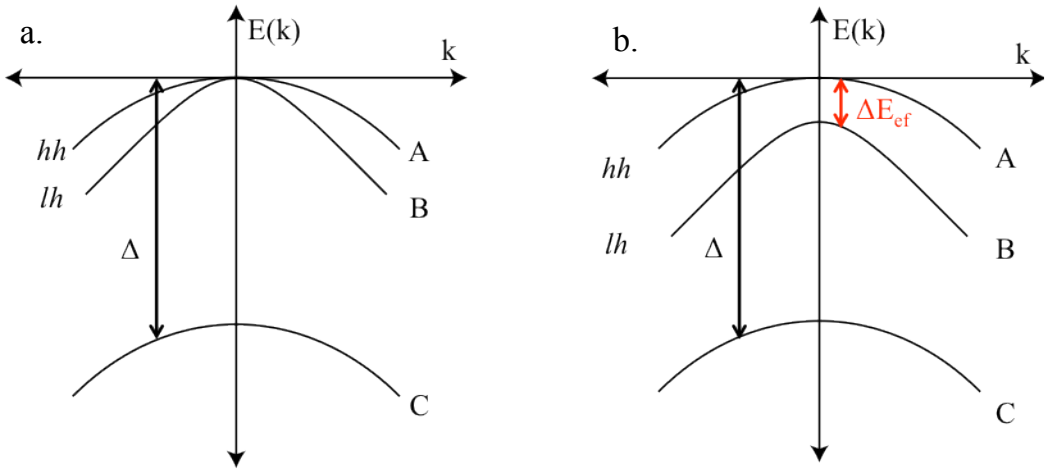

Figure 2.5: a) Valence band at k=0 for diamond-like semiconductor, b) The valence band structure for CdSe crystal near k=0

2.1.5.2 Shape asymmetry mixing

Another assumption that was made at the beginning of this chapter is the perfect spherical shape of the QDs. This assumption leads to highly degenerate electron and hole states. For example, the first excited state of CdSe QDs is eightfold degenerate [82]. However, any variation in the shape of the QDs reduces the degeneracy and splits the electron-hole pair states. This can be better understood, if we assume a particle whose shape is given by the equation:

$$\frac{x^2+y^2}{b^2}+\frac{z^2}{c^2}=1 \tag{2.21}$$

By replacing $x \to \frac{bx}{a}$, $y \to \frac{bx}{a}$ and $z \to \frac{cx}{a}$ in the equation (2.21), the equation for the surface of a sphere with radius a, appears. Applying the same change of variables, then, the Hamiltonian operator ($\widehat{H}$) will consist of two components:

$$\widehat{H}=\widehat{H}_L+\hat{V} \tag{2.22}$$

where $\widehat{H}_L$ is Luttinger Hamiltonian describing the unperturbed spherical NC and the component $\hat{V}$ corresponds to anisotropic perturbation resulting from the shape asymmetry.

2.1.5.3 Exchange interaction

The electron–hole exchange interaction takes effect on degenerate excitonic states with identical total angular momentum. It is proportional to the overlap of electron-hole wavefunctions, therefore this interaction is strongly enhanced due to the confinement of the carriers [5,6,12,82,83].

For nanocrystals in the strong confinement regime, such as PbSe and PbS, the electron-hole exchange interaction splits the lowest level of the conduction band into a lower energy non-degenerate singlet (dark) and three times degenerate higher-energy triplet (bright) states, separated by the exchange spitting ΔE [12]. The spitting was calculated to increase for smaller particles since the confinement of carrier enhances the overlap of electron and hole wavefunctions [82].

2.1.6 Optical gain in semiconductor nanocrystals

Optical gain, as described by Klimov [1,43,44], corresponds to a light-matter interaction regime for which the generation of photons by stimulated emission dominates over photon absorption. Stimulated emission is defined as the process in which the atom gives up its excess energy, *hv,* to the field, adding coherently to the intensity. The added photon has the same frequency, the same phase, the same polarization and propagates in the same direction, as the wave that induced the atom to undergo this type of transition [84].

A lasing media can exhibit optical gain when a population inversion occurs. In this situation, the number of electrons in the excited state should be greater than that in the ground state. For explaining the optical gain in semiconductor nanocrystals, we simplify the structure of their energy levels. We consider their energy levels as a two-level system with two electrons in its ground state. Excitation of a single electron (single exciton) in the excited state does not produce gain but results in optical transparency (Figure 2.6a). The stimulated emission of the electron being in the excited state is compensated by absorption, due to the remaining electron in the valence band. Thus, gain could be achieved only if both electrons are excited, creating two excitons (biexcitons) [1,43-46].

Therefore, it has been shown that optical gain can also be achieved by a single exciton, if the local electric field associated with this electron-hole pair induces a splitting to the lowest energy level of the conduction band (Stark effect) greater than the transition line width [44]. In this description, the transient Stark shift is determined by the exciton-exciton Coulomb interaction energy and is defined as $\Delta_{XX} = E_{XX} - 2E_X$, where E_{XX}, E_X are the single and biexciton energies respectively. The energy Δ_{XX} depends on the local electrical charge densities $\rho_X(r)$ associated with a single-exciton state, which is given by $\rho_X(r) = e\,(|\Psi_h(r)|^2 - |\Psi_e(r)|^2)$, where e is the electron charge, $\Psi_h(r)$ is the spatial distributions of hole and $\Psi_e(r)$ is electrons wavefunctions.

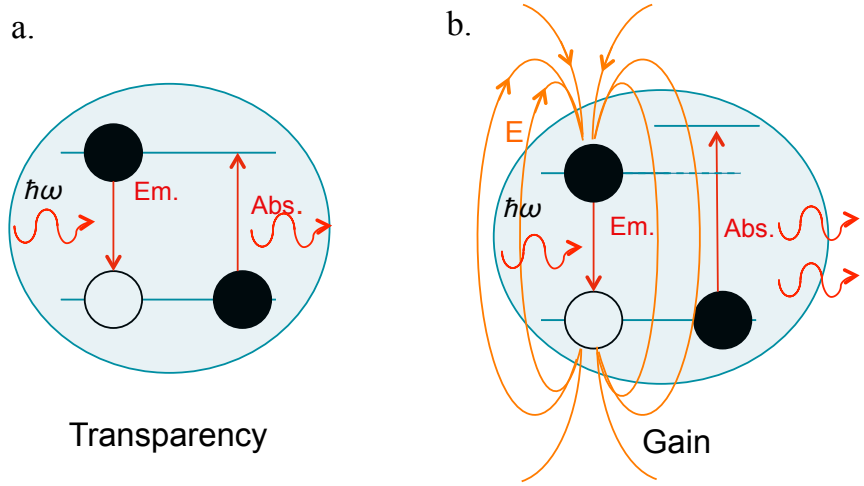

Figure 2.6: a) The stimulated emission is exactly compensated by the absorption leading to optical transparency, b) the exciton-exciton interaction in Type II nanocrystals spectrally displace the absorbing transition with respect to the emission band, and hence if Δ_{XX}>>linewidth optical gain can occur in the single exciton regime [44]

Nanocrystals in the strong confinement regime and Type I intermediate regime exhibit almost identical spatial distribution between electron and hole wavefunctions, thus the values of Δ_{XX} energy are commonly smaller than typical transition linewidths. On the other hand, nanocrystals in the Type II intermediate regime are composed of two materials where their conduction or valence bands are not aligned; hence spatial separation between electron and hole can be achieved. In the case of CdSe/CdS QRs, holes reside in CdSe core while electrons are

delocalized over the entire hetero-crystal which leads to a significant difference in the spatial distributions of negative and positive charges [85,86].

It is also worth taking into consideration the sign of the exciton-exciton interaction energy. The Coulomb interactions in Type I nanocrystals spatially arrange the charges, such that the biexciton energy E_{XX} is less than twice the exciton energy E_X. In this case, the energy Δ_{XX} is negative indicating the attraction between exciton-exciton. In comparison the Coulomb interaction in Type II nanocrystals do not control the spatial arrangement of the charges due to the large gradient potential at the core/shell interface and hence identical sign charges are concentrated in the same part of the hetero-crystal. This type of arrangement increases the repulsive component of the Coulomb interaction and decreases its attractive component, which results in exciton-exciton repulsion [44].

The sign of the energy Δ_{XX} affects the optical gain, because it determines the direction of the absorbing transitions with respect to the emission line. In the case of Type I nanocrystals, the transitions move downward in energy, increasing the absorption above the emitted band. In the other case, the repulsive attraction between exciton-exciton moves the absorbing transitions away from the emission line and, consequently, benefits lasing.

2.2 Resonance Energy Transfer

Resonance energy transfer (RET) is an electrodynamic phenomenon that occurs between a donor in the excited state and an acceptor in the ground state [87]. It involves the non-radiatively transfer of the excitation energy, a donor molecule to an acceptor molecule. The process of RET mechanism can be described in the following steps:

1. The donor absorbs a photon of energy $\hbar\omega_o = E_{D,no}$ and an exciton is generated in the n_o^{th}excited state.
2. The exciton then relaxes to a lower excited state under the emission of phonons with energy $E_{D,n_1} \leq E_{D,n_o}$.

3. The energy E_{D,n_1} is then transferred from the donor to the acceptor via a dipole interaction and an exciton of the energy $E_{A,n_o} = E_{D,n_1}$ is created in the acceptor. In this point, it is worth highlighting that RET occurs without the appearance of a photon from the recombined electron-hole pair in the donor molecule. It is the result of short-range dipole-dipole interaction between the dipole moments of the electronic transitions in the donor and acceptor [37].
4. The excited (through RET process) electron–hole pair in the acceptor molecule could finally recombine by emitting a photon (Figure 2.7).

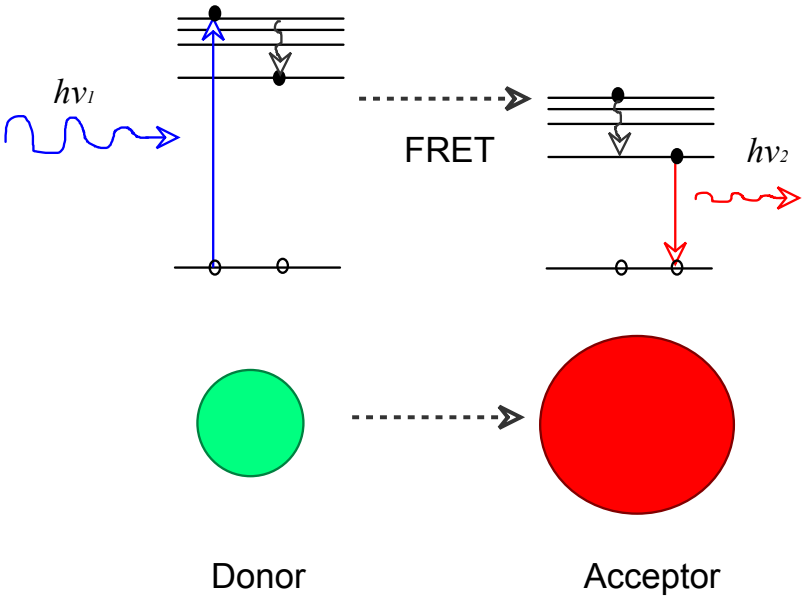

Figure 2.7: Schematic presentation of the RET process between two QDs

The rate of energy transfer ($k_T(r)$) for two point-like molecules is given by:

$$k_T(r) = \frac{\kappa^2 Q_D\, k_D}{r^6}\left(\frac{9000(ln10)}{128\pi^2 N n^4}\right)\int_0^\infty F_D(\lambda)\varepsilon_A(\lambda)\lambda^4 d\lambda \qquad (2.23)$$

where Q_D is the quantum yield of the donor in the absence of acceptor, n is the refractive index of the surrounding medium, N is the Avogadro number in mole^{-1}, r the distance between donor and acceptor in nm and k_D is the decay rate of the donor in the absence of acceptor in s^{-1}. $F_D(\lambda)$ is the corrected fluorescent intensity of the donor with total intensity normalized to unity, $\varepsilon_A(\lambda)$ is the extinction coefficient of the acceptor at λ, which is usually in units of M^{-1} cm^{-1}. The factor κ^2 describes the relative orientation in space of the transition dipoles of donor and acceptor.

According to equation (2.23), the RET mechanism is proportional to the spectral overlap between the absorption spectrum of the donor and the emission spectrum of the acceptor, the quantum yield and the decay rate of the donor. The spectral overlap between the absorption spectrum of the donor and the emission spectrum of the acceptor is expressed in equation (2.23) through the integration $\int_0^\infty F_D(\lambda)\varepsilon_A(\lambda)\lambda^4 d\lambda$. In addition, RET scales with the orientation angle between the dipoles of donor and acceptor and it is inversely analogous with the sixth power of the separation distance between donor and acceptor.

The orientation factor (orientation angle between the dipole of the donor and acceptor) is determined by the equation $\kappa^2 = (cos\theta_J - 3cos\theta_D cos\theta_A)^2$, where θ_J is the angle between the emission transition dipole of the donor and the transition absorption dipole of the acceptor, θ_D and θ_A are the angles between these dipoles and the vector connecting the donor and the acceptor (Figure 2.8). Different orientations of donor and acceptor, scale the factor κ^2 from 0 to 4 (Figure 2.8b). For head-to-tail parallel transition dipoles, κ^2 equals to 4 while for perpendicular dipoles the value of the κ^2 equals to 0.

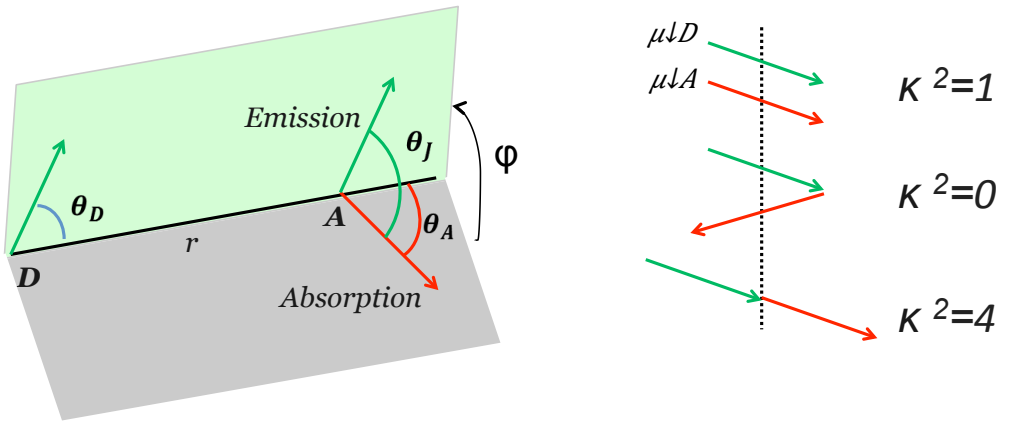

Figure 2.8: Dependence of the orientation factor κ^2 on the direction of the emission dipole of the donor and the absorption dipole of the acceptor

As already mentioned, the RET rate scale depends on the distance separation between donor and acceptor. In the case where the donor and acceptor are point dipoles, the RET rate is inversely proportional with the sixth power of separation distance between donor and acceptor molecule.

In general, the RET mechanism requires short distances between a donor and an acceptor. Usually these distances are in the scale of few nanometers.

Nevertheless, this distance dependence significantly varies for RET between a point-dipole QD and a bulk semiconductor. In this case the efficiency of RET can be illustrated in the geometry of an oscillating dipole embedded in medium 1 with dielectric function $\varepsilon_1(\omega) = \varepsilon_1'(\omega) + i\varepsilon_1''(\omega)$ at distance d from the planar interface of the medium 2 with dielectric function $\varepsilon_2 = \varepsilon_2'(\omega) + i\varepsilon_2''(\omega)$ [37]. The RET rate (k_T) into the second medium is given by

$$k_T = k_r^0 (\frac{\lambda}{2\pi d})^3 \frac{\varepsilon_2''}{|\varepsilon_1+\varepsilon_2|^2} \tag{2.24}$$

where $\lambda = \frac{2\pi c}{\omega}$ is the vacuum photon wavelength and k_r^0 is the dipole vacuum radiative rate. The decay rate in this case is inversely proportional with the third power of the separation distance between donor and acceptor. The equation (2.24) results to a power-law distance dependence of the type:

$$\frac{k_T}{k_r^0} = (\frac{R_o}{d})^i, \tag{2.25}$$

which is commonly cited for the RET rate from a point-like dipole to an array of dipole acceptors. The Föster radius R_o is the distance where the RET rate is equal with the rate of the donor.

For small separation distances between donor and acceptor, the effectiveness of RET is dictated by the second factor of the equation (2.24), which is in the range of 10^6. This enhancement can be reduced by the dielectric screening (typically $|\varepsilon_1 + \varepsilon_2|^2 \sim 10^3$). The absorptive strength (ε_2'') in the semiconductor depends on the frequency and varies between direct and indirect transitions [37].

The efficiency of RET (η) is the fraction of photons absorbed by the donor which are transferred to the acceptor and is given by:

$$\eta = \frac{k_T(r)}{k_D+k_T(r)} \tag{2.26}$$

and is the ratio of the transfer rate to the total decay rate of the donor in the presence of acceptor.

2.3 Whispery gallery modes microresonators

Whispery gallery mode (WGM) resonators consist of a dielectric material, such as silicon dioxide, with spheroidal shape [54,88,89]. The high refractive index difference between the dielectric material and the surrounding material (e.g. air), creates an interface where light rays intersect repeatedly with the critical angle, undergoing total internal reflection [22]. In the case that this ray propagates near the surface of the spheres (with radius R) and one round trip is equal to an integer number of wavelength, the constructive interference occurs with resonance condition $x = \frac{2\pi R}{\lambda}$. Therefore, WGM resonators enable optical amplifications and select specific frequencies of light that can be coupled into the optical guides [22]. This type of resonators exhibits high wavelength selectivity and small mode volume that is critical for the development of photonic circuits.

WGMs are characterized by three mode number n, l, m that corresponds to radial, polar and azimuthal components of the electromagnetic field distribution (Fig. 2.9) [90]. More specifically the n mode takes values 1, 2, 3... and describes the field intensity distribution in the radial direction. The mode number l takes values $l=n$-1 and describes the field intensity distribution in the polar direction. Finally, the mode number m can take values from $-l$ to l and indicates the number of maxima in the sinusoidal variation of the field intensity in the equatorial or azimuthal variation.

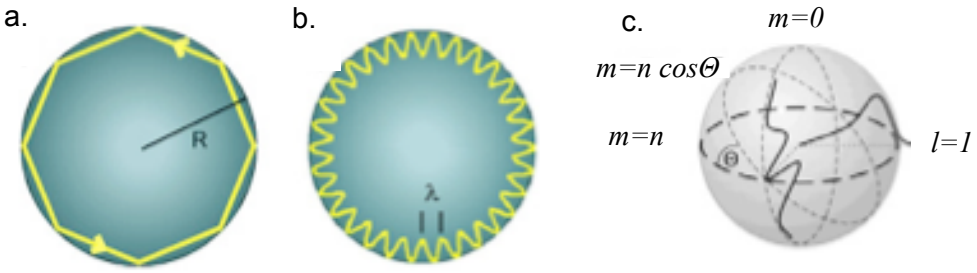

Figure 2.9: Light confinement inside a whispery gallery mode resonator, in (a) geometrical, (b) wave optics approach. (c) Schematic of a spherical microcavity showing distribution and spatial orientation of the modes [22]

Basic properties of a WGM resonator include its geometrical characteristics of the field localization usually called mode volume [91]. The mode volume for a spherical WGM resonator is given by

$$V = 3.2\pi^{\frac{3}{2}}\left(\frac{\lambda}{2\pi n}\right)^3 n^{11/6}\sqrt{n-m+1} \tag{2.27}$$

where λ is the wavelength of the pumping light.

Some important parameters that characterize a microresonator are the quality factor of the cavity (Q-factor), the free spectra range and the finesse (F). The Q-factor in an optical resonator indicates the capacity of the resonator to circulate and store light. It is defined as the ratio of stored energy to the energy dissipated to the cycle. The Q-factor is also a measure of energy losses and is defined as the time average energy in the cavity divided by the energy loss per cycle [84] and is given by:

$$Q = \omega_o \frac{Stored\ energy}{Power\ loss} = \omega_o \tau_P \tag{2.28}$$

where τ_P is a time constant describing the build up or the decay time of stored energy in the cavity [22].

The space between successive polar modes is defined by the free spectral range (FSR) and is given by the equation:

$$FSR(\Delta\nu_{FSR}) = \frac{c}{2\pi R n_1}\,(\text{Hz}) \tag{2.29}$$

where c is the speed of light, R the resonator radius and n_1 is the effective refractive index of the medium inside the resonator [92,93]. In the case of a microresonator coated with a medium with refractive index n_2, the spacing between the different modes is given by

$$\Delta\lambda_{FSR}^{azim} = \left(\frac{\lambda^2}{2*\pi*R_H*n_2}\right)\frac{tan^{-1}[\left(\frac{n_1}{n_2}\right)-1]^{1/2}}{[\left(\frac{n_1}{n_2}\right)^2-1]^{1/2}} \tag{2.30}$$

where R_H is the total radius of the microsphere with the coating [22].

The finesse factor provides a measure of the filtering properties of the cavity and relates the free spectral range to the resonance linewidth by:

$$F = 2\pi\frac{FSR}{\delta\omega} = 2\pi Q\frac{FSR}{\omega_o} \tag{2.31}$$

The finesse of an optical resonator can also be defined as the ratio between the free spectral range and its bandwidth and is independent of the resonator length.

Chapter 3: Optical properties of oleic-acid capped lead sulphide quantum dots and their potential application in silicon photovoltaics

As it was mentioned in Chapter 1, quantum dots (QDs) represent a promising material for photonic applications such as photo-detectors [18-21,94], photovoltaics [14,15,29,40,41], as well as for labelling of biological targets [95-98]. Compared with CdSe or CdS QDs, lead chalcogenide QDs (PbS, PbSe, and PbTe QDs) are better suited for the study of the strong confinement regime [83,99]. This type of materials exhibits a range of favourable properties which could be advantage for their use in photovoltaic applications. Due to their small band gap PbS QDs have been widely studied for multiple exciton generation, a mechanism that a photon with higher energy than the bandgap of the material could create more that one exciton. This mechanism could potentially lead to improved solar conversion efficiencies [100,101] as the number of the formed electron-hole pairs could be higher than the number of the absorbed photons. Using PbS QDs as a solar absorber could also yield improved photovoltaic performances, due to the good match of their absorption spectrum with the solar spectrum. Their absorption spectrum extends into near infrared and therefore solar photons at lower energy can also create excitons. The photogenerated excitons in the PbS QDs can then be transferred to silicon by means of Resonance Energy Transfer (RET). This type of hybrid solar cell devices take advantage of the high absorption efficiency of the QDs and the efficient electron and hole transport in the well studied p-n junction [41]. However, it is worth mentioning that PbS QDs is a toxic material and environmental issues are raised. For overcoming this limitation, encapsulation of the solar cell devices is required. For the encapsulation of solar cell, glass is mainly used to cover the solar panel in order to protect it from the outer environment but also to prevent the leakage of toxic materials into the environment.

Colloidal PbS QDs are usually functionalized with organic molecules or coved with a higher bandgap semiconductor material. This organic or inorganic shell around the QDs prevent their surface from photobleaching and avoid the aggregation of the QDs [102]. The surface-dependent optical properties of the QDs has been previously studied and explained due to the dangling bonds, adatoms and vacancies that can form shallow or deep traps states of electrons and holes [103]. These trap states can deactive the quantum-confined exciton by enabling non-radiative pathways [103]. Non-functionalized QDs can be also oxidized and photo-oxidized. The oxidation and photo-oxidation of the surface of the QDs result in non-radiative recombination of

electrons and holes. Passivated quantum dots show dramatically enhanced photostability which is important for long term observations.

Lead surfide QDs have been passivated with thiols and their optical properties have been extensively studied [104]. The temperature dependence of the PL emission from thiol-capped PbS colloidal QDs showed an enhancement in the QDs PL intensity for increasing temperatures up to 50K and a further decrease for temperature aboves to 50 K [104]. This PL behaviour was explained by a thermally activated redistribution of carriers in the dots in the present of a defect. However no estimation of the fine structure splitting was derived from these observations. The fine exciton splitting in colloidal PbS QDs depends on the diameter of the dots while the role of surface states is still unclear.

In this chapter, the exciton dynamic of oleic acid capped PbS QDs for a wide size and temperature range is first investigated. The optical properties of these QDs in solution and after deposition on a glass substrate are studied. Temperature dependent measurements are also performed. Three different temperature regimes are observed. The low temperature regime (<180 K) is characterized by an increase in the average decay rate and a decrease in the integrated photoluminescence (PL). The intermediate regime (~180-250 K) is described by an enhancement in the PL and a decrease in the average decay rate. The high-temperature regime (>250 K) is governed by a quench in the PL intensity and acceleration in the average lifetimes. To explain this overall trend a simple model is proposed, which interprets the carriers dynamics and the behavior of the surface states in oleic acid capped PbS QDs, and allows the quantitative estimation of the lowest splitting energy and the dark-bright exciton lifetimes. A global fit to the measured temperature and size dependent PL decay dynamics converges to a lowest exciton splitting of 3 meV that is within the range of theoretical expected values reported in the literature [83]. The model also reveals a clear trend of oscillator strength transfer from bright to dark excitons states with decreasing QDs diameter.

Having explained the exciton dynamics in oleic-capped PbS QDs, the transfer of excitons from PbS QDs to a silicon p-n junction is investigated. To demonstrate the concept, PbS QDs are placed onto a silicon substrate and the efficiency of RET from PbS QDs to bulk silicon is

investigated. The efficiency of the RET mechanism between PbS QDs and silicon is modulated by varying their separation distance. These results undoubtedly identify RET from colloidal QDs to bulk silicon. Temperature measurements are also presented and show that the RET efficiency remains high across a range of temperatures. The demonstrated findings are encouraging for further investigations and open the way for the development of hybrid photovoltaics.

3.1 Characterization techniques

Streak cameras are devices which measure ultra-fast light phenomena and provide spatial and temporal information. Streak cameras have proven to be an excellent tool for simultaneous time and spectrally resolved measurement. The operating principle of the streak camera is illustrated in Figure 3.1.

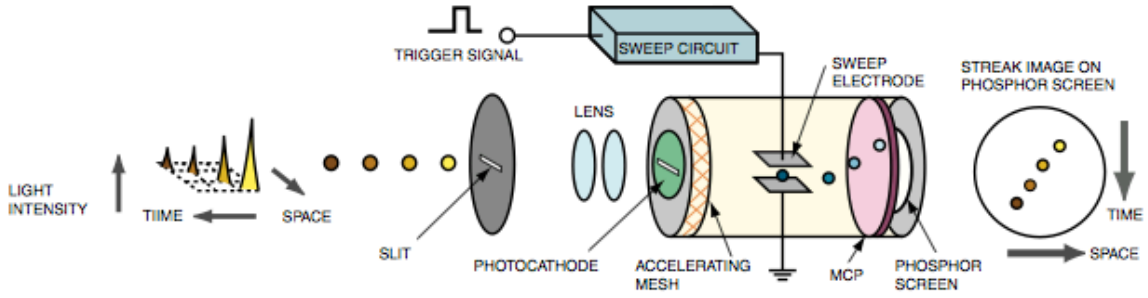

Figure 3.1: Operation diagram of the streak camera [105]

The light collected from the sample passes through a slit and a monochromator, where it is dispersed and separated into different wavelengths. The spectrally dispersed light is then directed by a set of lenses into a slit image on the photocathode of the streak tube.

The incident light incoming on the photocathode is converted into a population of photogenerated electrons proportional to the light intensity. The electrons are then accelerated via a pair of electrodes and deflected by a pair of high voltage vertical sweep electrodes. The sweep is synchronised with the pulsed excitation and the first photon triggers the start of the sweep. This initiates a high-speed sweep and therefore, the accelerated electrons are deflected on the micro-channel plate at different angles depending on their arrival time at the sweep electrodes. The micro-channel plate is an electron multiplier and contains a bundle of glass

channels with around 20 µm diameter. The inner wall of the glass channels is coated with a secondary electron emitter material. This type of micro-channel plate can multiply single electron to several thousands of electrons.

3.2 Material and Methods

3.2.1 Time resolved spectroscopy

Time resolved measurements were performed using a streak camera system with a temporal resolution of 30ns. All QDs were excited non-resonantly at 400 nm with 150 fs pulses at a 27 kHz repetition rate. Glass substrates with PbS QDs were mounted on a cold finger helium flow cryostat and excited at oblique angle as illustrated in Figure 3.2. The fluorescence was collected at normal incidence to the sample surface. Steady-state PL measurements were carried out using a charge coupled device spectrometer with an 1 nm resolution.

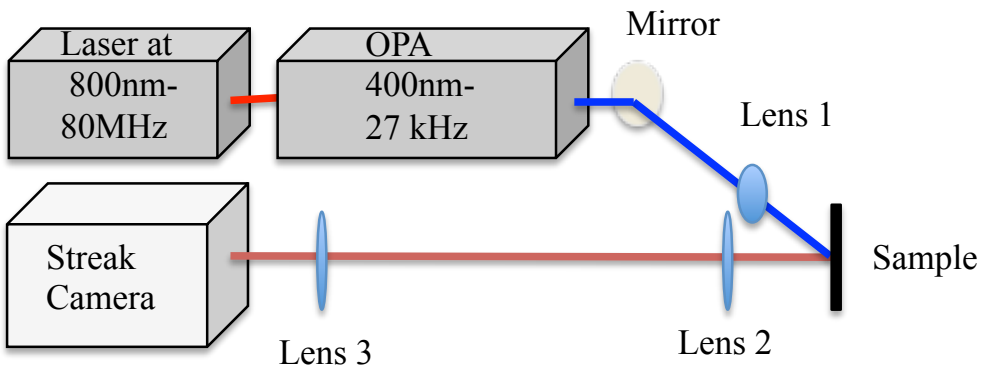

Figure 3.2: Time resolved experimental setup. The focal distance of lens 1 and 2 was 5 cm, while the focal distance of lens 3 was 15 cm.

The PL decay kinetics of PbS QDs were found to exhibit a non-single exponential behaviour that was satisfactorily described by the bi-exponential function

$$I_{PL}(t) = A_1 * e^{-k_1 * t} + A_2 * e^{-k_2 * t} + C \tag{3.1}$$

The average decay rate is given by:

$$< k_{aver} >= \frac{A_1 * \tau_1 + A_2 * \tau_2}{A_1 * {\tau_1}^2 + A_2 * {\tau_2}^2} \quad (3.2)$$

where $\tau_1 = \frac{1}{k_1}$ and $\tau_2 = \frac{1}{k_2}$ are used to monitor the overall trend of the decay dynamic at different temperatures.

3.2.2 Fabrication of silicon oxide spacer/ silicon samples

The devices studied in this work consisted of PbS QDs deposited on silicon substrates with different thicknesses of silica (SiO_2). To produce the silica spacers on the silicon sample, a silica film with thickness 100 nm was thermally grown on a silicon wafer in a furnace. This wafer was then diced into 20x20 mm^2 samples. Each sample was finally etched down by using reactive ion etching technique to obtain the required spacer thicknesses. The thickness was measured using ellipsometry techniques.

3.3 Size and temperature dependent carrier dynamics in oleic acid capped PbS quantum dots

3.3.1 Optical properties of oleic acid capped PbS quantum dots in solution

The absorption and emission spectra from oleic acid capped PbS QDs of four different diameters in toluene solution are shown in Figure 3.3a and b. The maximum of the first exciton absorption is located at 620, 730, 830 and 920 nm for PbS QDs with diameters of 2.3, 2.6, 3.2 and 3.5 nm, respectively. The PL intensity maxima of these nanocrystals are red shifted from their absorption maxima at 771, 856, 913 and 977 nm.

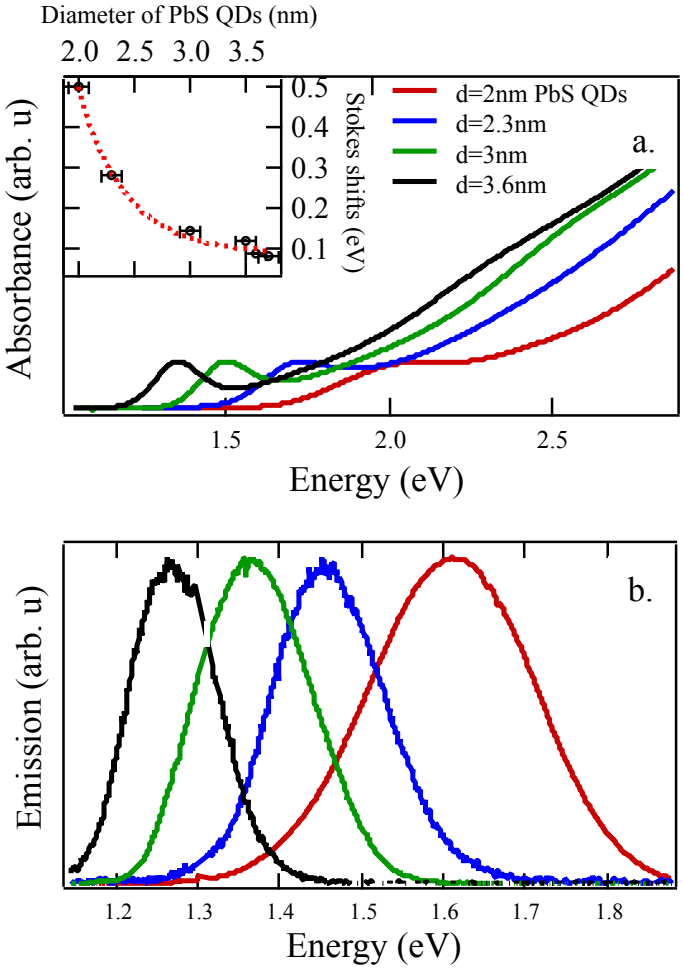

Figure 3.3: Absorption (a) and emission (b) spectra of 2.3 nm (red), 2.6 nm (blue), 3.2 nm (green) and 3.5 nm (black) of oleic acid capped PbS QDs. Inset: Stokes shift energy as function of the diameter of oleic acid capped PbS QDs

This phenomenon is usually referred to as Stokes-shift energy and has its origin in the particular structure of the exciton energy levels inside the nanocrystal (section 2.1.4). In lead salt QDs the lowest excitonic manifold initiates from four equivalent L-points in the Brillouin zone. The electron hole exchange interaction and spin orbit coupling lead to the fine structure of the lowest 1S-1S exciton state, which is represented by a nondegenarate lower-energy dark exciton state (singlet) followed by the higher energy threefold degenerate bright exciton state (triplet), which are separated by an energy gap ΔE [83]. The bright state has significantly higher oscillation strength than the dark states. PL depends on the product of the oscillator strength and the population of a given state. Carrier relaxation from the bright to the dark state with the emission

of phonons can strongly populate the dark state and enable radiative recombination of dark excitons. The Stokes-shifts of the exciton luminescence in these QDs is thus controlled by the exciton phonon interaction and the bright-dark splitting in the following way:

$$\Delta_{Stokes} = 2S\hbar\omega + \Delta E \tag{3.4}$$

where S is the Huang-Phys factor, $\hbar\omega$ the characteristic phonon energy and ΔE the dark-bright splitting. The dark-bright splitting increases for smaller QDs due to the enhanced electron-hole overlap generated by the quantum confinement, and is thus expected to be size dependent. Indeed, it is observed that Stokes-shifts exhibit a strong size dependence, which is illustrated in the inset of Figure 3.3a.

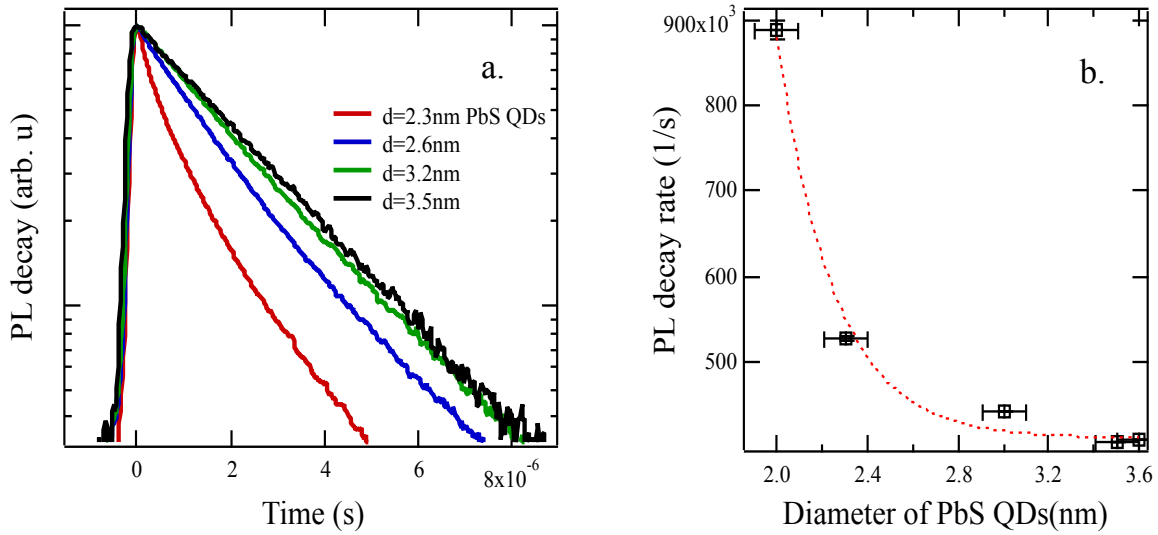

Figure 3.4: (a) PL decay of 2 nm (red), 2.3 nm (blue), 3 nm (green) and 3.5 nm (black) of oleic acid capped PbS QDs, (b) PL decay rate as function of the diameter of the oleic acid capped PbS QDs

The PL decays of PbS QDs of various sizes in solution are demonstrated in Figure 3.4a. The decay rates of the QDs exhibit a strong size dependence (Figure 3.4b) which is in agreement with the theory. In the strong confinement limit the electron-hole overlap grows monotonically with decreasing size. For the first exciton transition the oscillator strength (f_1) per QD tends to be inversely proportional to the volume of the sphere ($f_1 \rightarrow f_{ex}\frac{\pi a_B^3}{V}$, where f_{ex} is the exciton oscillation strength of the bulk crystal, a_B is the Bohr radius and V the volume of the QD). The

radiative decay time is proportional to the oscillation strength and therefore obeys the $\tau_{rad} \propto a^{-3}$ dependence as well.

3.3.2 Size and temperature dependent dynamic of oleic acid capped PbS QDs deposited on a glass substrate

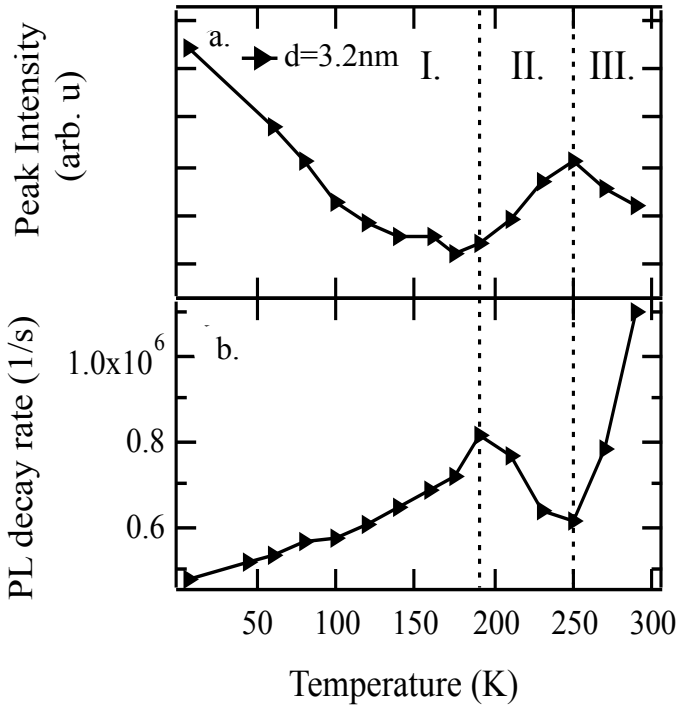

Figure 3.5: PL peak intensity (a) and PL decay rate (b) of the oleic acid capped PbS QDs with diameter 3.2nm, as a function of temperature

Spectral and time-resolved measurements were performed for spin coated oleic acid capped PbS QDs (at a concentration of 5 mgr/mL) on glass substrates in order to study the size and temperature dependent dynamics of oleic acid capped PbS QDs. The PL decay rate and intensity maxima of the PbS QDs are illustrated in Figure 3.5, and both are shown to exhibit strong temperature dependences in the 6 to 290 K range. The PL decay of this type of QDs appears to be double exponential, indicating the existence of two radiative relaxation channels: the transition from the dark to the ground state and from the bright to the ground state.

The trends of the intensity maxima and PL decays change at specific temperatures as is shown in Figure 3.5. Consequently, the analysis of the decay curves and the PL peak intensities were combined and three temperature regimes were identified: i) the low temperature regime corresponds to temperatures below 180 K, the intermediate regime refers to temperatures between 180 and 250K, and the high temperature regime relates to temperatures above 250 K.

The low temperature regime (<180 K) is characterized by a decrease in PL intensity and an increase in the average decay rate. As the temperature increases, more carriers populate the bright state at the expense of the dark state, which can then efficiently radiatively relax to the ground state. As the radiative relaxation of carriers from the bright state dominates with the increase of temperature, one would expect the increase of the integrated intensity would also increase. However, it is observed that the maximum intensity decreases for larger temperatures. Temperature quenching of the PL of QDs is a commonly observed phenomenon, both in colloidal suspensions or in solvent free systems such as QDs deposited on glass substrates, and is attributed to surface states [106]. The carriers with thermal energy larger than the energy difference between the surface state and bright state or surface state and dark state can transit to the trap state with the absorption of phonons. The carriers of the surface state are trapped and consequently the overall number of carriers, which relax radiatively is reduced.

For the 180 to 250 K temperature range, the PL intensities recover and the average decay rate decreases, while for temperatures above 250 K, the PL intensity quenches and the average PL decay rate increases again. These three regimes were observed for all PbS QD sizes (Figure 3.5).

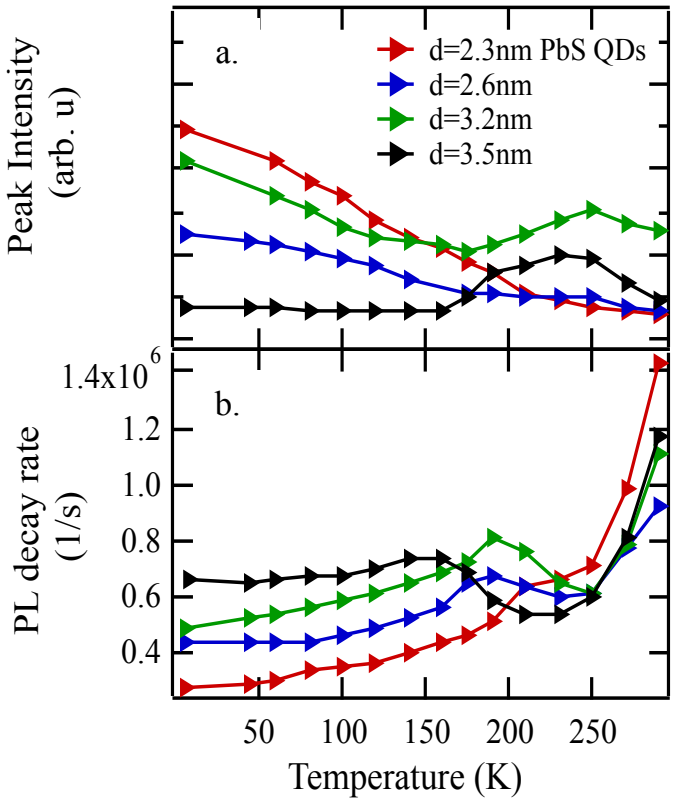

Figure 3.6: PL peak intensity (a) and PL decay rate (b) of oleic acid capped PbS QDs with a diameter of 2.3 nm (red), 2.6 nm (blue), 3.2 nm (green) and 3.5 nm (black) as a function of temperature

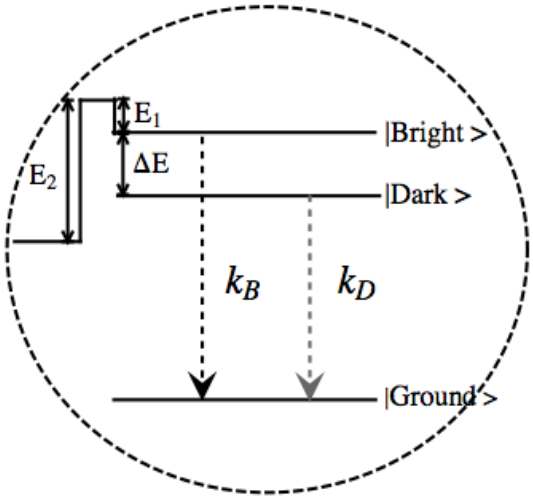

Figure 3.7: A schematic representation of the exciton relaxation processes

To describe the temperature-dependence of the exciton PL in oleic acid capped PbS QDs, a simple model is proposed, which is summarized in Figure 3.7. The fine structure of the lowest exciton state is represented by a bright and a dark state with radiative decay rates k_B and k_D, respectively. The energy splitting ΔE between these two states is in the range of a few meV, depending on the size and shape of the QDs [83]. A trap surface state as described in Figure 3.7 is introduced. A barrier of height E_1 from the bright to the trap state prevents total quenching of the bright states rendering this surface state thermally activated [107].

According to the proposed model, the increase in PL decay rate in the first regime is due to the splitting between the dark and the bright state, as it has been previously reported [106]. As the temperature increases, exciton relaxation rate (k_B) from the bright to ground state dominates over the radiative relaxation channel from the dark to the ground state, and consequently, the average lifetime is increased. On the other hand, the PL peak intensity decreases as the temperature increases because of the existence of the surface state. Carriers with thermal energy $K_B T_e \geq E_1$ become trapped and consequently decrease the total number of carriers which relax radiatively (we assume that $E_1 < E_2$). For temperatures above 180 K (regime 2) the thermal energy of the trapped carriers is sufficient to overcome the barrier of E_2, populating the dark and the bright states, which can relax to the ground state and increase the PL peak intensity. In the third regime we observe that the PL intensity is quenched suggesting the existence of a non-radiative channel from the trap state. This non-radiative channel helps carriers with thermal energy higher than the escape energy to escape from the particle. The average lifetime shows a complex trend for temperatures above 180 K due to the interplay between trapping and detrapping rates.

The non-radiative relaxation probabilities from the bright (κ_{B-T}) and dark state (κ_{D-T}) to the trap state with the absorption or emission of phonons are calculated from:

$$\kappa_{B-T} = k_o \left(\exp\left(\frac{E_{ph}}{K_B T}\right) - 1\right)^{-\frac{E_1}{E_{ph}}} * \left(\frac{\exp\left(\frac{E_{ph}}{K_B T}\right)}{\left(\exp\left(\frac{E_{ph}}{K_B T}\right) - 1\right)}\right)^{\frac{E_2}{E_{ph}}} \tag{3.5}$$

and $$\kappa_{D-T} = k_o \left(\exp\left(\frac{E_{ph}}{K_B T}\right) - 1\right)^{-\frac{E_1+\Delta E}{E_{ph}}} * \left(\frac{\exp\left(\frac{E_{ph}}{K_B T}\right)}{\left(\exp\left(\frac{E_{ph}}{K_B T}\right)-1\right)}\right)^{\frac{E_2}{E_{ph}}} \quad (3.6)$$

where k_o is a rate constant, which characterizes the efficiency of the thermally induced non-radiative relaxation processes, $(\exp\left(\frac{E_{ph}}{k_B T}\right) - 1)^{-1}$ is the probability of a carrier to absorb a phonon of energy E_{ph} according to the Bose-Einstein distribution, and $\frac{\exp\left(\frac{E_{ph}}{k_B T}\right)}{\left(\exp\left(\frac{E_{ph}}{k_B T}\right)-1\right)}$ is the probability to emit a phonon of energy E_{ph}. Non-radiative processes also take place from trap to bright (κ_{T-B}) and dark (κ_{T-D}) states with rates given by

$$\kappa_{T-B} = k_o \left(\exp\left(\frac{E_{ph}}{K_B T}\right) - 1\right)^{-\frac{E_2}{E_{ph}}} * \left(\frac{\exp\left(\frac{E_{ph}}{K_B T}\right)}{\left(\exp\left(\frac{E_{ph}}{K_B T}\right)-1\right)}\right)^{\frac{E_1}{E_{ph}}} \quad (3.7)$$

$$\kappa_{T-D} = k_o \left(\exp\left(\frac{E_{ph}}{K_B T}\right) - 1\right)^{-\frac{E_2}{E_{ph}}} * \left(\frac{\exp\left(\frac{E_{ph}}{K_B T}\right)}{\left(\exp\left(\frac{E_{ph}}{K_B T}\right)-1\right)}\right)^{\frac{E_1+\Delta E}{E_{ph}}} \quad (3.8),$$

while carriers from the trap state can thermally escape the dot with a rate

$$k_{esc} = k_o \left(\exp\left(\frac{E_{ph}}{K_B T}\right) - 1\right)^{-\frac{E_{esc}}{E_{ph}}} \quad (3.9)$$

where E_{esc} is the energy required for a carrier to escape from the surface state of the QDs.

Furthermore, the transition of a carrier from dark to bright states (κ_{D-B}) as well as the transition from bright to dark state (κ_{B-D}) is considered by the absorption or emission of phonons. The corresponding non-radiative rates are described by

$$\kappa_{D-B} = k_o \left(\exp\left(\frac{E_{ph}}{K_B T}\right) - 1\right)^{-\frac{\Delta E}{E_{ph}}} \quad (3.10)$$

$$\kappa_{B-D} = k_o \left(\exp\left(\frac{E_{ph}}{K_B T}\right) / \left(\exp\left(\frac{E_{ph}}{K_B T}\right) - 1\right)\right)^{\frac{\Delta E}{E_{ph}}} \quad (3.11)$$

Having determined the different rates, we write the differential equations describing the populations of the dark, bright and trap state:

$$\frac{dn_{bright}}{dt} = -(k_B + k_{B-T} + k_{B-D}) * n_{bright} + k_{D-B} * n_{dark} + k_{T-B} * n_{trap}$$

$$\frac{dn_{dark}}{dt} = k_{B-D} * n_{bright} - (k_D + k_{D-T} + k_{D-B}) * n_{dark} + k_{T-D} * n_{trap}$$

$$\frac{dn_{trap}}{dt} = k_{B-T} * n_{bright} + k_{D-T} * n_{dark} - (k_{T-D} + k_{T-B} + k_{esc}) * n_{trap} \quad (3.12)$$

where n_{bright}, n_{dark} and n_{trap} are the carrier populations of the bright, dark and trap states, which are time and temperature dependent, and k_B, k_D are the rates of the radiative relaxation of carriers from the bright and dark state, respectively.

The initial population of the bright and dark states is set to follow the Boltzmann distribution $\frac{n_{bright}}{n_{dark}} = e^{\frac{-\Delta E}{K_B T}}$ (3.13), while the total number of carriers at t=0 is

$$N_{total}(t = 0) = n_{bright} + n_{dark} \quad (3.14)$$

By combining the equations 3.13 and 3.14, the initial population of the bright and dark state are calculated:

$$n_{bright}(t = 0, T) = \frac{e^{\frac{-\Delta E}{K_B T}} * N_{total}}{(e^{\frac{-\Delta E}{K_B T}} + 1)},$$

$$n_{dark}(t = 0, T) = \frac{N_{total}}{e^{\frac{-\Delta E}{K_B T}}} \quad (3.15)$$

Nevertheless, it is noted that the overall dynamics will be independent of the initial carrier distribution and can only be affected by the thermal energy of the carriers and therefore the temperature. In the linear excitation density regime the total number of carrier per QD is one. The integrated PL intensity is equal to the number of photons, and consequently, the number of excitons ($n_{exciton,r}$) which relax radiatevely. Therefore, the integrated PL is obtained from the solution of the differential equation

$$\frac{dn_{exciton,r}}{dt} = k_B * n_{bright} + k_D * n_{dark} \quad (3.16)$$

while the PL decay is given by the sum of ($k_B * n_{bright} + k_D * n_{dark}$).

We applied the above model to our experimental data. We set E_{ph} equal to the LO-phonon energy $E_{LO} = 26.6$ meV. The best fit was found for the following set of parameters, presented in Table 3.1 for all the various sizes of PbS QDs, while the fittings are shown in Figure 3.8.

Table 3.1: Fitting parameters of the energy levels and the carriers rates in PbS QDs

	ΔE (meV)	**E_1** (meV)	**E_2** (meV)	**E_{esc}** (meV)	**k_B** (s^{-1})	**k_D** (s^{-1})	**k_o** (s^{-1})
d=2.3 nm	3	7	115	10	10^6	$6*10^4$	$4*10^5$
d=2.6 nm	3	4.5	115	95	$1.6*10^6$	$1.5*10^4$	$1.5*10^6$
d=3.2 nm	3	3	95	110	$1.7*10^6$	$1.5*10^4$	$1.5*10^6$
d=3.5 nm	2	1	60	120	$2*10^6$	$0.8*10^4$	$1.5*10^6$

The bright-dark state energy splitting ΔE was estimated to be equal to 3 meV for most of the particles, while it decreased to 2 meV for the 3.5 nm diameter particles. As it was mentioned in Chapter 2, the electron-hole exchange interaction splits the lowest excited state into dark and bright states and is proportional to the overlap of the electron-hole wavefunction. The overlap between the electron-hole wavefunction increases for smaller particles and hence a strong size dependent splitting is expected. However, the PbS QDs exhibit variations from the perfect spherical shape which can affect the size dependent splitting. A shape dependence of the bright-dark splitting has been predicted by Efros *et al.* [82]. Kang I. *et al.* [83], estimated the lowest direct exciton splitting for PbS QDs, by considering the effect of Coulomb and exchange interactions. For a bulk exchange strength of 10 meV the dark-bright splitting was calculated to be around 4 meV for 2nm diameter PbS particles, a value close to the one estimated from our simulations [83]. The estimated value of the bright-dark energy gap (ΔE=3 meV) is lower than the value reported by similar investigations for PbS QDs embedded in glass substrates [106] but remains in good agreement with the theoretical predictions mentioned previously.

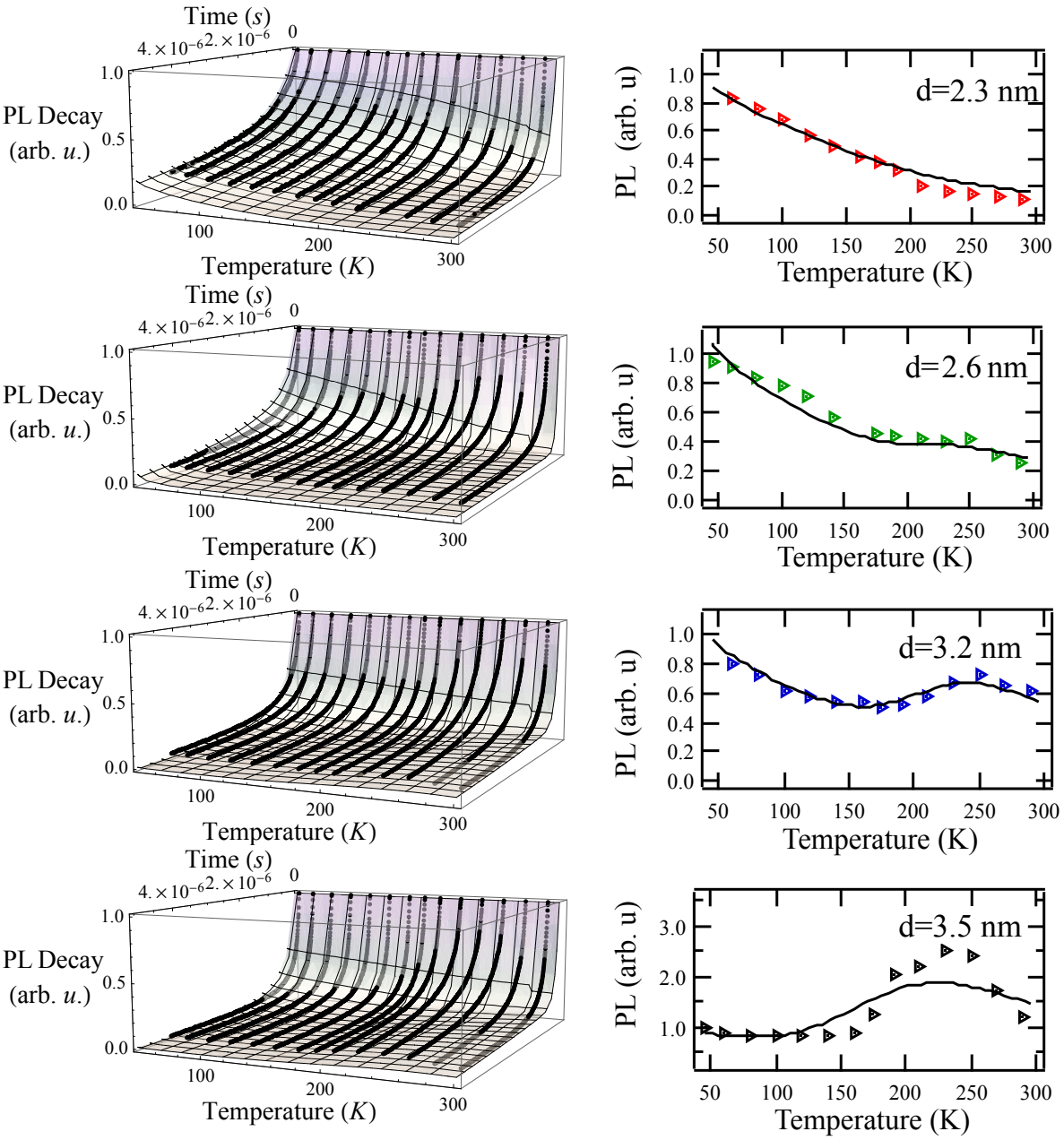

Figure 3.8: PL decay curves and PL peak intensity fitted with the proposed theoretical model for PbS QDs of (a) 2.3 nm, (b) 2.6 nm, (c) 3.2 nm and (d) 3.5 nm diameter.

The exciton lifetimes of the dark state were observed to range between 60 ms and 8 ms for different sizes of PbS QDs. Within the effective mass approximation the singlet (dark) exciton lifetimes are described to be size independent and radiationless. Nevertheless, the finite observed lifetimes could be explained by considering the spin orbit coupling, QD asymmetry and the associated violation of selection rules. The spin-orbit coupling as well as the asymmetric shape

of the QDs change the excitonic fine structure splitting and consequently lead to a mixing of dark and bright excitons states. Through this process the latter acquire finite optical oscillator strength, leading to measurable dark exciton lifetimes. With increasing QD size we observe a trend of decreasing radiative dark exciton rates as it should be expected towards the limit of an infinitely large crystal (bulk) where dark states are forbidden optical transitions. The transfer of optical oscillator strength from the bright to dark states is also evident in the size dependence of the radiative rate of bright excitons. Indeed, we observe that the radiative rate of bright excitons follows the opposite trend to that of dark excitons, namely an increasing radiative rate with increasing size of QDs.

The energy of the trap states of the oleic acid capped PbS QDs was found to decrease with increasing QD size. This trend could be due to the deformation of the crystal lattice and the increasing number of dangling bonds in the outer atoms as the size of the QDs decreases. The escape energy, which describes the thermal energy needed for a carrier to escape the surface of the QD, was shown to decrease for smaller nanocrystals. The k_o rate, which introduces the efficiency of the thermal non-radiative relaxation processes, was constant for most of the QD sizes. The higher value found for the smallest QDs can be explained by the increase in the confinement and the associated modification of the electron-phonon coupling constant [83].

3.4 Energy Transfer from oleic acid capped PbS QDs to silicon

3.4.1 Donor-acceptor separation dependence in energy transfer

Hybrid structures of oleic acid capped PbS QDs deposited on substrates consisting of SiO_2 thin films of various thicknesses on silicon were used for the study of RET from PbS QDs to bulk silicon, as illustrated in Figure 3.9. It has been mentioned in Chapter 2 that RET mechanism depends on the separation distance between donor and acceptor, the spectra overlap between the emission spectrum of the donor and the absorption spectrum of the acceptor, as well as their dipole orientation angles.

The absorption and emission spectrum of the PbS QDs used in this experiment are shown in Figure 3.10a. These particles are excellent solar absorbers due to the match of their absorption spectrum with the solar radiation (Figure 3.10b).

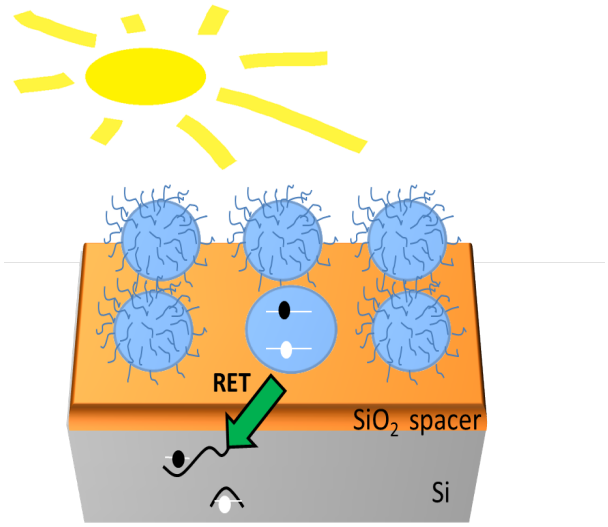

Figure 3.9: Schematic description of the RET mechanism from oleic acid capped PbS QDs to bulk silicon substrate

RET mechanism can be detected by measuring acceleration in the PL decay of the donor or a slightly temporal shift in the PL decay of the acceptor. As silicon is an indirect band gap semiconductor the emission of silicon at room temperature is negligible and consequently the PL decay of PbS QDs is only recorded for the study of RET from the PbS QDs to silicon. The PL lifetimes of the deposited oleic acid capped PbS QDs with an excitonic peak at ~ 800 nm were measured for different SiO_2/Si samples where the thickness of the SiO_2 spacer was varied from 5 to 56 nm (Figure 1a). Time-resolved measurements were performed using the setup described in section 3.1.1. The PbS QDs were excited at 400 nm, with a 81 kHz repetition rate. It is observed that the PL decay of the PbS QDs was shorter for thinner SiO_2 layers as shown in Figure 3.11.

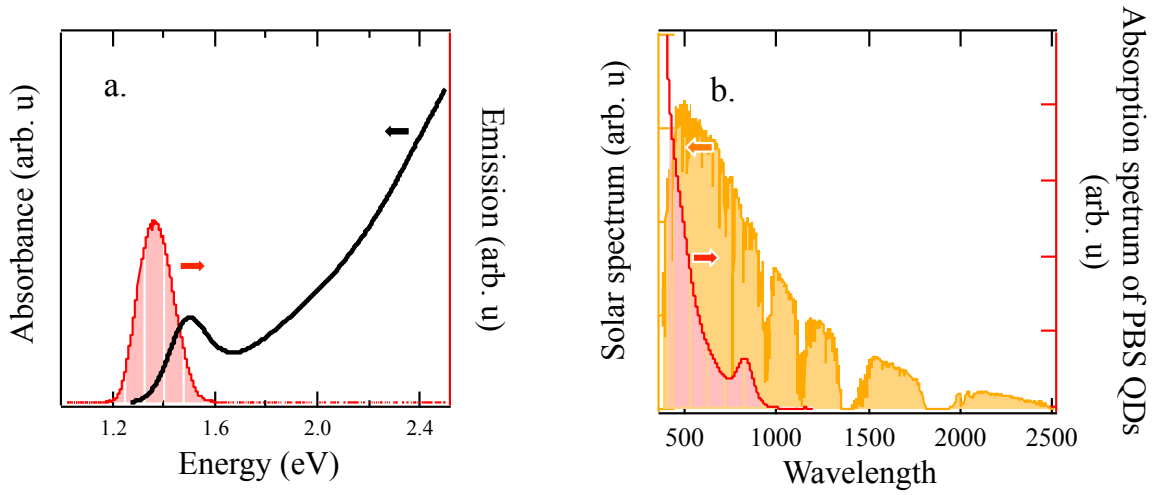

Figure 3.10: (a) PL and absorption spectra of oleic acid capped PbS QDs, (b) The solar spectrum (orange colour) plotted with the absorption spectrum of PbS QDs (red colour)

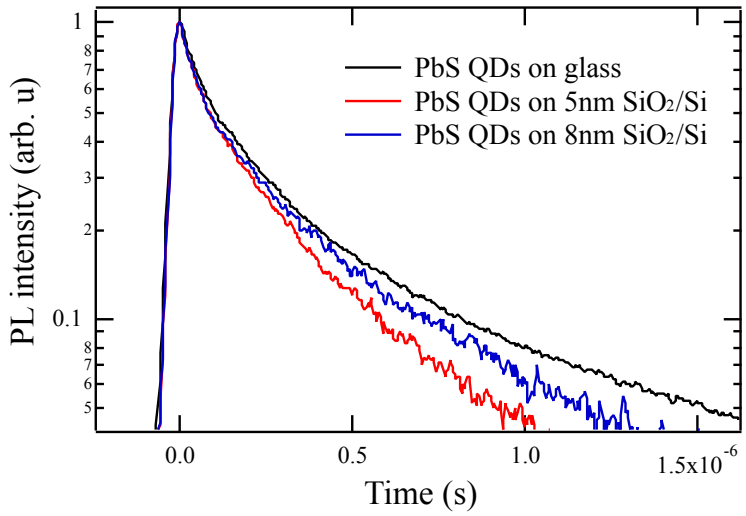

Figure 3.11: PL decay of oleic acid capped PbS QDs deposited on glass (black), 5 nm SiO_2/Si (red) and 8 nm SiO_2/Si (blue) substrate

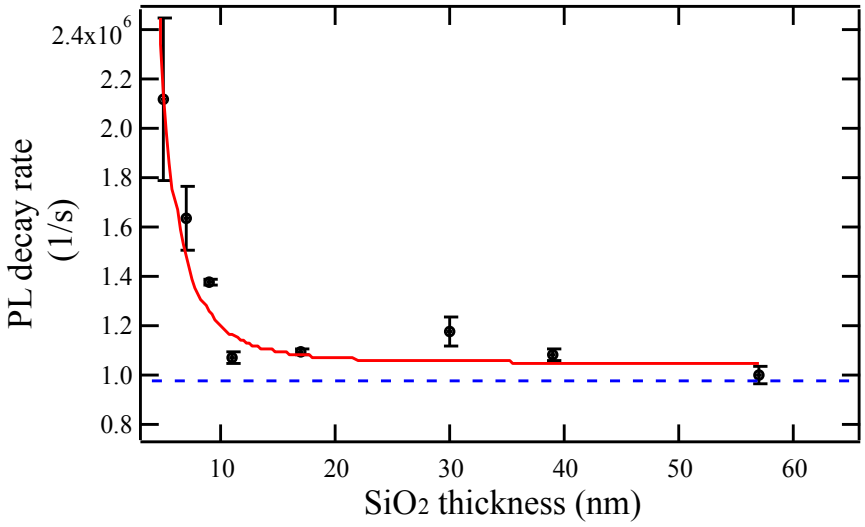

Figure 3.12: PL decay rate of oleic acid capped PbS QDs plotted as a function of spacer thickness. The blue dashed line shows the PL decay rate of PbS nanoparticles deposited on glass. The red line illustrates the fitting with an R^{-3} function.

The PL decays of the PbS QDs described with a stretched exponential or bi-exponential function. We calculate the average lifetimes of the PL decays by fitting them with a stretched exponential function, an equation widely used for analysis of energy transfer:

$$I_{PL} = C + A \exp\left(-\left(\frac{t}{\tau}\right)^{\beta}\right) \tag{3.17}$$

The average lifetime of the different PL components is given by:

$$\langle\tau\rangle = \frac{\tau_1}{\beta}\Gamma\left(\frac{1}{\beta}\right) \tag{3.18}$$

where Γ represents the gamma function. The PL decay rate is given by $k = \frac{1}{<\tau>}$. The PL dynamics of the PbS QDs differ significantly for the different substrates. The full dependence of the PL decay rate for a variety of SiO_2 spacing thickness is shown in Figure 3.12. The PL decay rate increases for SiO_2 spacer thicknesses below 12 nm. It then remains almost constant for SiO_2 spacer thicknesses greater than 12 nm, with values comparable to the decay rate of PbS QDs deposited on a glass substrate. The observed acceleration in the lifetimes of PbS QDs for short separation distances is a strong evidence of RET from the QDs to the bulk silicon.

At distances greater than 12 nm, there is no net absorption of energy by the silicon and the decay rate of the PbS QDs is almost equal to the value on glass (absence of an absorbing semiconductor). At distances below 12 nm, the lifetime is sharply reduced due to transfer energy to the silicon. The near field of the PbS QDs can directly excite a vertical transition in the semiconductor band structure. In this regime, it is observed that the lifetime of PbS QDs decreases inversely with the third power of the thickness of the spacer. This is in agreement with previous studies that recorded RET from a dye molecule to bulk Silicon[108] and also as expected theoretically for RET from a point dipole to a continuum of absorbing exciton states[109].

3.4.2 Temperature dependence of energy transfer in oleic acid capped PbS QDs-silicon hybrid structures

Temperature dependent measurements were performed in three different samples: PbS QDs deposited on a 5 nm SiO_2 spacer-silicon substrate, a 20 nm SiO_2 spacer-silicon substrate and on a glass substrate. The behavior of the average decay rate for these three different samples is illustrated in Figure 3.13.

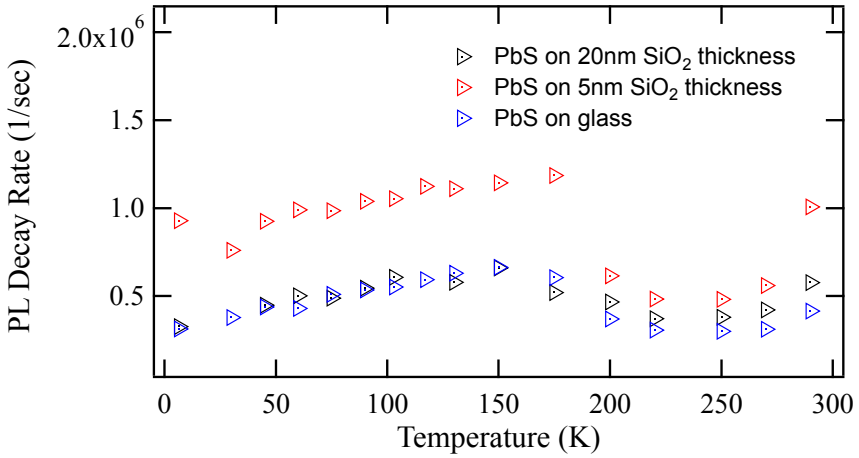

Figure 3.13: Average PL decay rate of oleic acid caped PbS QDs deposited on glass substrate (blue markers) and on 5 nm (red markers), and 20 nm SiO2/Si substrates (black markers) as function of the temperature

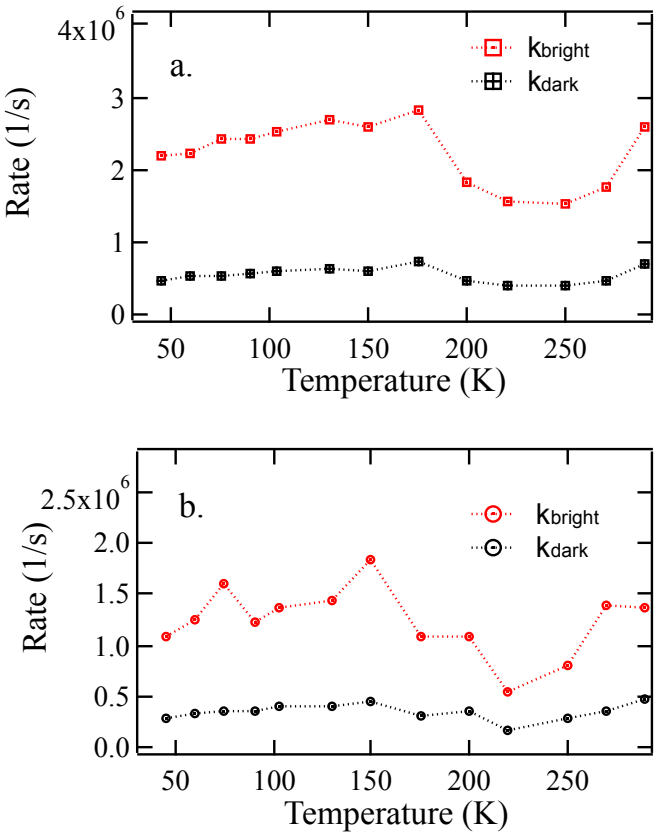

Figure 3.14: Bright (red) and dark (black) rates of oleic acid caped PbS QDs deposited on (a) 5 nm and (b) 20 nm SiO_2/Si substrates as function of the temperature

The average decay rate of the PbS QDs exhibits a similar trend for the different samples, which is attributed to the electronic structure of PbS QDs. The observed trend has been extensively explained in section 3.2.2, where it was shown that the radiative decay rate of bright excitons is around two orders of magnitude larger than the rate of dark excitons. It is therefore understood that in the framework of RET the bright excitons dominate the dynamics. To derive the energy transfer dynamics from PbS QDs to crystalline silicon as a function of temperature we decouple the contribution of bright and dark exciton from the observed PL by fitting the decay dynamics using a bi-excponential function. The fast and slow components correspond to bright and dark exciton dynamics respectively as shown in Figure 3.14a for 5 nm and Figure 3.14b for 20 nm SiO_2 separation layer. The RET rate and the efficiency of the process as function of temperature is shown in Figure 3.15. The RET rate at the different temperatures is extracted from the relation:

$$k_H = k_{PbS} + k_{RET} \tag{3.19}$$

and the RET efficiency is calculated according to the equation $\eta = \frac{k_{RET}}{k_H}$, where k_H is the rate of PbS QDs deposited on the 5 nm SiO_2 spacer/Si sample, k_{PbS} is the rate of PbS QDs deposited on the 20 nm SiO_2 spacer/Si sample and k_{RET} the RET rate. As expectedly we observe that the RET rate and the efficiency of the process depends only weakly on temperature due to the temperature independent nature of the radiative rates.

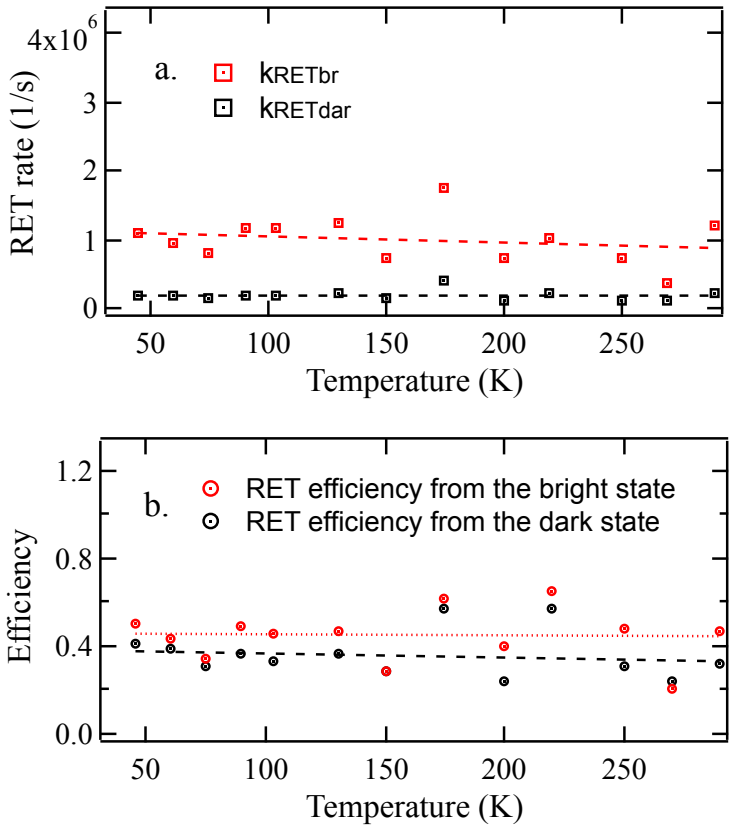

Figure 3.15: (a) Calculated RET rate from the radiative rates of the dark state (black) and bright (red) state as function of the temperature; (b) Efficiency of RET process attributed by the dark (black) and bright (red) state as function of the temperature.

In conclusion, RET mechanism occur from PbS QDs to bulk silicon with temperature constant efficiency of 46%. In the case of the hybrid photovoltaic devices, the number of the absorbed photons will be significant higher compared to the plane silicon devices, due to the presence of the PbS QDs, while the efficiency of the carrier extraction is the same in both cases. As it was mentioned previously, the absorption spectrum of PbS QDs match with the solar radiation and

this type of particles can be used for the creation of exciton by the absorption of low energy solar photon. Consequently, the number of exciton in the QDs that their energy is transferred to silicon by creating electron-hole pair (with efficiency 46%), can in overall increase the quantum efficiency of silicon photovoltaics. In contract comparison, the absorption spectrum of QDs such as CdSe, CdS or CdSe/CdS heterostructures, do not extend into the near infrared and consequently part of the solar radiation is not utilized for the creation of carriers.

3.5 Conclusions

In this chapter, the exciton dynamics of oleic acid PbS QDs was studied and their use as optical absorbers for non-radiative injection of carriers into the silicon was demonstrated. The size and temperature dependence of exciton dynamics in PbS QDs on a glass substrate was studied. Three difference regimes were recognized, regardless the size of the particles. The low temperature regime (<180 K) was governed by an increase in the average decay rate due to the Boltzmann distribution of carriers between the dark and bright state, and a quench in the PL intensity explained by the existence of a surface state. The intermediate regime (~180-250 K) is described by an enhancement in the PL due to the return of the trapped carriers to the dark and bright states while the PL rate decreases indicating an increase in dark radiative transitions at the expense of bright transitions. The PL intensity is quenched again in the high-temperature regime (>250 K) due to the enhanced non-radiative processes while the PL rate increases demonstrating that the bright to ground transition dominates. Our experimental results were fitted with a simple model and we estimated that the lowest energy splitting for the smallest particles is 3 meV. The simplicity of this model and its capacity to explain the observed non-monotonous intensity and fluorescence decay rate dynamics of PbS colloidal QDs increases our confidence in the validity of the converged parameters describing the exciton fine structure.

It is also demonstrated that RET form PbS QDs to silicon substrates can be an efficient process. The presence of RET between the PbS nanocrystals and the silicon substrate was studied by measuring the PL lifetime of PbS particles deposited on silicon capped by a SiO_2 spacing layer. It is observed that the PL decay rate was significantly quenched for spacer thicknesses below 12 nm and the RET rate was found to change with the inverse cube of the distance between the PbS QDs and the silicon. For a spacer thickness greater than 12 nm the decay rate was equal to the

value measured from PbS QDs deposited on a glass substrate. These results undoubtedly identify RET from colloidal QDs to bulk silicon. Time-resolved measurements for a range of temperatures were also presented for PbS QDs deposited on glass and silicon with 5 nm and 20 nm spacer thicknesses substrates. Our findings show that the RET mechanism could be used for the development of thin film hybrid photovoltaic devices that could potentially overcome the low solar absorption of thin film crystalline silicon.

Chapter 4: Single-mode tunable laser emission from CdSe/CdS core/shell colloidal quantum rods on spherical silica microcavities

Colloidal elongated core/shell hetero-nanocrystals have been widely studied and used in a range of applications such as light harvesting, lasers and biolabelling [4]. These structures consist of a semiconductor core that is covered with a thin shell of another type of the semiconductor material. The band alignment at the interface of these two materials could be such that the energy levels of the valence and conduction band edges of the core material are located inside the shell material, or only one of the band edges of the core material is located in the gap of the shell material [4]. The second case leads to type II intermediate confinement regime where one of the carriers is confined into the core and the other one into the shell (Section 2.1.3). As, it was described in Section 2.1.6, the spatial separation of the carriers creates an electric field within their volume which induces a Stark-shift of the absorption wavelength with respect to the emission one and hence gain can be observed by a single exciton [44].

On the contrary, the gain optical mechanism in bare QDs such as PbS, CdSe ect, requires the creation of multi-excitons. This is due to the fact that single excited electron leads to optical transparency because of the absorption of the created photon by the remaining electron in the ground state. In this case the induced Stark shift by the excited electron is not greater than the linewidth of the excited state due to the spatial overlap of the electron-hole wavefunction. Therefore the absorption energy of the remaining electron in the ground state is similar to the first excited electron and optical gain can be achieved with at least two electrons excited (biexcitons).

The potential of core/shell nanocrystals for lasing applications is further enhanced with respect to bare QDs, because the shell protect the core from photodegradation and thereby ensures significantly higher PL quantum yields and larger absorption cross section [2]. Specifically, the quantum efficiency of the QDs is mainly reduced due to the thermal ionization (carrier in a trap state) and the Auger effects [110]. In the case of core/shell QDs, the shell further insolates the surface of the nanocrystals and reduces the presence of the surface states resulting in an enhanced photoluminescence. In the strong confinement, the Auger autoionization or other ionization processes are greatly enhanced. Auger effect is a physical phenomenon where an electron is removed leaving a vacancy where can be occupied by an electron of high energy level and result in a release of energy. Most of the times this energy is released with the emission of

photon, however can also be transferred to another electron which is excited. Auger effects induce non-radiative processes where the excess of a charge carrier quenches the radiative recombination of the electron-hole pairs. Chalcogenide QDs are characterized by the strong confinement of the electron-hole pair and enhanced Auger recombinations. On the other hand, Auger recombinations in type II core shell QRs are significantly reduced indicating this type of material important for laser applications.

In this chapter, the tuneable emission from microscale lasers based on silica spheres coated with colloidal CdSe/CdS core/shell QRs using a fiber taper coupling scheme for the pump light is demonstrated. The lasers operate at room temperature and coupling of the nanocrystals' emission with the WGMs of the microsphere can be precisely tailored by the pump coupling conditions, leading in laser emission with controllable modality. Using an infrared (IR) femtosecond laser as a heating source, the single-mode emission wavelength was tuned over a maximum range of 2.1 nm. The observed wavelength shift is satisfactorily explained by means of a simple model that has been developed.

Such type of microlaser can be incorporated in a microfluidic flow system and used as biosensors. The microfluidic could be functionalized with receptor biomolecules, such as antibodies, streptavidin, aptamers and enzymes, which interact with specific fluorescent labeled analytes. The microlaser can then excite the fluorescent molecules attached on the analytes. By recording the fluorescence of these molecules, the presence of the analyte can be quantified. Another type of biosensor can be achieved if the micro-resonator is covered by functionalized QDs with proteins, DNA etc. The receptor, then, interacts with the analyte and as a consequence, the intensity will be quenched and the formed laser line will be spectrally shifted.

4.1 Material and methods

4.1.1 Fabrication of CdSe/CdS QRs

Colloidal CdSe/CdS QRs were synthesized with the seeded-type growth method at high temperatures in suitable surfactant mixtures. This approach offers reproducibility in size and shape and avoids aggregation effects of the QRs. The whole process consists of two distinct

steps; the synthesis of the monodisperse spherical core (CdSe) and then their coating with CdS shells.

Synthesis of CdSe seeds: To synthesize the CdSe seeds, trioctylphosphine oxide (TOPO), octadecylphosphonic acid (ODPA) and cadmium oxide (CdO) were mixed in a container and the temperature was elevated to about 150 °C for approximately 1 hour. In order for CdO to be dissolved, the temperature was increased to 300 °C in nitrogen atmosphere. Trioctylphosphine (TOP) was subsequently introduced in the container followed by the injection of selenium (Se):TOP once the temperature reached the level of 370 °C and the incurring reaction led to the synthesis of the QDs. The QDs were then precipitated with methanol and washed by dissolution in toluene twice and finally dissolved in TOP.

Coating with CdS shells: CdSe/CdS QRs were produced by overgrowing the CdSe seeds with CdS shells using the seeded growth approach. This method requires the preparation of two solutions; the first containing TOPO, octylated diphenylamine (ODPA), hexylphosphonic acid (HPA) and CdO, and the second sulphide (S):TOP and CdSe QDs dissolved in TOP. The first solution was initially heated to a temperature of 150°C for about 1 hour under vacuum conditions. Then, the temperature was subsequently raised to a level of 350-380 °C and TOP was added into the solution. The second solution was then added to the mixture and the overgrowth process with CdS shells was allowed to proceed for about 6-8 minutes. The size and shape of the QRs fabricated with this method is highly reproducible due to the controlled parameters that determine the morphology of the QRs including the diameter of the seeds, the growth temperature, and the amount of precursors and seeds introduced in the solution. The used CdSe/CdS QRs were 27.7±2.2 nm long and 4.1±0.6 nm wide, defined by the SEM images illustrated in Figure 4.1a. These QRs exhibit emission and local absorption maxima at 616 nm and 610 nm respectively, as is shown in Figure 4.1b.

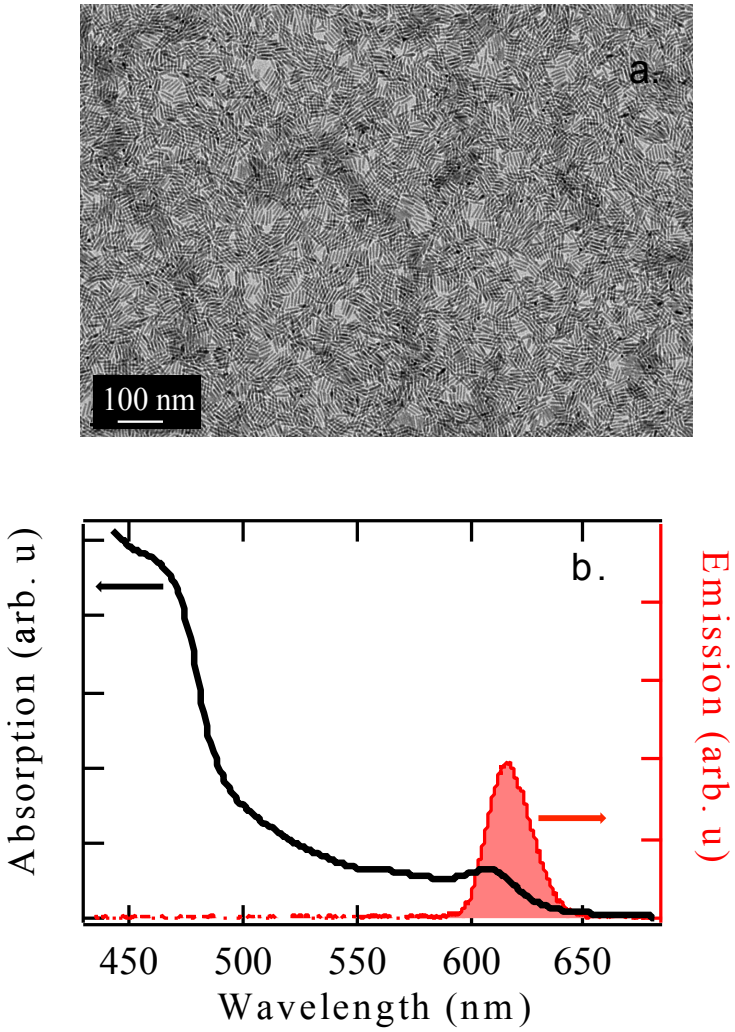

Figure 4.1: (a) SEM image of CdSe/CdS QRs, (b) absorption and emission spectrum of CdSe/CdS QRs

4.1.2 Fabrication of silica optical fiber tapers and microsphere templates

Tapers were fabricated according to the heat-and-pull technique, which involves heating of a section of the fiber with a microheater operated at 1100 °C. The fiber was initially heated and then its two ends were simultaneously pulled at opposite directions by a pair of computer-controlled translation stages of submicron precision. This method has the potential for producing taper transitions of well-defined lengths and shapes and extremely uniform waists.

4.1.3 Fabrication of microsphere resonators and coating with CdSe/CdS QRs

The microspheres were produced from standard silica optical fibers used for telecommunication applications and their outer diameters were smaller than the diameter of the host fiber. This was achieved by tapering a small region of the silica glass fiber, following the process described in section 4.1.2. Once the fiber elongation process was completed, the uniform waist tapered region formed was cut in its centre. One of the taper ends was then heated by a CO_2 laser beam to a temperature of about 900 °C. This temperature is higher than the softening point (540 °C) of the cladding glass and consequently the taper end was reflowed and moulded by producing a spherical shaped structure due to the surface tension was developed. During this process, the taper was rotated in order to ensure uniform heating of its end and prevented the stem to which the sphere remained attached, from bending. Due to the high viscosity of the silica glass, the reflowed structure is both highly spherical and extremely uniform while its surface has intrinsically very low roughness and hence very low scattering loss**.**

The microspheres studied had diameters from 8 to 40 μm and are illustrated in Figure 4.2. After the completion of the fabrication process they remained attached to their stems, which did not affect the optical modes in the equatorial plane. The Q factors of these microspheres were measured to be higher than 10^8.

The microspheres were coated by immersion in a toluene solution of the nanorods. After their withdrawal from the solution, they were left drying with their stems pointing down to ensure uniformity of the coating layer over their entire surface. The density of the QRs attached on the microsphere was controlled by varying the concentration of their initial solution, the time that the microsphere was into the solution and the withdrawal speed of the spheres from the solution. These parameters were defined by imaging the distribution of the QRs on planar silica substrates as is shown in Figure 4.3. The thickness of the coating was assumed to be approximately equal to the width of the nanorods (~ 4 nm).

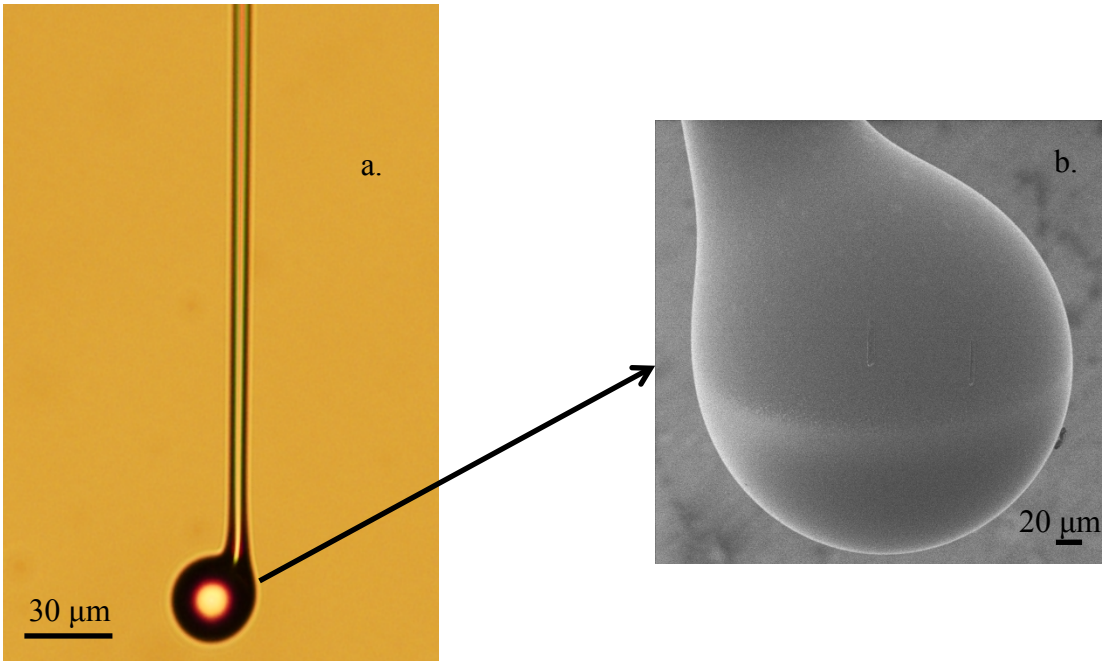

Figure 4.2: (a) Microscope image and (b) Helium-Ion microscope image of silica microspheres

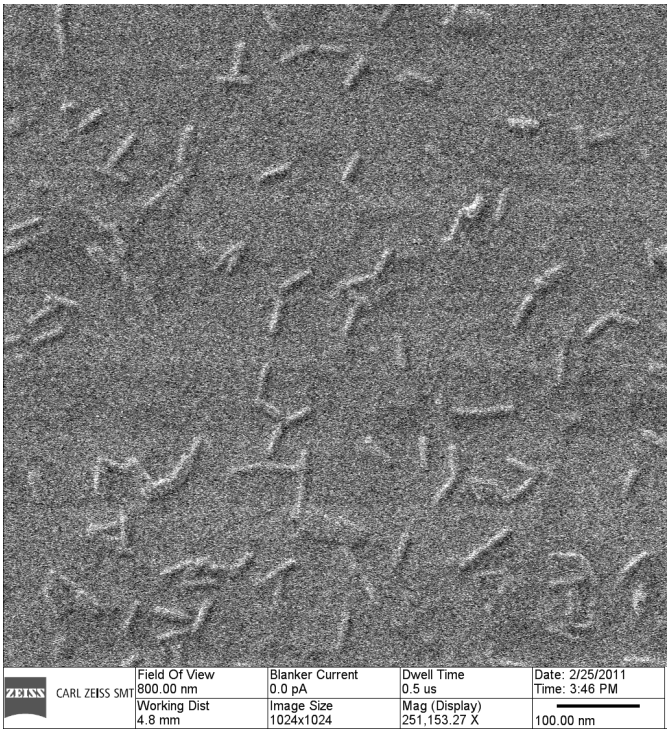

Figure 4.3: Hellium-Ion microscope image of CdSe/CdS QRs deposited on a silica substrate

4.1.4 Fabrication of tips

The fiber tips were manufactured by using a commercial micropipette puller (P-2000, Sutter Instrument), in which the heating source is a CO_2 laser and the whole pulling process is controlled by a microprocessor. The device configuration allows fabrication of tips with a diameter as small as 40 nm from fibers with a diameter of 125 μm which have a tapered transition length between 1 and 2 mm. Figure 4.4 shows the microscope image of a fiber tip produced with this procedure and used for the experiments described in this Chapter. The taper is ~2 mm and the tip diameter is ~50 nm.

Figure 4.4: Image of a fiber tip with diameter of 50 nm used to collect signals from the CdSe/CdS nanocrystal/silica microsphere hybrid resonators.

4.1.5 Experimental Setup

A schematic of the experimental setup used is shown in Figure 4.5. The spheres were pumped at 400 nm with a tuneable frequency doubled Ti:sapphire amplifier, operating at 250 KHz and emitting 180-fs-short pulses with a linewidth of 5 nm. The pump light was efficiently coupled to the circumference of microsphere resonators by a tapered fiber. The coupling via a tapered fiber for exciting the QRs can ensure: i) efficient coupling in and out of the pump and laser beam through the evanescent field and ii) selectivity in the excitation of the modes (i.e. fundamental or higher order modes). The tapers used for evanescent coupling were fabricated with the technique described in section 4.1.2. The taper was positioned on a high-resolution three-axis nano-positioning stage which allowed movement in close proximity from the microsphere and an overlap of the fundamental optical mode of the taper with the WGMs.

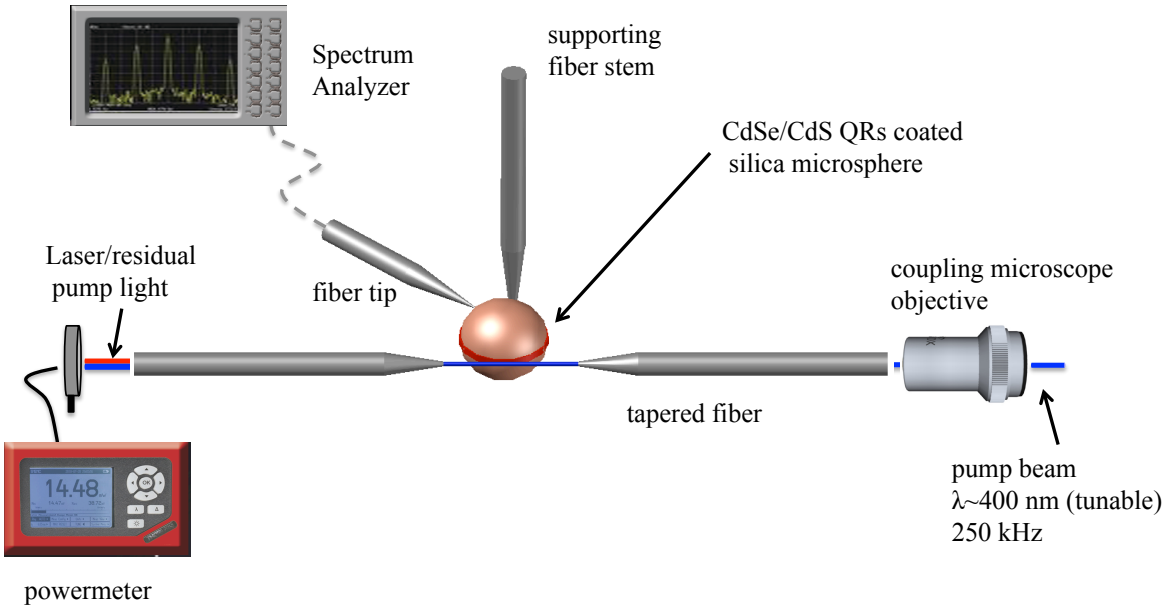

Figure 4.5: Schematic of the experimental arrangement used for demonstration of fiber-coupled laser operation of CdSe/CdS core/shell QRs in silica microspheres.

Laser signals were collected either by a probe fiber tip with a diameter of approximately 50 nm or with the same taper used for pumping, and spectra were recorded with an optical spectrum analyzer (OSA) [111]. The tip, which was fabricated with a micropipette puller, as described in section 4.1.4, was mounted on a three-dimensional high-precision micropositioner, in order to bring it into contact with the sphere and then move on the surface along a meridian to the desired plane. The coupling configuration was optimized to both reduce the laser threshold and obtain single-mode laser emission. For the microspheres used, coupling tapers had diameters ranging from 1 to 2 μm.

4.2 Single-mode laser emission from CdSe/CdS core/shell QRs

Resonant pumping of the fundamental WGM led to a single mode laser emission at 628.32 nm with a full-width-half-maximum (FWHM), $\Delta\lambda$ = 0.06 nm from the deposited CdSe/CdS QRs on the microsphere. Figure 4.6 shows the laser spectrum for the single-WGM operation at 628.32 nm of a microsphere with a diameter of 9.2 μm. The linewidth obtained suggests a Q factor value around ~10^5 for the coated microsphere. This value is significantly reduced compared to the measured Q factor before the microsphere coating (Q_o ~10^8). This reduction can be explained

considering the coating of the microsphere with the gain medium, which introduces roughness on the surface of the sphere and consequently induces scattering loss at the boundaries between the silica microsphere and the surrounding air. The presence of taper close to microsphere also reduces the Q factor of the resonator. It is very difficult, though to distinguish the losses due to the presence of the taper from the losses induced by the coating of the micro-resonator. An experimental method for determining the losses due to the presence of taper, is to couple the pump laser into the micro-resonator through a prism. The variation then, of the calculated Q factor through this method, will give evidence of the losses induced by the presence of the taper.

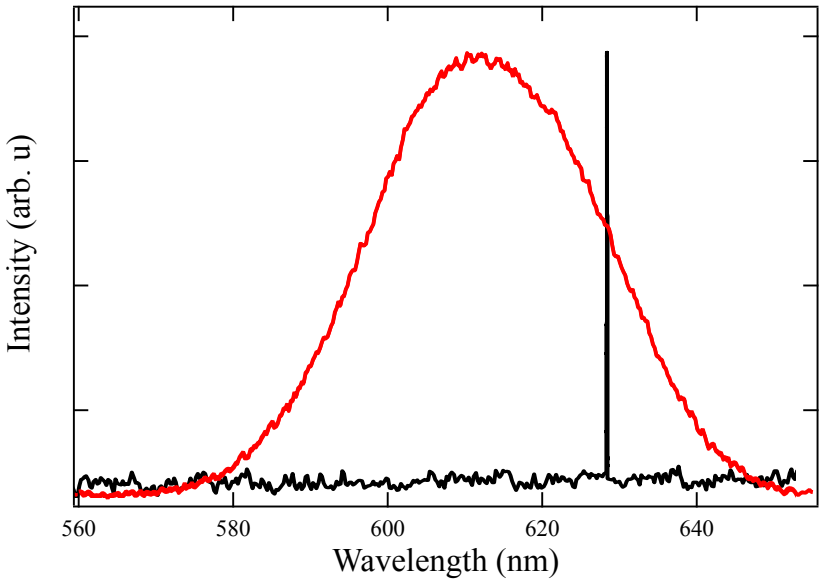

Figure 4.6: Laser emission at 628.32 nm (black line) and fluorescence emission (red line) spectra from the CdSe/CdS nanorods attached to 9.2 µm diameter sphere

The absorbed pump power threshold for single mode operation was 67.5 µW, which corresponds to pump fluence of 34.14 mJ/cm^2. Single-mode operation can be achieved by establishing phase matching conditions between the fundamental mode of the fiber and WGM. The pump laser spectral band also needs to encompass only one resonance frequency to ensure pumping of a single WGM. Other critical factors for single laser operation are the size of the microsphere template, the pump wavelength and bandwidth, the laser pump power and the gain bandwidth of the active medium.

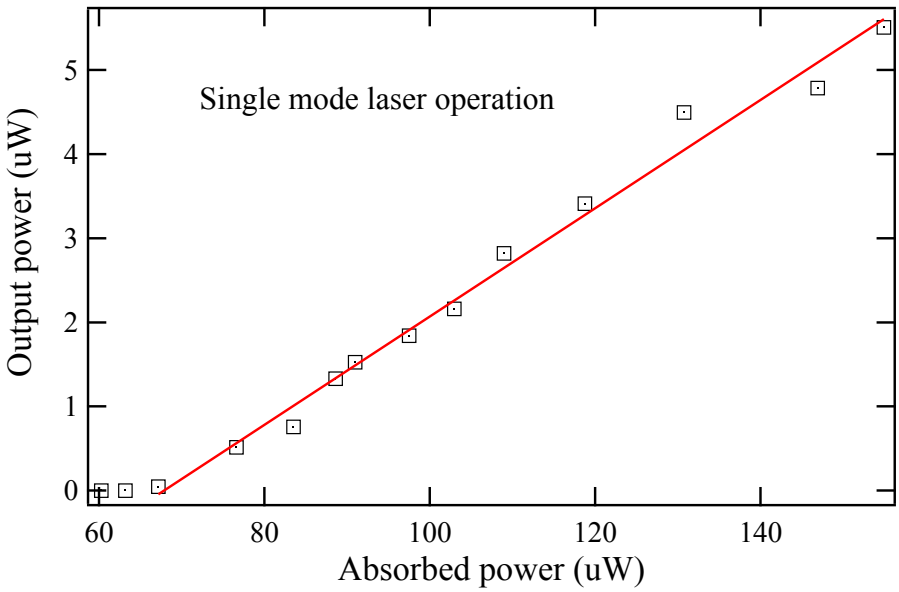

Figure 4.7: Laser output power as function of pump power for the single-mode laser operation of a 9.2 μm hybrid microsphere.

The laser output power as a function of absorbed pump power for single WGM operation for this microsphere is illustrated in Figure 4.7. The maximum output power was 5.5 μW and observed for 155 μW of absorbed power, which corresponds to a slope efficiency of 6.4 %. The absorbed pump power was estimated from the difference between the coupled power into the taper and the transmitted power after the taper. The power of the laser emission signal was measured at the end of the taper using a 530 nm long-pass filter in order for the pump laser to be removed.

It is worth calculating the number of QDs which participate in the observed laser line. From the Helium-Ion images, the density of particles is calculated and found equal to $1.69691*10^{14}$ particles/m^2. The particles cover an area of the microsphere equal to $2*\pi*r*\Delta x=2.8888*10^{-11}$ m^2, where r =4.6 μm is the radius of the microsphere and Δx is the thickness of the mode, which was considered approximately equal to the thickness of the taper ≈1 μm. Therefore, the total number of QRs attached in the microsphere in the area of the equatorial is 4902. The distribution of the different sizes of the QRs can be described by the fluorescence observed and plotted with red colour in Figure 4.6. The area under the red curve corresponds to the total number of particles. In

particular, the area between the wavelengths 628.2 nm and 628.4 nm will then correspond to the size of particles which contribute to the laser line at 628.32 nm. Consequently, multiplying the area between the wavelengths 628.2 nm and 628.4 nm with the total number of particles and dividing by the total area, gives ≈ 10 particles, which contribute to the laser line.

Evanescent coupling of the pump beam into the resonator away from its equatorial zone results in a multimode laser emission which is shown in Figure 4.8. A second set of laser-emissions can be observed at lower wavelengths, 592.5 nm and 585.76 nm, with respect to the peak observed in the single mode operation. The spectra difference between the first laser peak at 628.32 nm and the second set of laser peaks 585.76 nm and 593.5 nm cannot be explained by excitation of higher order modes.

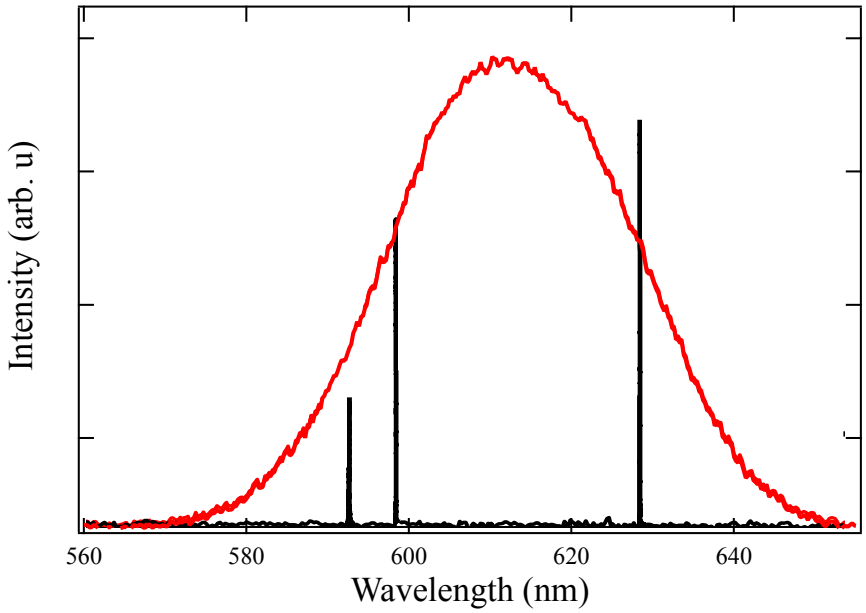

Figure 4.8: Multimode laser emission at 585.76, 592.5 and 628.32 nm (black lines) obtained for 120 µW absorbed power by non-equatorial pumping. The red curve corresponds to the emission spectrum of the deposited CdSe/CdS QRs on the microsphere.

In order to interpret the experimental results, we calculate the wavefunctions of the first excited state of the electron and the hole in the QRs using effective mass approximation method and considering the Coulomb interaction. In the case of single exciton, the Schrödinger equation is

used to calculate the wave function of the electron (ψ_e) and the hole (ψ_h) while the electric potential of the electron (Φ_e) and the hole (Φ_h) is calculated by the Poisson equation as follows:

$$\left[-\frac{\hbar^2}{2m_e^*}\nabla^2 + q_e(\Phi_h + V_{cb})\right]\psi_e = E_e\psi_e \tag{4.1}$$

$$\left[-\frac{\hbar^2}{2m_h^*}\nabla^2 + q_h(\Phi_e + V_{vb})\right]\psi_h = E_e\psi_h \tag{4.2}$$

$$\nabla^2\Phi_e = -\frac{\rho_e}{\varepsilon\varepsilon_o} \tag{4.3}$$

$$\nabla^2\Phi_h = -\frac{\rho_h}{\varepsilon\varepsilon_o} \tag{4.4}$$

where m_e^*, m_h^* are the effective masses of the electron and the hole respectively which are material dependent ($m_e^* = 0.13 * m_e$, $m_h^* = 0.45 * m_h$ for CdSe core and $m_e^* = 0.2 * m_e$, $m_h^* = 0.7 * m_h$ for CdS shell), $\hbar$ is the reduced Plank constant, V_{cb} and V_{vb} are the potential of the conduction and valence band, respectively, q_e and q_h are charges of electron and hole. ε_o is vacuum permittivity, ε is relative permittivity and E_e and E_h are the energy eigenvalues of the electron and the hole, respectively. The charge distributions of the electron (ρ_e) and the hole (ρ_h) are calculated by the equations:

$$\rho_e = q_e\frac{\psi_e^2}{\langle\psi_e|\psi_e\rangle} \tag{4.5}$$

$$\rho_h = q_e\frac{\psi_h^2}{\langle\psi_h|\psi_h\rangle} \tag{4.6}$$

These calculations have been done in collaboration with Dr. Chunyong Li. The conduction and valence band offsets, between CdSe core and CdS shell, are assumed to be equal to -0.06 eV and 0.78 eV, respectively and $E_g = 1.67$ is the bandgap of CdSe at room temperature. Following the same equations, we also estimate the wavefunctions and energy eigenvalues of two excited electron-hole pairs (biexcitons), while the electric potential generated by all other carriers is also included into the Schrödinger equation.

The energy eigenvalues $E_e = 0.151$ eV and $E_h = 0.140$ eV of the electron and the hole, respectively, results to single exciton energy $E_X = E_e + E_h + E_g = 0.152 + 0.140 + 1.68 = 1.972$ eV. Radiative recombinations of the single excitons produce photons at $\lambda = \frac{hc}{E} = 629$ nm, a value very close to single mode laser emission (628.32 nm) shown in Figure 4.6. Therefore, the

theoretical calculations give strong evidence that the laser emission observed is originated by the stimulated emission of single exciton.

The energy eigenvalues of the two excited electron-hole pairs (biexciton) was also estimated to be $E_{e1} = 0.149$ eV, $E_{h1} = 0.199$ eV, $E_{e2} = 0.155$ eV and $E_{h2} = 0.199$ eV where E_{e1}, E_{h1} are the energy eigenvalues of the first excited electron and hole pair and E_{e2}, E_{h2} are the energy eigenvalues of the second one. Figure 4.9 illustrates the spatial separation of the electron and hole wavefunctions for the single exciton and biexciton. We observe that the repulsive Coulomb interaction between the two excited electrons separates their wavefunctions, localizing the wavefunction of the first excited electron in the CdSe core and the wavefunction of the second excited electron in the CdS shell and leading to different exciton energies. The Coulomb interaction between the two generated excitons results in a transient Stark shift that leads to an exciton/biexciton energy difference of $\Delta_{XX} = E_{XX} - 2E_X$ where E_{XX} and E_X are the biexciton and single exciton energies, respectively. The Stark shift is then calculated to be $\Delta_{XX} = 0.702 - 2 * 0.292 = 0.118$ eV where the biexciton energy is equal to $E_{XX} = E_{e1} + E_{h1} + E_{e2} + E_{h2} = 0.702$ eV. Photons produced by the biexciton radiative recombinations are spectrally shifted with respect to the photons from the single exciton recombinations and their emission wavelength is calculated to be 593.217 nm. This result identifies that the laser emission at 592.5 nm shown in Figure 4.7, corresponds to $1S_e$-$1S_h$ biexciton transitions while the laser emission at 585.76 nm is a high order mode within the biexciton gain bandwidth. The spacing between these lines with adjacent *l* indices was 6.74-nm at λ_L~592.5 nm, and corresponds to the free spectral range (FSR) $\Delta\lambda_{FSR} = 6.75$ nm of the hybrid resonator, which is approximately given by the equation (2.30).

Larger microspheres produced multimode laser emission due to the smaller free spectral range ($\Delta\lambda_{FSR}$) which corresponds to smaller separation distance between the modes with different azimuthal numbers. Figure 4.10 shows a laser emission spectrum obtained from a microsphere with a diameter of 29.4 μm by pumping at the equatorial zone. A number of lasing modes appear in the spectrum, at wavelengths separated by a distance of 2.4 nm, which is very close to the $\Delta\lambda_{FSR}$=2.375 nm that can be derived from the equation (2.30) for a coated sphere with this specific radius and laser-emission at a wavelength λ_L = 628.3 nm. These laser-emission peaks

correspond to the stimulated emission from single electron-hole pair excitation, according to the previous calculations.

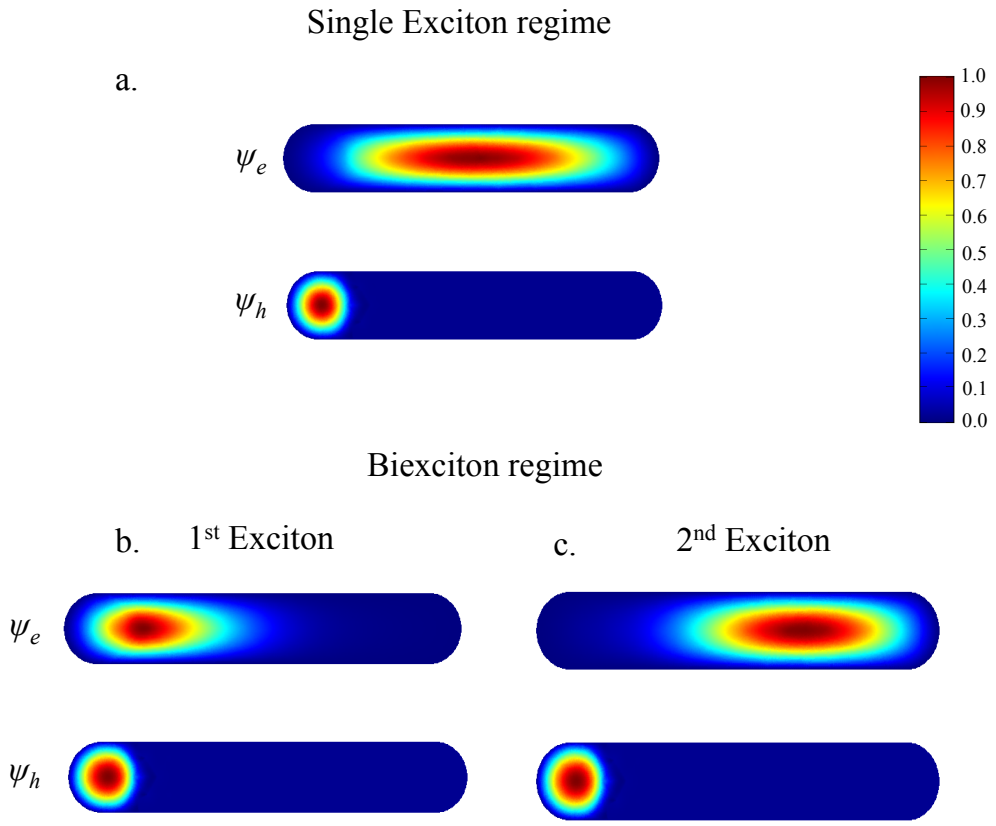

Figure 4.9: a) Wavefunctions of the lower energy electron-hole pair for a single exciton. The electric field induced between two excitons separates the wavefunctions of the two excited electrons, (b) localizing the wavefunction of the first excited electron in CdSe core and (c) the wavefucntion of the second electron in CdS shell. The hole in all the cases is localized into the CdSe core.

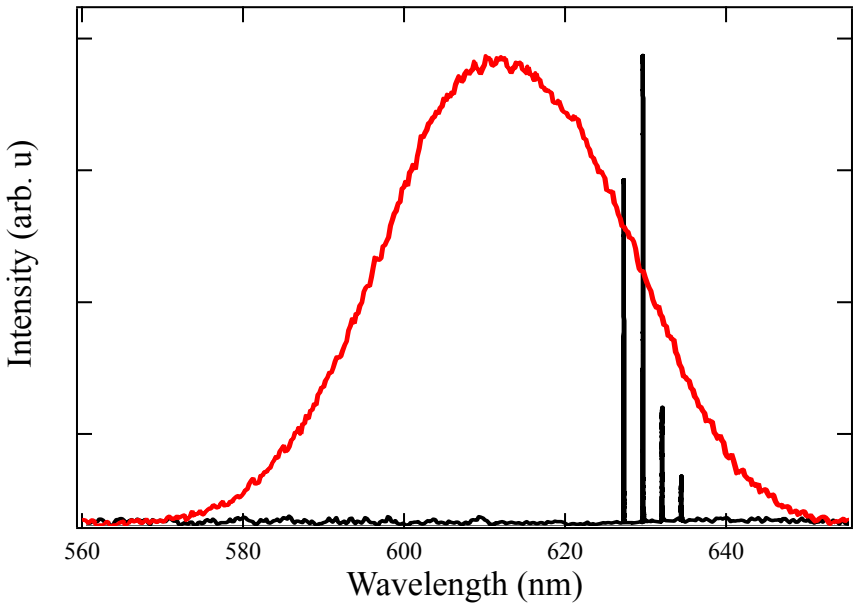

Figure 4.10. Multimode laser spectrum, with laser lines at 628.3 nm, 630.7 nm, 633.1 nm and 635.5 nm, obtained from a microsphere with a diameter of 29.4 μm. The equally spaced laser modes correspond to the free-spectral range of the microsphere.

4.3 Tunable single-mode laser emission from CdSe/CdS core/shell QRs

Laser-emission can be tuned by applying pressure or strain [112,113], using heating sources [114] or modulating the pump power [113]. The application of strain to a silica microsphere deforms the cavity, changes the refractive index of the glass and thereby tunes the resonant frequencies of the cavity modes [113]. Heating the microsphere is another alternative method for tuning the resonance modes due to alterations of the refractive index and cavity size. Although the tuning ranges achieved by temperature variation are shorter compared to those obtained with the strain method, this approach can accurate control the tuning of the laser wavelength. An increase in pump power also results in a shift of the WGM laser emission wavelength, which is associated with the induced heating of the microsphere from the pump laser.

In this work the wavelength of the laser (λ_L) was continuously tuned by heating the 9.2 μm large hybrid microsphere with 3.5-μm femtosecond laser. The beam of the infrared laser was focused to the microsphere by a microscope objective with five times magnification. The power of the

laser pulses was raised in successive steps. For each step the wavelength of the pump laser was modulated in order to excite resonant WGMs that were gradually shifted in wavelength due to the temperature elevation. The laser spectrum was recorded for each pump power indicating a maximum red-shift of the wavelength of 2.1 nm within the available power range of 60 mW (Figure 4.11), which corresponds to 30 % of the FSR at laser-wavelength. According to the red-shift observed in the single mode laser, it is expected that pumping the microsphere away from the equatorial, the emission of the multimode laser will also red-shift gradually.

We examined if the tuning range obtained experimentally is consistent with the theoretical predicted value for a given temperature variation. So, first of all, the temperature variation induced by the laser irradiation needs to be determined. Then, the spectral shift is estimated through the variation of the refractive index, the size and the energy gap of the QRs and the size of the microsphere, for a given temperature change. The effect of these factors on the tuning range of the lasing wavelength is described by the following equation:

$$\Delta\lambda = \lambda * a_{nc} * \Delta T + \lambda * a_s * \Delta T + \lambda * \frac{1}{n_{nc}} * \frac{dn_{nc}}{dT} * \Delta T + \Delta\lambda_{bg} \quad (4.10)$$

where $a_s = 5.5 * 10^{-7}\text{K}^{-1}$ and $a_{nc} = 4.5 * 10^{-6}\text{K}^{-1}$ are the thermal expansion coefficient of silica microsphere and the CdSe/CdS QRs, respectively, $n_{nc} = 2.5$ is the effective refractive index of the QRs and $\frac{dn_{nc}}{dT} = 10^{-4}$ K^{-1} is the thermo-optic coefficient of the bulk CdS and ΔT is the variation of the temperature due to the irradiation with the laser at 3.5 μm. The first and second terms in the equation (4.10) correspond to the shift of the laser emission due to the size change of the QDs and the microsphere due to the altered temperature. The third factor is related to the thermo-optic coefficient and shows the change in the refractive index due to the heat conduction from the microsphere to the QRs coating. Finally, $\Delta\lambda_{bg}$ is the shift in the emission wavelength of the QRs due to the bandgap ΔE_g variation with the increase of the temperature. All the factors mentioned previously, shift the laser emission in the same direction.

At 3.5 μm (the wavelength of the laser irradiation), the silica microsphere absorbs 65 % of the total power intensity while the QRs are transparent. For this reason is expected that the QRs do not contribute to the increase of the temperature.

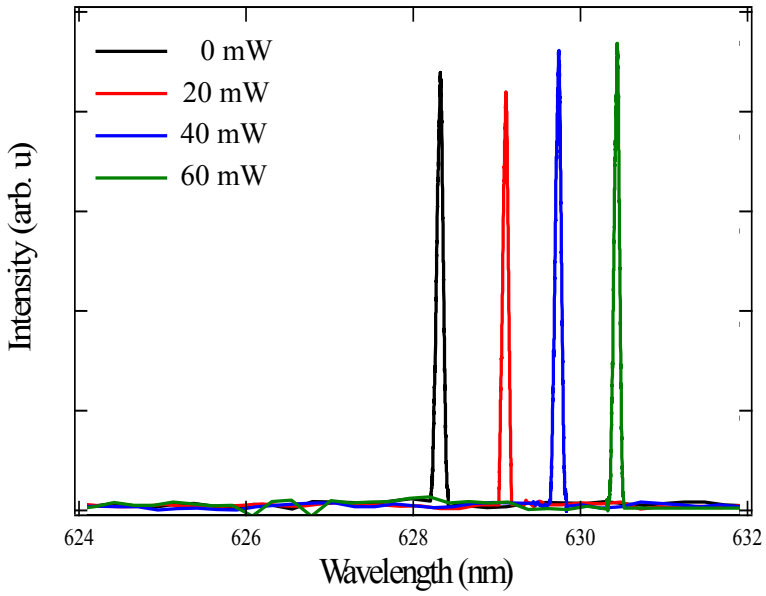

Figure 4.11: Laser emission lines obtained from a 9.2 µm large microsphere as recorded for different output powers of the 3.5 µm laser used for heating. The laser emission was tuned 2.5 nm for maximum irradiation power 60 mW.

The microsphere is therefore considered to be a single material (silica) which is heated by a focused laser beam in the presence of an ambient medium (in this case air). The air does not absorb at 3.5 µm and therefore it induces a decrease in the temperature of the microsphere. According to [115], the temperature rise in the microsphere as a result of the IR-laser illumination is given by:

$$\Delta T_c = \frac{P(1-R)}{2\sqrt{\pi}\omega_o \kappa_s}\left(1+\frac{\kappa_a}{\kappa_s}\right)^{-1} \quad (4.11)$$

where $\omega_o = R_s = 4.6\,nm$ is the radius of the illuminating laser beam which is approximated to be equal to the radius of the microsphere, κ_s=1.38x10^{-3} mW/mK^{-1} and κ_a = 2.6x10^{-2} mW/m·K^{-1} are the thermal conductivities of the silica glass and air, respectively. Also, *(1-R)* represents the absorption by the silica microsphere at the illumination wavelength with *R* corresponding to the Fresnel reflection at the air/QRs and QRs/silica interface and *P* to the illumination laser power which is absorbed by the microsphere. Since only 65 % of the input power is absorbed by the microsphere and 50 % loses are induced due to the Gaussian shape of the beam and the spherical

shape of the microsphere the power which contributes to the heating of the microsphere is given by:

$$P = 0.65 * 0.5 * 60 = 19.5 \text{ mW} \tag{4.12}$$

The Fresnel reflection in the interfaces between QRs/air and silica/QRs is calculated by the equation

$$R = (\frac{n_{QRs}-n_{air}}{n_{QRs}+n_{air}})^2 + (\frac{n_{QRs}-n_s}{n_{QRs}+n_s})^2 = 0.25 \tag{4.13}$$

where $n_{QRs} = 2.5, n_{air} = 1$ and $n_s = 1.47$ are the refractive indices of the QRs, the air and the sphere, respectively. Then, through equation (4.11) the change in the temperature is calculated to be 32.7 K.

The band gap of the QRs depends on the temperature according to the equation:

$$E_g(T) = E_g(0) - (\frac{a*T^2}{b+T}) \tag{4.14}$$

where $E_g(0)$ is the energy bandgap of the CdSe core at 0 K, b = 216 K and $a = 1.84 * 10^{-4}$ eV/K are constants for CdSe. Therefore, the energy bandgap difference (ΔE_g) for a 32.7 K temperature variation is given by:

$$\Delta E_g(T) = \left(\frac{a*(T+32.7)^2}{b+(T+32.7)}\right) - \left(\frac{a*T^2}{b+T}\right) = -0.005 \text{ eV} \tag{4.15}$$

where *T*=290 K. This energy variation corresponds to 1.579 nm red shift change calculated through the equation $\Delta\lambda_g = -\frac{{\lambda_g}^2}{h*C} = 1.579$ nm, where $\lambda_g = 628.32$ nm is the laser emission wavelength. Therefore, we can calculate from the equation (4.10) that the total shift in the laser-emission for 60 mW irradiation powers at 3.5 μm is 2.5 nm. The deviation between the theoretically predicted value (2.5 nm) and the experimentally observed wavelength tuning range (2.1 nm) can be attributed to various factors such as higher reflection levels than those was assumed or partial illumination of the microsphere by the IR beam. Furthermore, the different size of QRs could contribute to the laser emission by changing the size of the micro-resonator. Nevertheless, this parameter is very difficult to define experimentally or by calculations. In conclusion, the observed red-shift in the laser-emission due to the increased in temperature resulted from the thermal expansion of the sphere and QRs, the alter of the thermo-optic

coefficient, the change in the bandgap of the QRs and possibly the different sizes of QRs contribute to the laser emission.

4.4 Conclusions

In summary, operation of WGM lasers based on silica spheres coated with colloidal CdSe/CdS core/shell QRs was demonstrated by pumping through tapered fibers. Stable, single laser emission was achieved at room-temperature using microspheres with a diameter of less than 10 μm. Solving the Schrödinger equation by considering the effective mass approximation and Coulomb interaction, the laser emission was successfully matched to the single exciton regime. Simultaneous lasing from the biexciton $1S_h$–$1S_e$ state was observed by changing the coupling conditions in order to excite higher order modes away from the equatorial area of the microsphere or by increasing the in-coupled pump power. Multimode lasing from the single exciton regime was also observed for larger microspheres with a diameter of up to 40 μm. Tunable lasing within a wavelength range that includes approximately 30% of the FSR of the microsphere was achieved by using irradiation from an ultrashort pulsed laser source at 3.5 μm (80 MHz, 180 fs). The simplicity of the wet-chemical synthesis process of the QRs in combination with the high-Q factors of the spherical resonators makes the hybrid fiber-coupled system an excellent candidate for the study of the lasing properties of novel gain media.

Chapter 5: Ferroelectric substrates for neuro-photonics

Neuroscience is the study of the nervous system and links molecular processes with cell functions and human behaviour [116]. In order for the molecular and cellular behaviour to be explored, non-invasive techniques are needed that can produce both high resolution in space and time. Magnetic resonance imaging [117] and positron emission tomography [118,119] provide fairly good spatial resolution, but low temporal resolution. Other techniques for studying the electrical activity of neuron are electrophysiology [77] and voltage-sensitive fluorescent dyes [71-74]. Electrophysiology provides high temporal resolution, but is limited in spatial resolution since the required electrodes cannot be less than few hundreds nanometers [77]. On the other hand, membrane potential fluorescent dyes offer high spatial and time resolution, but their toxicity does not allow them to be used for consistent long-term studies [120]. The limitations of the current techniques reveal the need for the development of novel non-invasive tools for studying neuroscience.

As was mentioned in Chapter 1, other requirements for studying neuronal activity are the biocompatibility of the probes/electrodes, the controlled stimulation of the neurons, and the patterning of the neurons for the fundamental study of neuronal behaviour. Functionalized QDs could be used as a probe for imaging expression of proteins and recording the electrical activity of neurons. QDs can be functionalized with specific biomolecules, such as proteins or peptides, and selectively bind on neurons membrane. The expression of proteins can then be defined by recording the emission of the attached QDs. In addition, functionalized QDs with different ligands can spontaneously image multiple processes of neuron [121].

QRs have also the potential to work as nanoprobe for investigating cellular electrical signals due to their optical properties which are sensitive to the creation of local electric fields. Previous studies have shown that the PL spectrum of core/shell QDs shifts under the application of electric field [85,86].

When an external electric field is applied parallel to the length of the QDs, the wavefunctions of electron and the hole can spatially separate. The spatial separation of the electron and hole wavefunction is enhanced for the elongated Type II QRs heterostructure, such as CdSe/CdS QRs, where the hole is confined inside the core material (CdSe) while the electron can penetrate

into the elongated shell material (CdS). The application of an external electric field manipulates the distribution of the electron wavefunction in the core or shell material. Consequently, the Coulombic interaction between the electron and the hole is altered. Once an external electric field separates the wavefunctions of an electron and a hole in opposite direction, the decrease of the Coulombic interaction leads to lower emission wavelengths. The Coulombic electron-hole interaction is incorporated into the following equations by an effective potential $V_{e,h}$:

$$\left(\frac{\hbar^2\pi^2}{2m_e^*(\vec{r})}\Delta + V_{cb}(\vec{r}) + V_h(\vec{r}) + V_{ext}(\vec{r})\right)\Phi_e(\vec{r}) = E_e\Phi_e(\vec{r}) \tag{5.1}$$

$$\left(\frac{\hbar^2\pi^2}{2m_h^*(\vec{r})}\Delta + V_{vb}(\vec{r}) + V_e(\vec{r}) - V_{ext}(\vec{r})\right)\Phi_h(\vec{r}) = E_h\Phi_h(\vec{r}) \tag{5.2}$$

where V_{vb} and V_{cb} are the valence and conduction band potentials, respectively, and V_{ext} indicates an external potential [86]. The first term in the two equations corresponds to the kinetic energy, the second represents the valence and conductive band energies and the third one constitutes the electron-hole interaction mediated through an effective potential.

Neurons are highly polarized cells where thousand of ions are transferred through their membrane in sub-millisecond time scale. The action potential produced across their 12 nm thick membrane is around 50 mV, which corresponds to 416 kV/cm [72,74,120]. Previous experimental studies have shown that this range of electric field can produce a 18 nm spectral shift in the emission of CdSe/CdS QRs [86]. Therefore, the imaging of the neuronal electrical activity can be recorded with nanometer resolution by using heterostructured CdSe/CdS QRs.

On the other hand, neurons can be cultured on a material which can allow their patterning, and the excitation of the optical nanoprobes. In this work, the transparent ferroelectric $LiNbO_3$ crystal is employed as a substrate. The junction between $LiNbO_3$ crystal and neuronal tissue, is particularly worthy of scientific attention for several reasons: (i) neuronal cells are electroactive, hence, the pyroelectric properties of the mentioned substrate can be used to electrically stimulate them, (ii) $LiNbO_3$ waveguides could be used for multi-excitation of different fluorophores on neuron surfaces and (iii) microstructured $LiNbO_3$ substrates have the potential to control neural interfacing through physical patterning. Physical patterning offers a potent means for the control of cell adhesion, migration, orientation, shape, while it is of high importance for fundamental neuronal studies [59].

In this chapter, the biocompatibility and the spatial selective attachment of neuron-like cells onto $LiNbO_3$ substrates are investigated. The use of QDs for interfacing neuron activity, requires the functionalization of the QDs with ligands which can bind to the cells. In addition, QDs are capped with ligands which gives them stability without aggregating in an environment, which is rich in salt and proteins such as the culture medium. Unfortunately, this type of functionalization is difficult to achieve. Furthermore, such functionalized water soluble QDs were not available when this work was conducted.

This chapter presents the findings regarding the proliferation and differentiation of pheochromocytoma (PC12) [122] and human neuroblastoma SH-SY5Y cell lines [123] on the polar surfaces of the crystal as well as the comparison with the commonly used collagen coated plastic substrates. The results suggest that both polar faces (±z) of $LiNbO_3$ crystals are excellent substrates for the growth of biological cells. In addition, it is shown that ferroelectric domain engineered and surface micro-structured $LiNbO_3$ substrates can be used as templates for the spatially selective growth of neuron-like cell lines and the development of neuronal networks.

5.1 Properties of $LiNbO_3$ Ferroelectric Crystal

Lithium niobate ($LiNbO_3$) is an artificial dielectric crystal that has one threefold axis of rotation defined as polar axis (c-axis) and along this axis a sequence of close-packed, face sharing, oxygen octahedral are stacked [124].

This material is of high technological interest due to its numerous properties (electro-optic, piezoelectric, acousto-optic, photo-refractive, pyro-electric, photovoltaic, ferroelectric and optical nonlinearity) [125]. Moreover, $LiNbO_3$ has been widely used for the production of integrated optical modulators [125], optical frequency converters [126] and surface acoustic wave transducers on a single substrate [127].

5.1.1. Ferroelectric property of $LiNbO_3$ crystal

As defined by Lines and Glass [128], ferroelectrics are substances which in certain range of temperatures and isotropic pressures, in the absence of external electric field have a spontaneous polarization, P_s, which can have two or more orientation states. The orientation states can be switched from one state to the other by an external electric field. Any of the orientation states are identical in their crystal structure and differ only in direction of the electric polarization vector. Regions with uniform polarization are called ferroelectric domains.

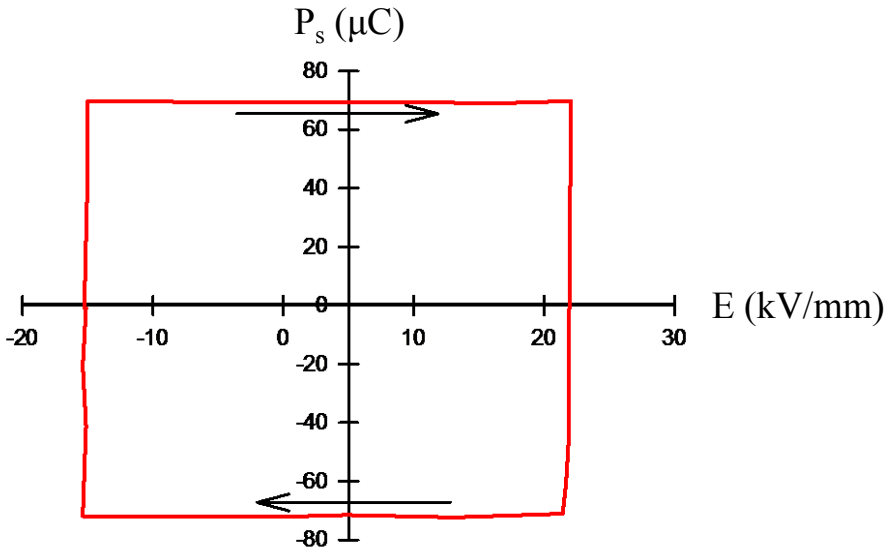

Figure 5.1: The hysteresis loop of $LiNbO_3$, single crystal at room temperature. An arrow indicates the magnitude and direction of the internal field. The two polarization states are labelled as state I and II [129]

Ferroelectricity is determined experimentally through the hysteresis loop. Ferroelectric hysteresis loop measures the average spontaneous polarization in a material as a function of the applied electric field. It initiates from the energy required to move the domain walls between domains of different polarization and then change the net polarization of the ferroelectric material by altering the size of the various domains [130].

$LiNbO_3$ is an optical ferroelectric crystal. Figure 5.1 illustrates the typical polarization hysteresis curve for 0.5 mm thick $LiNbO_3$ single crystal at room temperature [129]. It is observed that

applying a forward E_{cf} or reverse E_{cr} electric field the polarization can switch from $+P_s$ to $-P_s$, respectively. The crystal with reversed polarization is called "domain reversed crystal".

5.1.2 $LiNbO_3$ crystal structure upon domain inversion

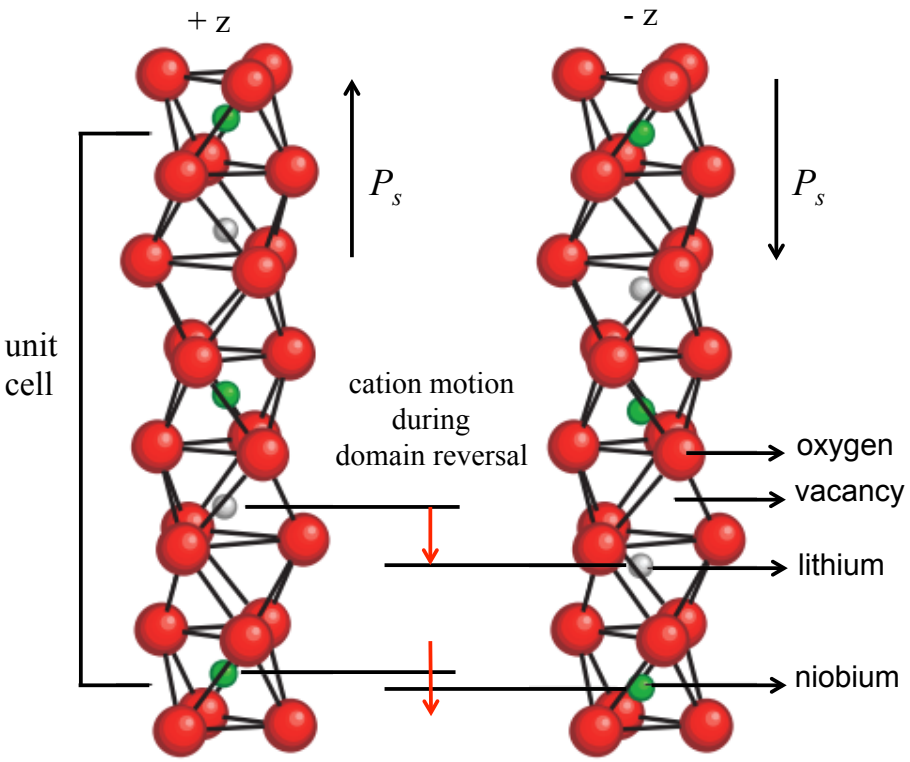

Figure 5.2: Cation motion during domain reversal redrawn from Gopalan *et al.* [129]

$LiNbO_3$ is also a ferroelectric material which has a Curie temperature at 1210 °C and a large (0.70 C/m^2) spontaneous polarization at room temperature. $LiNbO_3$ single crystals exhibit paraelectric phases above the Curie temperature and ferroelectric phases below the Curie temperature [131]. The existence of a dipole moment in $LiNbO_3$ material is emanated from the position of the metallic ions (Li^+ and Nb^{5+} ions) in the ferroelectric phase.

In order to invert the dipole moment of $LiNbO_3$ and consequently the direction of polarization, the metallic ions should undergo a transition within the oxygen lattice (Figure 5.2). As illustrated in Figure 5.2, the niobium ions (Nb^{5+}) undergo a small displacement from one asymmetric

position to the other equivalent position with respect to the centre of its octahedron along the z-axis, while lithium ions (Li^+) are transited from one octahedron, though the intermediate close-packed oxygen plane, to an equivalent displacement in the adjacent vacant octahedron [132]. The direction of these cations determines the direction of the spontaneous polarization, P_s. Therefore, two domain orientations can occur $\pm P_s$, because of the two permitted directions along z ($\pm z$).

5.2 Neurons

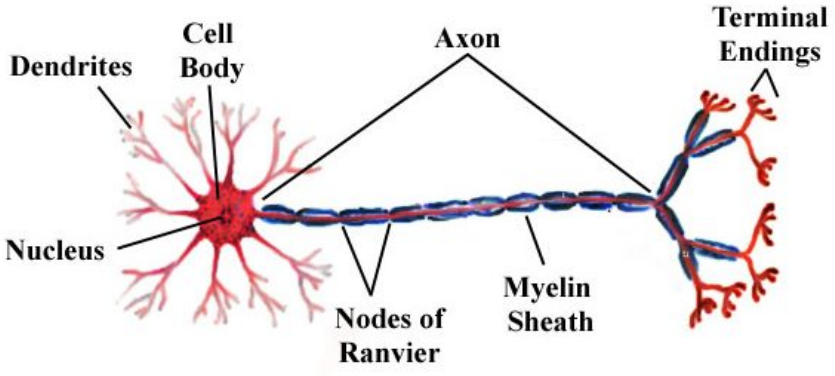

Figure 5.3: Structure of neurons

Neurons are cellular elements that underlie the function of the nervous system and response to an external stimulus by translating it into an electrical signal [133]. The brain mainly consists of a highly complex network of neurons that carry out and coordinate many of the human body's biological functions. Therefore, we can determine many aspects of the neural processes by studying the generation and propagation of electrical signals at the level of an individual cell up to a neuronal network [59,63,134,135].

Neurons consist of four distinct regions: the cell body (or soma), the dendrites, the axon and the axon terminal [59]. Figure 5.3 illustrates the structure of neurons with the four different regions. The cell body is the metabolic "control centre" of the neuron. The soma contains the nucleus and most of the genomic expression and synthetic machinery that elaborates the proteins, lipids, and

sugars that constitute the neuronal cytoplasm and membranes. The body diameter varies with the type of the cell, ranging from 5 to 120 μm. The extension of the cell body leads to an axon and dendrites [133].

Most of the neurons contain numerous, short and highly branched dendrites. Dendrites develop connections with other neurons and work as a gate for the incoming signals from other neurons. The diameter of the dendrites is around 1 μm and their length varies from 15 to 60 μm.

The axon is the third concrete region of neurons and has a diameter of between 1 and 15 μm while the length varies from a few hundreds of μm to 1 m. This region is extremely rich in microtubules and participates in the genesis of the electrical signal named "action potential". The axon could be considered as a tube filled with watery solution rich in salts and proteins. The intracellular solution is of the same ionic strength as the extracellular solution, but of different ionic composition. In a typical neuron, the axon is covered by a special insulating layer, the myelin sheath (200 and 800 μm thick), which is interrupted at regular intervals by gaps called the Nodes of Ranvier (1 μm wide). This insulating envelope of myelin facilitates the transmission of nerve impulses and increases the speed by which information travels along the nerve. Furthermore, various ion channels are positioned along the Nodes of Ranvier, which allow the influx or efflux of different type of ions into and out of the neuron. These channels are responsible for maintaining the physiological functioning of the neuron in terms of the membrane potential [136]. Information is transduced from one neuron to another from the nerve endings to the cell soma.

5.3 Material and Methods

5.1.1 $LiNbO_3$ samples

$LiNbO_3$ substrates with +z/-z polarities were purchased by Crystal Technology.

Micro-structured $LiNbO_3$ substrates were engineered via polar surface-specific chemical etching. A set of different etchants including a mixture of 30 % hydrogen peroxide (H_2O_2) and sodium

hydroxide (NaOH), hydrofluoric acid (HF) with potassium permanganate ($KMnO_4$) or potassium hydroxide (KOH), can be used to differentially etch $LiNbO_3$ [137]. The etching rates of the mentioned chemicals for the different polarities of the $LiNbO_3$ crystal can vary significant. It was reported that the etching rates were 0.8 μm/h for the –z face and 30 μm/h for +z face at room and temperature, for a mixture of nitric and HF acid [138]. The y-faces also exhibit a similar etch characteristic, with the –y face etching much faster than the +y face in HF [138].

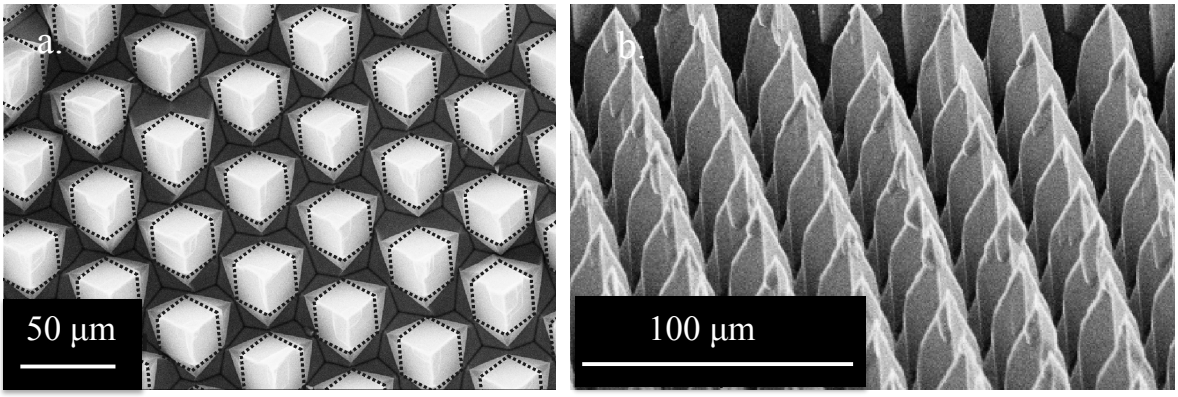

Figure 5.4: a) Top view SEM image of the micro-structured LiNbO3 substrate used in the cell growth experiments. The shape and position of the original inverted domains is indicated by the dotted hexagonal shapes. b) SEM side-view of the structures shown in (a)

In order to take advantage of the differentiated etching rates, different polarities pattern can be achieved on $LiNbO_3$ crystal by using intense pulsed UV irradiation at wavelength 248 nm [139,140]. Micro-structured substrates can then be prepared by differential etching (in HF acid) of a 2D periodic lattice of inverted hexagonal shaped domains. The combined action of the fast etching rate of HF acid of the –z face compared to the +z face and a slower sideways etching along the three symmetry y-directions of the crystal results in a 2D array of sharp tipped micro-pyramids [137] which can be observed in the SEM images shown in Figure 5.4. These pyramids are around 100 μm high and are 30 μm apart [141].

This complex etching process transforms the initially hexagonal shape of the individual domains into micro-pyramids with a triangular cross section as shown in Figure 5.4a. A SEM side view of the micro-pyramid array demonstrating the high aspect ratio and their sharp endpoints is shown

in Figure 5.4b. The dash-line hexagons, drawn onto the SEM image of Figure 5.4a, indicate an inverted ferroelectric distribution superimposed onto the topography of the surface [141].

5.3.2 Culture of neurons

All chemicals used in the processes described in this chapter were purchased from Sigma-Aldrich, and culture media and components were purchased from Invitrogen-Gibco.

Two different neuron-like cells, pheochromocytoma (PC12) [122] and human neuroblastoma SH-SY5Y cell line [123], were seeded onto $LiNbO_3$ substrates and onto collagen coated plastic culture plates with $1x10^6$ cells density.

The proliferation of PC12 cells was achieved by using a culture medium which contains RPMI 1640 medium completed with 7% horse serum, 7% foetal calf serum, 2 mM of L-Glutamine, 10 mM of HEPES, 4.5 g/l of D-Glucose. The substrates were placed in a 6-well plate composed of two wells with $LiNbO_3$ –z oriented $LiNbO_3$ substrates, two wells with +z oriented $LiNbO_3$ substrates, and two wells with collagen IV coating. Cells were allowed to attach for one week before the start of the cellular proliferation assay.

After 24 hours of seeding, nerve growth factor (NGF-50 ng/ml) was added in a culture medium of 6 % foetal calf serum concentration, in order to induce neurite formation.

The SH-SY5Y cell line was grown in Dulbecco's Modified Eagle's Medium (DMEM) supplemented with 2 mM of L-glutamine, penicillin (20 unit/ml), streptomycin (20 mgr/ml), and 15% heat-inactivated foetal calf serum (GIBCO). Cells were maintained at 37 ^oC in a saturated humidity atmosphere containing 95% air and 5% CO_2. Cells were seeded at an initial density of 10^4 cells/cm^2. Retinoic Acid (RA) was added at a concentration of 10 μM in DMEM with 15% foetal serum for 7 days in order to induce cells differentiation and neuronal development. The addition of RA started the day after the beginning of cell culture. In the presence of RA, cells were then washed three times with DMEM and incubated with 50 ng/mL of Brain-Derived Neurotrophic Factor (BDNF) in DMEM for 3 days.

5.4 Results and Discussion

5.4.1 Biocompatibility of neurons on $LiNbO_3$ substrate

The biocompatibility of neurons on the +z/-z polar surfaces of $LiNbO_3$ substrates was evaluated by four independent experiments. Neuron cells were cultured onto three different substrates: +z-face, -z face of $LiNbO_3$ crystal and collagen treated plastic control substrate. Cellular proliferation and viability were measured using the Resazurin Assay (Alamar Blue) [142]. This assay measures the reduction of resazurin (non-fluorescent molecule) by cells to resorufin (fluorescent molecule-emission at 590 nm) using a flexible multi-detection microplate reader (FLUOstar OPTIMA, BMG Labtech, Offenburg, Germany). The excitation wavelength was fixed at 530 nm. The water-soluble resazurin assay was performed in Hanks' Balanced Salt Solution with 10 mg/ml resazurin mixed with the culture medium at a 10 % final concentration. The solution was heated to 37 °C prior to use and added to the cultures one hour after seeding to allow the attachment of the cells. After the addition of resazurin the cells were incubated at 37 °C/ 5% CO_2.

Cells were seeded onto $LiNbO_3$ substrates, which had been placed in 6-well plates. The irregular shape of the substrates was not a perfect fit with the culture plate wells; therefore, it was not possible to place the plate inside the plate reader directly due to potential reflection of the laser through the substrates. Thus, the medium was removed from the wells and placed in a 96-well plate at 4 and 24 hours intervals, and was then assayed using the plate reader. Wells containing no cells were also measured to give the background signal to the well itself and these values were subtracted prior to further calculations.

Figure 5.5 illustrates the mean values of the resazurin absorption from four independent experiments for three different substrates. The absorption value of the resazurin for the +z and -z polar surface was similar indicating that the cellular proliferation was not influenced by the polarity of the crystal. The number of cells grown on the +z and -z polar surface of $LiNbO_3$ substrates was close to the number of cells grown on the plastic control-substrate.

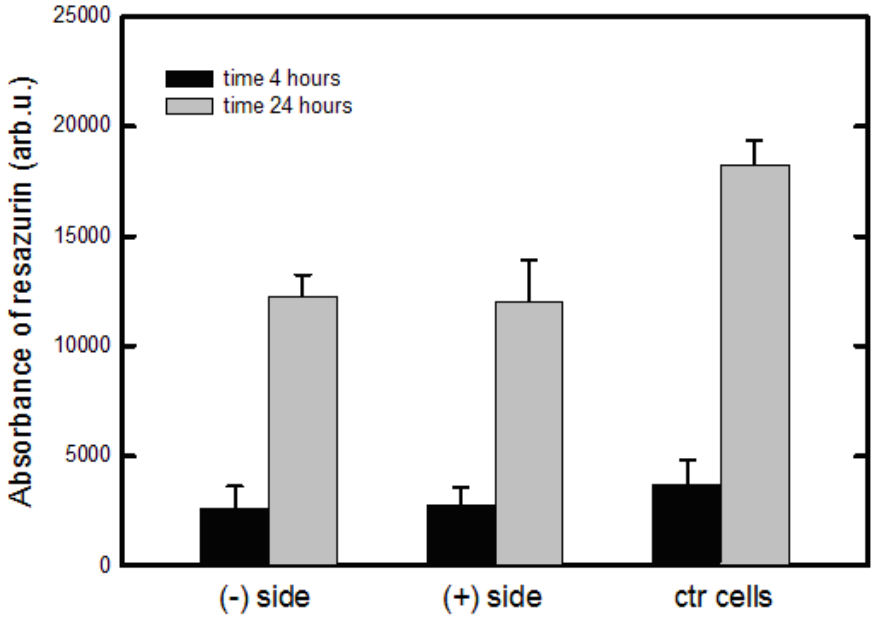

Figure 5.5: Cellular proliferation of cultured PC12 cells on the –z and +z polar surfaces of $LiNbO_3$ crystal substrates are compared to control cells cultured onto collagen IV coated petri dish (control cells) at 4 hours and 24 hours intervals after seeding. The histogram shows average data from 4 independent experiments

Statistical analysis on the presented data in Figure 5.5 was also carried out using t-test in order to compare the mean values from six independent groups: (G1) cells grown on -z face of $LiNbO_3$ substrate after 4h, (G2) cells grown on +z face of $LiNbO_3$ substrate after 4h, (G3) cells grown on collagen treated substrate after 4h, (G4) cells grown on -z face of $LiNbO_3$ substrate after 24h, (G5) cells grown on +z face of $LiNbO_3$ substrate after 24h, (G6) cells grown on collagen treated substrate for 24h. T-tests were used to compare the means of two independently sampled groups. The t-value was calculated in the equation

$$t = \frac{(\bar{x}_1 - \bar{x}_2)}{\sqrt{\frac{\sigma_1^2 + \sigma_2^2}{N^2}}} \quad (5.1),$$

where $\bar{x}_1$, $\bar{x}_2$ are the mean values of the two comparison groups, σ_1, σ_2 are their standard deviation and N is the degree of freedom. We make the hypothesis that the variation between the group values is zero for $p>0.05$ while for $p<0.05$ we can conclude that the groups have a significant difference in their means. The p-value shows the probability of obtaining a value of a test statistic greater or equal as the one that was observed, assuming that the initial hypothesis is true.

The comparison of the groups (G1) and (G2) showed that there is no statistical difference between their mean values as the p-value (p_{G1-G2}=0.82) was larger than 0.05 supporting the beginning hypothesis. After the comparison of the (G1) and (G2) group with the (G3) group, we were led to the same conclusion (p_{G1-G3}=0.20, p_{G2-G2}=0.23). The qualitative analysis, thus, showed that there was no statistical difference between the number of cells grown on the different faces of $LiNbO_3$ substrates with that on collagen treated controlled substrates after 4 hours (p_{G4-G5}=0.814>0.05).

The comparison between the groups (G4) and (G5) also support the results from the comparison of the groups (G1) and (G2), indicating that there is no difference on the number of cells grown between the different ±z faces of $LiNbO_3$ substrates. Nevertheless, the comparison between the (G4) and (G5) with the (G6) group showed a statistical significant difference between their values with p<0.05 (p_{G4-G6}=0.005, p_{G5-G6}=0.009). The latter results indicate that the number of cells grown on the different faces of $LiNbO_3$ substrates was smaller than the number of cells grown on collagen treated substrate after 24 hours.

Cellular differentiation on both polar surfaces (+z/-z) of $LiNbO_3$ and the collagen IV coated plastic control substrate was initiated 24 hours after seeding using NGF. The extent of differentiation was assessed by measuring the length of multiple individual neurites from a minimum of 10 cells per well/experimental condition/time point. Representative images of the differentiated PC12 cells on $LiNbO_3$ after 10 and 20 days of culture are shown in Figure 5.6.

As shown in Figure 5.6, neurons differentiate successfully on the both +z/-z polar surfaces of the $LiNbO_3$ substrates. It can be observed that their neuronal processes have been developed in all the substrates. The lengths of the multiple individual neurites from the three different substrates indicate that the differentiation process was not interrupted by the presence of the $LiNbO_3$ substrate. The only observed difference between the neuron cells cultured on $LiNbO_3$ and plastic substrate is their initial number.

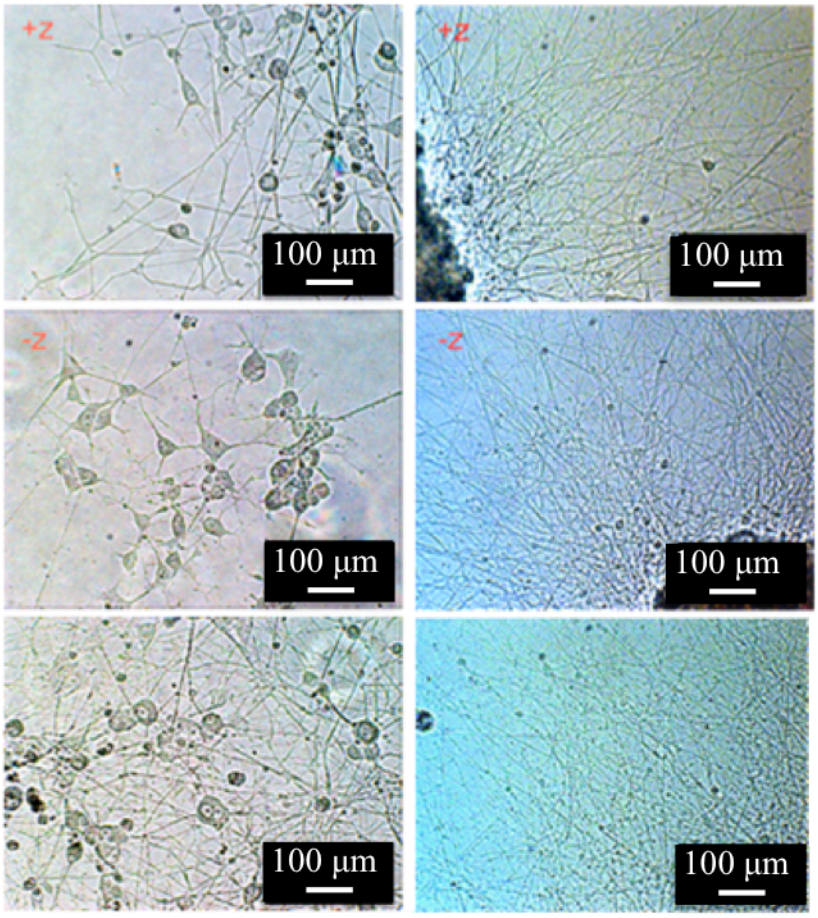

Figure 5.6: Differentiation of PC12 cells, following stimulation with NGF 24 hours after seeding, at 10 (left column) and 20 days (right column). The cells were grown on different substrates (+z top row, -z middle row and collagen coated plastic-bottom row) as indicated in the images.

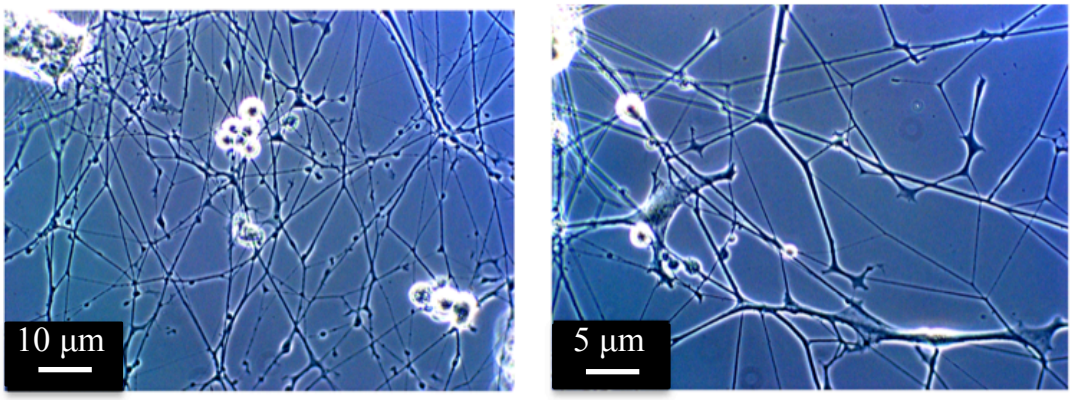

Figure 5.7: Differentiated PC12 cells on +z $LiNbO_3$ substrate

Also, the morphology of the differentiated neurons, the smoothness of the cell bodies and the multiple developed neuronal processes of axons and dendrites, indicate the health of these cells. Figure 5.7 illustrates the neuronal network of the differentiated PC12 cells on the $LiNbO_3$ substrates. The successful differentiation of neuron and the development of their processes rely on good cell adherence to the substrate. The results suggest that cell adhesion is sufficient to merit further neurobiological studies using $LiNbO_3$ and proves the compatibility of neuron cells with both polarizations of LiNbO3 substrate.

To confirm these results, SH-SY5Y cells, were also cultured on the +z $LiNbO_3$ substrate. SH-SY5Y cells are widely used for in vitro studies of neuronal processes. The proliferation and differentiation of the SH-SY5Y cell line on +z $LiNbO_3$ was comparable with the results from the PC12 cells and also verify the biocompatibility of this ferroelectric crystal (Figure 5.8). This cell line exhibits a much slower electrical signal transmission response, which makes them attractive for the investigation of electrical signals through cellular neural networks.

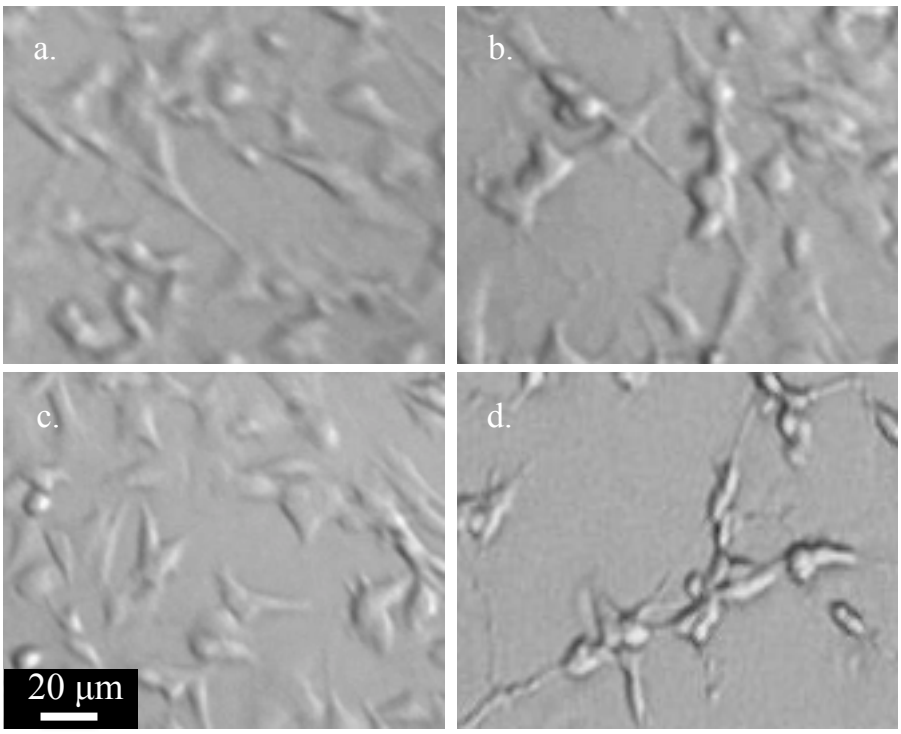

Figure 5.8: Culture of SH-SY5Y neuroblastoma cell line on (a, b) $LiNbO_3$ and plastic substrate (c-d)

The spontaneous polarization of polar materials, such as $LiNbO_3$, induces macroscopic polarization charges at the surface [124]. The presence of these microscopic dipoles at the polar surface can be cancelled by the introduction of compensating charges by the ambient environment (Figure 5.9). The surface absorption of charged molecules from the environment (external screening) can modify the electronic structure of the surface and give rise to variations in the surface electron affinity [143].

During the cell culture the crystal substrates are immersed in an electrolyte (culture media solution) and therefore the bound charges must be fully compensated. The two opposite polar surfaces, however, will be compensated by different ions/radicals consequently changing their chemical response accordingly [144]. The experimental results on the proliferation and differentiation of PC12 and SH-SY5Y cell lines prove that cell adhesion occurred on both polar surfaces. The latter can be interpreted in two different ways: i) the proliferation is independent of the surface polarity/type of compensated charges or ii) opposite charged parts of the cell (i.e. cell body, cell processes), or variable expression of molecules, e.g. adhesion molecules result in the attachment on different polar surfaces. The latter interpretation provides the most possible explanation for the results on the spatially selective attachment of cells onto micro-structured, domain engineered $LiNbO_3$ substrates, which is presented below.

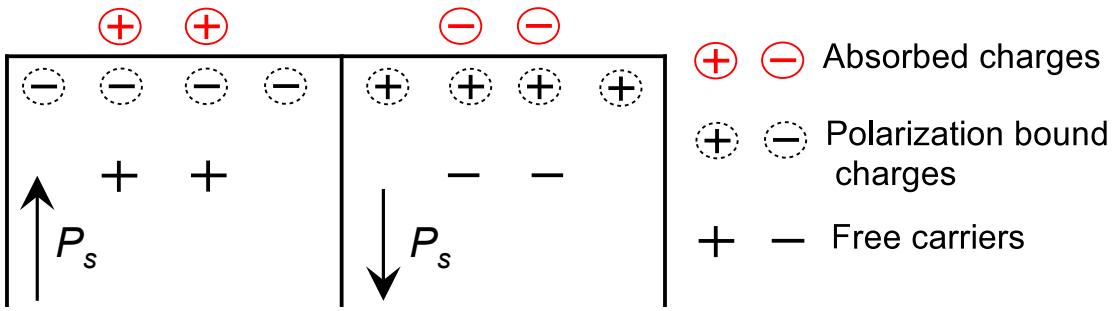

Figure 5.9: A schematic diagram of surface charges of polar materials redrawn from Yang W.C *et al.* [143]

5.4.2 Patterning of neurons on microstructured $LiNbO_3$ substrate

Having established the biocompatibility of $LiNbO_3$ surfaces with the proliferation and differentiation processes of the two most commonly used neuron-like model systems we set out to investigate the impact of the surface topography of domain engineered $LiNbO_3$ substrates on cell viability. The expansion beyond planar topography for cellular assays is of particular interest in order to control the positioning of the cellular distribution and provide a scaffold or template for the development of a model neural network.

PC12 and SH-SY5Y cells were seeded onto micro-structured domain engineered substrates and their distribution was investigated. The patterned structures were pyramids, about 100 μm high (Figure 5.4).

Neuron-like cells were cultured as it was described in section 5.3 and labelled with the cell membrane dye, CellTracker Green CMFDA (5-chloromethylfluorescein diacetate, Invitrogen). The cells were then excited at 490 nm and imaged with a fluorescent microscope. As shown in Figure 5.10, the PC12 and SH-SY5Y cells attach selectively in the vicinity of the apex of the micro-pyramids, while no cells can be found in the adjacent cervices. This observation was consistent throughout the surface of the micro-structured substrate. The images in Figure 5.10 correspond to different, randomly chosen, areas of the substrates cultured with PC12 (a-d) and SH-SY5Y cells (e-f).

Surface topography of substrates is known to alter cell adhesion and growth [145,146]. Alterations in the periodicity and aspect ratio of surfaces at the micron level have been shown to alter expression of cytoskeletal proteins, in both the soma and processes of cells [146]. Microstructured $LiNbO_3$ substrate confers control of growth through both topography and inherent variation in the domains within the 3D structure.

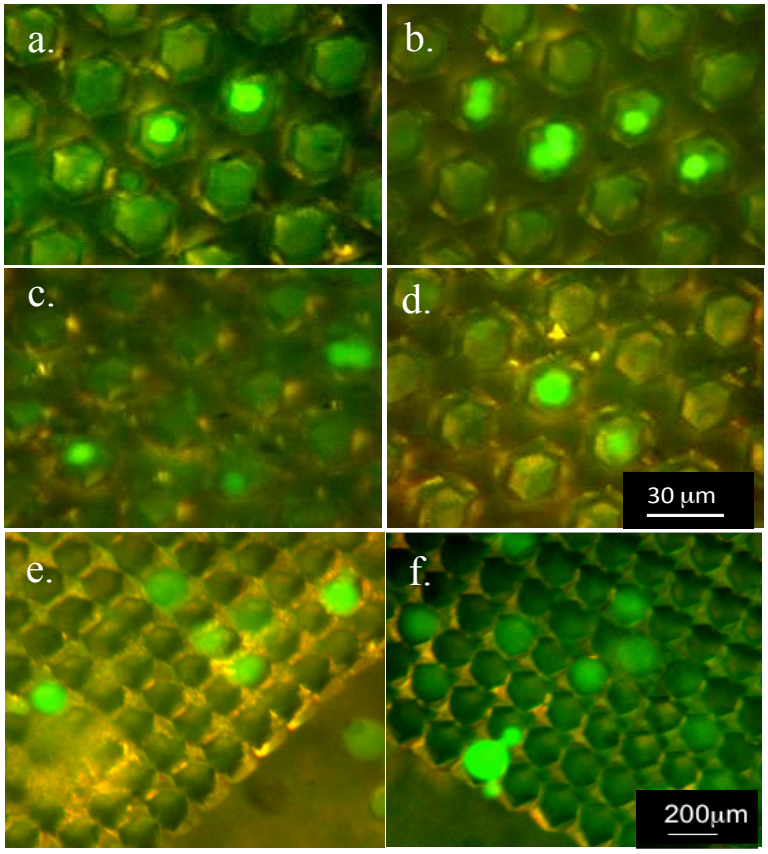

Figure 5.10: Optical microscopy images of fluorescent PC12 cells grown only on the tips of the $LiNbO_3$ micro-pyramids (a-d). Figures (a-d) have the same scale; Images of SH-SY5Y cells grown on the tips of the LiNbO3 micro-pyramids (e, f) and have the same scale

The selective attachment of the PC12 cells on the tips of the $LiNbO_3$ micro-pyramids is explained by the distribution of the bound charges on this structure. The superposition of the inverted domain distribution on the structured surface is associated with an uneven distribution of the bound charges on the crystal surface, which is given by: $\sigma=n*P$, where P is the spontaneous polarization (0.72 μC/mm^2) and n the surface normal unit vector. Unlike the bound surface charge could not be measured using electric force microscopy due to the extreme surface topography [147]. However, the localized electrostatic field on the tip of micropyramids attracts opposite charge molecules or areas of the cells resulting in the good affinity between the body of the cell and the microstructure. These findings suggests that this microstructure substrate could be successfully used for patterning neuron-like cells while their separation distance can be tuned by altering the distance between the micropyramids. Furthermore, the conclusions of this study,

open the way for further investigations on patterning neurons with other ferroelectric microstructured substrates, where the charge distribution can be controlled.

5.5 Conclusions

The biocompatibility of the domain engineered and micro-structured $LiNbO_3$ substrates, was investigated in this chapter. Two different neuron-like cell lines were used in order to study the proliferation and differentiation on the two different faces of $LiNbO_3$ substrate. It was observed that the number of cells on $LiNbO_3$ substrate was just slightly less than the ones grown on collagen treated plastic. However, it was demonstrated that the neuron-like cells can develop successfully their processes without any discrimination between the $LiNbO_3$ and the plastic substrate. The aforementioned results prove the biocompatibility of $LiNbO_3$ crystal with these neuron-like cell lines increasing the use of this ferroelectric material for further studies in the neuroscience area.

The biocompatibility of micro-structured domain engineered substrates with neuron-like cells was also studied. The experimental results showed that the cells specifically attach on the tip of the micropyramids. These results can set up the basis for the use of microstructure engineered $LiNbO_3$ substrates for patterning neuron cells and control their spatial distribution in order to develop of controlled neural networks. Our results show, that photonic circuits can now be effectively integrated into the biological environment in order to enable novel approaches, optical stimulation and sense molecular pathways within cells and cellular networks in real time.

Chapter 6: Conclusions

The integration of different types of materials into a hybrid structure provides a tool for the development of novel photonic devices. In the first part of this thesis, the exciton dynamics in oleic acid capped PbS QDs with diameters from 2.3 nm to 3.5 nm was studied. Non-monotonous temperature dependent carriers behaviour in PbS QDs was demonstrated and divided in three different temperature regimes. In the low temperature regime (temperatures from 6 K to 175 K), the PL decay rate was increased and the PL maximum was decreased as the temperature increased. In the second intermediate regime, (175-250 K) the PL decay rate decreased and the PL maximum increased while the reverse trend was observed in the last high temperature regime, (250-290 K) with the increase of temperature. This complex dynamics was explained by a model that considers the fine exciton splitting of PbS QDs and a trap state. A global fit to the measured size dependent PL dynamics converges to a lowest exciton splitting of 3 meV for most of the particles, while it decreased to 2 meV for the 3.5 nm diameter particles. An oscillator strength transfer from dark to bright state as the diameter of the particles increases was also observed.

RET from PbS QDs to silicon substrates was also studied by measuring the PL lifetime of PbS particles deposited on silicon, capped by an oxide spacing layer. RET mechanism occurred from PbS QDs to silicon for separation distances below 12nm. For a spacer thickness greater than 12 nm, no RET was observed and the PL decay of the QDs was equal to the value measured in absence of a silicon absorber, on a glass substrate. The RET rate and efficiency was found to exhibit a weak temperature dependence.

The findings suggest that PbS QDs can work as solar absorbers and can efficiently generate excitons to silicon. Nonetheless, in order to prove this concept which can be of benefit to the current photovoltaics industry, electrical measurements are also required. Photocurrent measurements should be performed on hybrid PbS coated silicon device and planar silicon device (without PbS QDs).

In the second part of this thesis, the use of heterostructured CdSe/CdS QRs as gain medium for laser applications was studied. The dimensions of the QRs were estimated to be around 4.1 nm width and 20 nm length and their emission maxima occurred at 616 nm. Silica microspheres

were coated with CdSe/CdS QRs and excited by pumping through tapered fibers. Single laser emission at 628.32 nm was observed at room temperature from microspheres with diameter around 9 nm. By changing the coupling conditions between the tapered fiber and the microsphere or increasing the in-coupled pump power, higher order modes were excited resulting to a multimode laser performance, with laser-emissions at 628.32 nm, 592.5 nm and 585.76 nm. In order to explain the observed laser-emission, the Schrödinger equation was solved and the energy eigenvalues for single and double excited electron-hole pairs were calculated. The theoretical calculations suggest that the single mode laser-emission is due to the stimulated emission from single excited electron-hole pair while the second set of laser emission is due to the stimulated emission of double excited electron-hole pair.

Tunability of the laser-emission was also achieved by heating the microsphere cavity with a laser at 3.5 μm. Considering that silica absorbs 65 % of the total power intensity at the given wavelength, the irradiation of the cavity with infrared laser altered the temperature of the silica microsphere. This rise in temperature changed the refractive index, the size and the energy gap of the QRs and the size of the microsphere and consequently tuned 2.5 nm the laser-emission for 60 mW irradiation powers.

In the last part of this thesis, the biocompatibility of the domain engineered $LiNbO_3$ substrates was investigated. Cellular proliferation of PC12 cells were conducted on –z and +z polar surfaces of $LiNbO_3$ crystal were compared to those cultured onto collagen-coated petri dish. These findings indicates that both polar surfaces of ferroelectric $LiNbO_3$ crystals can be excellent substrates for the proliferation and differentiation of the commonly used neuron-like cell lines, PC12 and SH-SY5Y neuroblastoma cells. Neuron-like cells were also cultured on micro-structured $LiNbO_3$ pyramids and selective attachment of the cells was observed. The latter results were attributed to the distribution of the bound charges on the tip of the micropyramids, which attract the cell body and result in the pattering of the cells. Photonic circuits can now be effectively integrated into the biological environment to enable novel approaches to real time optical stimulation and sensing of molecular pathways within cells and cellular networks.

The recording of different molecules behaviour in real time could give information for specific processes of neuron cells such as protein expressions, ion traffic, chemical or electrical responses of the neuronal transmitter. Different excitation wavelengths in the visible can be coupled in $LiNbO_3$ waveguides. The evanescent field created on the surface of $LiNbO_3$ can excite the different labelled molecules and their fluorescence can be detected with the use of a conventional fluorescent microscope. However more advanced optical techniques such as scanning near field microscopy will provide time and spatial information for specific areas of a neuronal network, such as the synaptic cleft.

As it was mentioned earlier, $LiNbO_3$ crystal provides an excellent route for surface micro-structuring. We demonstrated the selective patterning of neurons on sharp-tipped micro-pyramids. However, different structures of $LiNbO_3$ domain could also be studied for the development of different neuronal networks. The use of rectangular patterned areas, with width regions from 50 μm to 300 μm, is suggested. These regions can be used for elongated patterning of neurons. Then, the excitation of these patterned networks of neurons could be achieved via evanescent field.

The stimulation of these elongated structured neuron cells, while their electrical activity is monitored in real time, will expand our knowledge for the inter-neuron communications. The inter-neuron communication is highly important for the study of brain and neuromuscular diseases. The stimulation of neuron could be achieved by varying the temperature of $LiNbO_3$ locally, as the changes in the temperature can produce a voltage difference on $LiNbO_3$ surface leading to neuron stimulation.

Bibliography

[1] V. I. Klimov, "Spectral and dynamical properties of multiexcitons in semiconductor nanocrystals," *Annu. Rev. Phys. Chem.* **58**(1), 635–673 (2007) [doi:10.1146/annurev.physchem.58.032806.104537].

[2] D. V. Talapin, J. H. Nelson, E. V. Shevchenko, S. Aloni, B. Sadtler, and A. P. Alivisatos, "Seeded growth of highly luminescent CdSe/CdS nanoheterostructures with Rod and Tetrapod Morphologies," *Nano Lett.* **7**(10), 2951–2959 (2007) [doi:10.1021/nl072003g].

[3] L. Carbone, C. Nobile, M. De Giorgi, F. D. Sala, G. Morello, P. Pompa, M. Hytch, E. Snoeck, A. Fiore, et al., "Synthesis and micrometer-scale assembly of colloidal CdSe/CdS nanorods Prepared by a Seeded Growth Approach," *Nano Lett.* **7**(10), 2942–2950 (2007) [doi:10.1021/nl0717661].

[4] R. Krahne, G. Morello, A. Figuerola, C. George, S. Deka, and L. Manna, "Physical properties of elongated inorganic nanoparticles," *Physics Reports*, 1–147, Elsevier B.V. (2011) [doi:10.1016/j.physrep.2011.01.001].

[5] I. Moreels, G. Rainò, R. Gomes, Z. Hens, T. Stöferle, and R. F. Mahrt, "Band-edge exciton fine structure of small, nearly spherical colloidal CdSe/ZnS quantum dots," *ACS Nano*, 110930161304003 (2011) [doi:10.1021/nn202604z].

[6] M. Furis, H. Htoon, M. Petruska, V. Klimov, T. Barrick, and S. Crooker, "Bright-exciton fine structure and anisotropic exchange in CdSe nanocrystal quantum dots," *Phys. Rev. B* **73**(24) (2006) [doi:10.1103/PhysRevB.73.241313].

[7] V. I. Klimov, D. W. McBranch, and M. G. Bawendi, "Electron and hole relaxation pathways in semiconductor quantum dots," *Phys. Rev. B* **60**(19), 13740 (1999).

[8] C. de Mello Donegá, M. Bode, and A. Meijerink, "Size- and temperature-dependence of exciton lifetimes in CdSe quantum dots," *Phys. Rev. B* **74**(8) (2006) [doi:10.1103/PhysRevB.74.085320].

[9] F. Pisanello, L. Martiradonna, P. Spinicelli, A. Fiore, J. P. Hermier, L. Manna, R. Cingolani, E. Giacobino, M. De Vittorio, et al., "Dots in rods as polarized single photon sources," *Superlattices and Microstructures* **47**(1), 165–169, Elsevier Ltd

(2010) [doi:10.1016/j.spmi.2009.06.009].

[10] R. Espiau de Lamaëstre, H. Bernas, D. Pacifici, G. Franzó, and F. Priolo, "Evidence for a 'dark exciton' state of PbS nanocrystals in a silicate glass," *Appl. Phys. Lett.* **88**(18), 181115 (2006) [doi:10.1063/1.2201885].

[11] I. Moreels, K. Lambert, D. Smeets, D. De Muynck, T. Nollet, J. C. Martins, F. Vanhaecke, A. Vantomme, C. Delerue, et al., "Size-dependent optical properties of colloidal PbS quantum dots," *ACS Nano* **3**(10), 3023–3030 (2009) [doi:10.1021/nn900863a].

[12] J. M. An, A. Franceschetti, and A. Zunger, "The excitonic exchange splitting and radiative lifetime in PbSe quantum dots," *Nano Lett.* **7**(7), 2129–2135 (2007) [doi:10.1021/nl071219f].

[13] W. Ma, S. L. Swisher, T. Ewers, J. Engel, V. E. Ferry, H. A. Atwater, and A. P. Alivisatos, "Photovoltaic performance of ultrasmall PbSe quantum dots," *ACS Nano*, 111003095248002 (2011) [doi:10.1021/nn202786g].

[14] B. Sun, A. T. Findikoglu, M. Sykora, D. J. Werder, and V. I. Klimov, "Hybrid photovoltaics based on semiconductor nanocrystals and amorphous silicon," *Nano Lett.* **9**(3), 1235–1241 (2009) [doi:10.1021/nl9001469].

[15] J. Seo, M. J. Cho, D. Lee, A. N. Cartwright, and P. N. Prasad, "Efficient heterojunction photovoltaic cell utilizing nanocomposites of lead sulfide nanocrystals and a low-bandgap polymer," *Adv. Mater.* **23**(34), 3984–3988 (2011) [doi:10.1002/adma.201101912].

[16] A. J. Shields, "Semiconductor quantum light sources," *Nature Photon* **1**(4), 215–223 (2007) [doi:10.1038/nphoton.2007.46].

[17] S. Chanyawadee, P. G. Lagoudakis, R. T. Harley, M. D. B. Charlton, D. V. Talapin, H. W. Huang, and C.-H. Lin, "Increased color-conversion efficiency in hybrid light-emitting diodes utilizing non-radiative energy transfer," *Adv. Mater.* **22**(5), 602–606 (2010) [doi:10.1002/adma.200902262].

[18] G. Konstantatos, L. Levina, A. Fischer, and E. H. Sargent, "Engineering the temporal response of photoconductive photodetectors via selective introduction of surface trap states," *Nano Lett.* **8**(5), 1446–1450 (2008) [doi:10.1021/nl080373e].

[19] G. Konstantatos and E. H. Sargent, "Nanostructured materials for photon detection,"

Nature Nanotechnology **5**(6), 391–400, Nature Publishing Group (2010) [doi:10.1038/nnano.2010.78].

[20] G. Konstantatos and E. H. Sargent, "PbS colloidal quantum dot photoconductive photodetectors: Transport, traps, and gain," *Appl. Phys. Lett.* **91**(17), 173505 (2007) [doi:10.1063/1.2800805].

[21] G. Konstantatos, J. Clifford, L. Levina, and E. H. Sargent, "Sensitive solution-processed visible-wavelength photodetectors," *Nature Photon* **1**(9), 531–534 (2007) [doi:10.1038/nphoton.2007.147].

[22] Y. P. Rakovich and J. F. Donegan, "Photonic atoms and molecules," *Laser Photon. Rev.* **4**(2), 179–191 (2009) [doi:10.1002/lpor.200910001].

[23] W. J. Parak, T. Pellegrino, and C. Plank, "Labelling of cells with quantum dots," *Nanotechnology* **16**(2), R9–R25 (2005) [doi:10.1088/0957-4484/16/2/R01].

[24] G. Iyer, X. Michalet, Y.-P. Chang, F. F. Pinaud, S. E. Matyas, G. Payne, and S. Weiss, "High affinity scFv−Hapten pair as a tool for quantum dot labeling and tracking of single proteins in live cells," *Nano Lett.* **8**(12), 4618–4623 (2008) [doi:10.1021/nl8032284].

[25] B. Y. S. Kim, W. Jiang, J. Oreopoulos, C. M. Yip, J. T. Rutka, and W. C. W. Chan, "Biodegradable quantum dot nanocomposites enable live cell labeling and imaging of cytoplasmic targets," *Nano Lett.* **8**(11), 3887–3892 (2008) [doi:10.1021/nl802311t].

[26] J. M. Klostranec and W. C. W. Chan, "Quantum dots in biological and biomedical research: recent progress and present challenges," *Adv. Mater.* **18**(15), 1953–1964 (2006) [doi:10.1002/adma.200500786].

[27] X. Michalet, "Quantum dots for live cells, in vivo imaging, and diagnostics," *Science* **307**(5709), 538–544 (2005) [doi:10.1126/science.1104274].

[28] A. P. Alivisatos, W. Gu, and C. Larabell, "Quantum dots as cellular probes," *Annu. Rev. Biomed. Eng.* **7**(1), 55–76 (2005) [doi:10.1146/annurev.bioeng.7.060804.100432].

[29] S. Lu and A. Madhukar, "Nonradiative resonant excitation transfer from nanocrystal quantum dots to adjacent quantum channels," *Nano Lett.* **7**(11), 3443–3451 (2007) [doi:10.1021/nl0719731].

[30] M. Califano, A. Zunger, and A. Franceschetti, "Direct carrier multiplication due to inverse Auger scattering in CdSe quantum dots," *Appl. Phys. Lett.* **84**(13), 2409 (2004)

[doi:10.1063/1.1690104].

[31] M. T. Trinh, L. Polak, J. M. Schins, A. J. Houtepen, R. Vaxenburg, G. I. Maikov, G. Grinbom, A. G. Midgett, J. M. Luther, et al., "Anomalous independence of multiple exciton generation on different group IV−VI quantum dot architectures," *Nano Lett.* **11**(4), 1623–1629 (2011) [doi:10.1021/nl200014g].

[32] R. D. Schaller, V. M. Agranovich, and V. I. Klimov, "High-efficiency carrier multiplication through direct photogeneration of multi-excitons via virtual single-exciton states," *Nat Phys* **1**(3), 189–194 (2005) [doi:10.1038/nphys151].

[33] S. Deka, A. Quarta, M. G. Lupo, A. Falqui, S. Boninelli, C. Giannini, G. Morello, M. De Giorgi, G. Lanzani, et al., "CdSe/CdS/ZnS double shell nanorods with high photoluminescence efficiency and their exploitation as biolabeling probes," *J. Am. Chem. Soc.* **131**(8), 2948–2958 (2009) [doi:10.1021/ja808369e].

[34] R. R. Lunt, T. P. Osedach, P. R. Brown, J. A. Rowehl, and V. Bulović, "Practical roadmap and limits to nanostructured photovoltaics," *Adv. Mater.* 23(48), 5712-5727 (2011) [doi:10.1002/adma.201103404].

[35] H. A. Atwater and A. Polman, "Plasmonics for improved photovoltaic devices," *Nature Publishing Group* **9**(3), 205–213, Nature Publishing Group (2010) [doi:10.1038/nmat2629].

[36] D. Aspnes and A. Studna, "Dielectric functions and optical-parameters of Si, Ge, Gap, Gaas, Gasb, Inp, Inas, and Insb From 1.5 to 6.0 Ev," *Phys. Rev. B* **27**(2), 985–1009 (1983).

[37] V. M. Agranovich, Y. N. Gartstein, and M. Litinskaya, "Hybrid resonant organic–inorganic nanostructures for optoelectronic applications," *Chem. Rev.* **111**(9), 5179–5214 (2011) [doi:10.1021/cr100156x].

[38] D. D. L Dexter, "Two ideas on energy transfer phenomena Ion-pair effects involving the OH stretching mode and sensitization of photovoltaic cells," *Journal of Luminescence*, North-Holland Publishing Company, Ed., 779–784 (1979).

[39] R. M. Clegg, *Chapter 1 "Forster resonance energy transfer-FRET what is it, why do it, and how it's done"*, 1st ed., in *Fret and Flim Techniques* **33**, 1st ed., pp. 1–57, Elesvier B.V. (2009) [doi:10.1016/S0075-7535(08)00001-6].

[40] S. Chanyawadee, R. Harley, M. Henini, D. Talapin, and P. Lagoudakis, "Photocurrent

enhancement in hybrid nanocrystal quantum-dot p-i-n photovoltaic devices," *Phys Rev Lett* **102**(7) (2009) [doi:10.1103/PhysRevLett.102.077402].

[41] S. Lu, Z. Lingley, T. Asano, D. Harris, T. Barwicz, S. Guha, and A. Madhukar, "Photocurrent induced by nonradiative energy transfer from nanocrystal quantum dots to adjacent silicon nanowire conducting channels: Toward a new solar cell paradigm," *Nano Lett.* **9**(12), 4548–4552 (2009) [doi:10.1021/nl903104k].

[42] A. V. Malko, A. A. Mikhailovsky, M. A. Petruska, J. A. Hollingsworth, H. Htoon, M. G. Bawendi, and V. I. Klimov, "From amplified spontaneous emission to microring lasing using nanocrystal quantum dot solids," *Appl. Phys. Lett.* **81**(7), 1303 (2002) [doi:10.1063/1.1497708].

[43] V. I. Klimov, "Optical gain and stimulated emission in nanocrystal quantum dots," *Science* **290**(5490), 314–317 (2000) [doi:10.1126/science.290.5490.314].

[44] V. I. Klimov, S. A. Ivanov, J. Nanda, M. Achermann, I. Bezel, J. A. McGuire, and A. Piryatinski, "Single-exciton optical gain in semiconductor nanocrystals," *Nature* **447**(7143), 441–446 (2007) [doi:10.1038/nature05839].

[45] M. Saba, S. Minniberger, F. Quochi, J. Roither, M. Marceddu, A. Gocalinska, M. V. Kovalenko, D. V. Talapin, W. Heiss, et al., "Exciton-exciton interaction and optical gain in colloidal CdSe/CdS dot/rod nanocrystals," *Adv. Mater.* **21**(48), 4942–4946 (2009) [doi:10.1002/adma.200901482].

[46] M. Marceddu, M. Saba, F. Quochi, A. Lai, J. Huang, D. V. Talapin, A. Mura, and G. Bongiovanni, "Charged excitons, Auger recombination and optical gain in CdSe/CdS nanocrystals," *Nanotechnology* **23**(1), 015201 (2011) [doi:10.1088/0957-4484/23/1/015201].

[47] D. Bimberg and U. W. Pohl, "Quantum dots: promises and accomplishments," *Materials Today* **14**(9), 388–397, Elsevier Ltd (2011) [doi:10.1016/S1369-7021(11)70183-3].

[48] M. V. Artemyev, U. Woggon, R. Wannemacher, H. Jaschinski, and W. Langbein, "Light trapped in a photonic dot: Microspheres act as a cavity for quantum dot emission," *Nano Lett.* **1**(6), 309–314 (2001) [doi:10.1021/nl015545l].

[49] J. Schäfer, J. P. Mondia, R. Sharma, Z. H. Lu, A. S. Susha, A. L. Rogach, and L. J. Wang, "Quantum dot microdrop laser," *Nano Lett.* **8**(6), 1709–1712 (2008)

[doi:10.1021/nl080661a].

[50] Y. Chan, J. S. Steckel, P. T. Snee, J. M. Caruge, J. M. Hodgkiss, D. G. Nocera, and M. G. Bawendi, "Blue semiconductor nanocrystal laser," *Appl. Phys. Lett.* **86**(7), 073102 (2005) [doi:10.1063/1.1863445].

[51] H.-J. Eisler, V. C. Sundar, M. G. Bawendi, M. Walsh, H. I. Smith, and V. Klimov, "Color-selective semiconductor nanocrystal laser," *Appl. Phys. Lett.* **80**(24), 4614 (2002) [doi:10.1063/1.1485125].

[52] Y. Chan, J. M. Caruge, P. T. Snee, and M. G. Bawendi, "Multiexcitonic two-state lasing in a CdSe nanocrystal laser," *Appl. Phys. Lett.* **85**(13), 2460 (2004) [doi:10.1063/1.1795368].

[53] J. Xu and M. Xiao, "Lasing action in colloidal CdS/CdSe/CdS quantum wells," *Appl. Phys. Lett.* **87**(17), 173117 (2005) [doi:10.1063/1.2119423].

[54] G. C. Righini, Y. Dumeige, P. Féron, M. Ferrari, G. Nunzi Conti, D. Ristic, and S. Soria, "Whispering gallery mode microresonators: Fundamentals and applications," *Rivista del Nuovo Cimento* **34**(7) (2011).

[55] P. T. Snee, Y. Chan, D. G. Nocera, and M. G. Bawendi, "Whispering-gallery-mode lasing from a semiconductor nanocrystal/microsphere resonator composite," *Adv. Mater.* **17**(9), 1131–1136 (2005) [doi:10.1002/adma.200401571].

[56] A. N. Oraevsky, "Whispering-gallery waves," *Quantum Electronics* **32**(5), 377–400, Turpion Ltd (2002).

[57] J. Ward and O. Benson, "WGM microresonators: sensing, lasing and fundamental optics with microspheres," *Laser Photon. Rev.* **5**(4), 553–570 (2011) [doi:10.1002/lpor.201000025].

[58] M. V. Artemyev and U. Woggon, "Quantum dots in photonic dots," *Appl. Phys. Lett.* **76**(11), 1353 (2000) [doi:10.1063/1.126029].

[59] N. A. Kotov, J. O. Winter, I. P. Clements, E. Jan, B. P. Timko, S. Campidelli, S. Pathak, A. Mazzatenta, C. M. Lieber, et al., "Nanomaterials for neural interfaces," *Adv. Mater.* **21**(40), 3970–4004 (2009) [doi:10.1002/adma.200801984].

[60] A. R. Bishop and R. G. Nuzzo, "Self-assembled monolayers: Recent developments and applications," *Current Opinion in Colloid & Interface Science* **1**(1), 127–136, Current Science Ltd. (1996) [doi:10.1016/S1359-0294(96)80053-7].

[61] M. S. Skolnick and D. J. Mowbray, "Self assembled semiconductor quantum dots: Fundamental physics and device applications," *Ann. Rev. Mater. Res.* **34**(1), 181–218 (2004) [doi:10.1146/annurev.matsci.34.082103.133534].

[62] D. Allara, "Critical issues in applications of self-assembled monolayers," presented at Biosensors & Bioelectronics, 1995, 771–783.

[63] S.-J. Yen, W.-L. Hsu, Y.-C. Chen, H.-C. Su, Y.-C. Chang, H. Chen, S.-R. Yeh, and T.-R. Yew, "The enhancement of neural growth by amino-functionalization on carbon nanotubes as a neural electrode," *Biosensors and Bioelectronics* **26**(10), 4124–4132, Elsevier B.V. (2011) [doi:10.1016/j.bios.2011.04.003].

[64] M. Ulbrich and P. Fromherz, "Neuron-silicon self-excitation: A prototype of iono-electronics," *Adv. Mater.* **13**(5), 344–347 (2001).

[65] A. Ferrari, M. Cecchini, A. Dhawan, S. Micera, I. Tonazzini, R. Stabile, D. Pisignano, and F. Beltram, "Nanotopographic control of neuronal polarity," *Nano Lett.* **11**(2), 505–511 (2011) [doi:10.1021/nl103349s].

[66] S. Turner, L. Kam, M. Isaacson, H. Craighead, W. Shain, and J. Turner, "Cell attachment on silicon nanostructures," presented at Journal of Vacuum Science & Technology B, 1997, 2848–2854.

[67] P. Fromherz, A. Offenhausser, T. Vetter, and J. Weis, "A neuron-silicon junction: a Retzius cell of the leech on an insulated-gate field-effect transistor," *Science* **252**(5010), 1290–1293 (1991).

[68] D. Braun and P. Fromherz, "Fast voltage transients in capacitive silicon-to-cell stimulation detected with a luminescent molecular electronic probe," *Phys Rev Lett* **86**(13), 2905–2908 (2001) [doi:10.1103/PhysRevLett.86.2905].

[69] D. Braun and P. Fromherz, "Imaging neuronal seal resistance on silicon chip using fluorescent voltage-sensitive dye," *Biophys J* **87**(2), 1351–1359 (2004) [doi:10.1529/biophysj.104.039990].

[70] A. Bouron, C. Becker, and H. Porzig, "Functional expression of voltage-gated Na^+ and Ca^{2+} channels during neuronal differentiation of PC12 cells with nerve growth factor or forskolin," *Naunyn-Schmiedebergs Arch. Pharmacol.* **359**(5), 370–377 (1999).

[71] K. Homma, Y. Kitamura, H. Ogawa, and K. Oka, "Serotonin induces the increase in intracellular Ca^{2+} that enhances neurite outgrowth in PC12 cells via activation of 5-

HT3 receptors and voltage-gated calcium channels," *J. Neurosci. Res.* **84**(2), 316–325 (2006) [doi:10.1002/jnr.20894].

[72] D. S. Peterka, H. Takahashi, and R. Yuste, "Imaging voltage in neurons," *Neuron* **69**(1), 9–21, Elsevier Inc. (2011) [doi:10.1016/j.neuron.2010.12.010].

[73] S. Mennerick, M. Chisari, H. J. Shu, A. Taylor, M. Vasek, L. N. Eisenman, and C. F. Zorumski, "Diverse voltage-sensitive dyes modulate GABAA receptor Function," *Journal of Neuroscience* **30**(8), 2871–2879 (2010) [doi:10.1523/JNEUROSCI.5607-09.2010].

[74] M. Canepari, K. Vogt, and D. Zecevic, "Combining voltage and calcium imaging from neuronal dendrites," *Cell Mol. Neurobiol* **28**(8), 1079–1093 (2008) [doi:10.1007/s10571-008-9285-y].

[75] K. Takagaki, M. T. Lippert, B. Dann, T. Wanger, and F. W. Ohl, "Normalization of Voltage-Sensitive Dye Signal with Functional Activity Measures," *PLoS ONE* **3**(12), H. D. Mansvelder, Ed., e4041 (2008) [doi:10.1371/journal.pone.0004041.g008].

[76] E. Neher and B. Sakmann, "Single-channel currents recorded from membrane of denervated frog muscle fibres.," *Nature* **260**(5554), 799–802 (1976).

[77] J. Huguenard, D. McCormick, and G. M. Shepherd, *Electrophysiology of the neuron*, Oxford University Press, USA (1994).

[78] A. L. Rogach, *Semiconductor nanocrystal quantum dots*, Springer Verlag (2008).

[79] V. I. Klimov, Ebooks Corporation, and M. D. Firma comercial, *Semiconductor and metal nanocrystals*, CRC Press (2003).

[80] S. V. Gaponenko, *Optical properties of semiconductor nanocrystals*, Cambridge Univ Pr (2005).

[81] R. Krahne, G. Morello, A. Figuerola, C. George, S. Deka, and L. Manna, "Physical properties of elongated inorganic nanoparticles," *Physics Reports*, **501**(3-5) 1–147, Elsevier B.V. (2011) [doi:10.1016/j.physrep.2011.01.001].

[82] A. L. Efros and M. Rosen, "The Electronic structure of semiconductor nanocrystals 1," *Annual Review of Materials Science* **30**(1), 475–521, Annual Reviews 4139 El Camino Way, PO Box 10139, Palo Alto, CA 94303-0139, USA (2000).

[83] I. Kang and F. Wise, "Electronic structure and optical properties of PbS and PbSe quantum dots," *J Opt Soc Am B* **14**(7), 1632–1646 (1997).

[84] J. T. Verdeyen, *Laser Electronics (3rd Edition)*, 3rd ed., Prentice Hall (1995).

[85] R. Kraus, P. Lagoudakis, A. Rogach, D. Talapin, H. Weller, J. Lupton, and J. Feldmann, "Room-temperature exciton storage in elongated semiconductor nanocrystals," *Phys Rev Lett* **98**(1) (2007) [doi:10.1103/PhysRevLett.98.017401].

[86] J. Müller, J. M. Lupton, P. G. Lagoudakis, F. Schindler, R. Koeppe, A. L. Rogach, J. Feldmann, D. V. Talapin, and H. Weller, "Wave function engineering in elongated semiconductor nanocrystals with heterogeneous carrier confinement," *Nano Lett.* **5**(10), 2044–2049 (2005) [doi:10.1021/nl051596x].

[87] J. R. Lakowicz, *Principles of fluorescence spectroscopy*, Springer Verlag (2006).

[88] T. Yoshie, L. Tang, and S.-Y. Su, "Optical microcavity: Sensing down to single molecules and atoms," *Sensors* **11**(2), 1972–1991 (2011) [doi:10.3390/s110201972].

[89] A. Schliesser and T. J. Kippenberg, "Cavity optomechanics with whispering-gallery-mode optical micro-resonators," in *arXiv* **quant-ph** (2010).

[90] T. M. Benson, S. V. Boriskina, P. Sewell, A. Vukovic, S. C. Greedy, and A. I. Nosich, "Micro-optical resonators for microlasers and integrated optoelectronics: recent advances and future challenges," in *arXiv* **physics.optics** (2006).

[91] Matsko, AB, A. Savchenkov, D. Strekalov, V. ILCHENKO, and L. Maleki, "Review of applications of whispering-gallery mode resonators in photonics and nonlinear optics," *IPN Progress Report* **42**, 162 (2005).

[92] M. Gorodetsky and V. Ilchenko, "High-optical whispering-gallery microresonators - Precession Approach for Spherical Mode Analysis and Emission Patterns with Prism Couplers," *Optics Communications* **113**, 133–143 (1994).

[93] A. B. Matsko and V. S. Ilchenko, "Optical resonators with whispering-gallery modes-part I: basics," *IEEE J. Sel. Top. Quantum Electron.* **12**(1), 3–14, IEEE (2006).

[94] S. A. McDonald, P. W. Cyr, L. Levina, and E. H. Sargent, "Photoconductivity from PbS-nanocrystal⁄semiconducting polymer composites for solution-processible, quantum-size tunable infrared photodetectors," *Appl. Phys. Lett.* **85**(11), 2089 (2004) [doi:10.1063/1.1792380].

[95] K. Yum, S. Na, Y. Xiang, N. Wang, and M.-F. Yu, "Mechanochemical delivery and dynamic tracking of fluorescent quantum dots in the cytoplasm and nucleus of living cells," *Nano Lett.* **9**(5), 2193–2198 (2009) [doi:10.1021/nl901047u].

[96] K.-T. Yong, H. Ding, I. Roy, W.-C. Law, E. J. Bergey, A. Maitra, and P. N. Prasad, "Imaging pancreatic cancer using bioconjugated InP quantum dots," *ACS Nano* **3**(3), 502–510 (2009) [doi:10.1021/nn8008933].

[97] L. Bahshi, R. Freeman, R. Gill, and I. Willner, "Optical detection of glucose by means of metal nanoparticles or semiconductor quantum dots," *Small* **5**(6), 676–680 (2009) [doi:10.1002/smll.200801403].

[98] C. Wu, B. Bull, C. Szymanski, K. Christensen, and J. McNeill, "Multicolor conjugated polymer dots for biological fluorescence imaging," *ACS Nano* **2**(11), 2415–2423 (2008) [doi:10.1021/nn800590n].

[99] F. W. Wise, "Lead salt quantum dots: the limit of strong quantum confinement," *Acc. Chem. Res.* **33**(11), 773–780 (2000) [doi:10.1021/ar970220q].

[100] R. J. Ellingson, M. C. Beard, J. C. Johnson, P. Yu, O. I. Micic, A. J. Nozik, A. Shabaev, and A. L. Efros, "Highly efficient multiple exciton generation in colloidal PbSe and PbS quantum dots," *Nano Lett.* **5**(5), 865–871 (2005) [doi:10.1021/nl0502672].

[101] D. J. Farrell, Y. Takeda, K. Nishikawa, T. Nagashima, T. Motohiro, and N. J. Ekins-Daukes, "A hot-carrier solar cell with optical energy selective contacts," *Appl. Phys. Lett.* **99**(11), 111102 (2011) [doi:10.1063/1.3636401].

[102] S. S. Sahay and S. Majumdar, "A review of biofunctionalization of nanomaterials", Challa Kumar (Ed.) (2009).

[103] O. Chen, Y. Yang, T. Wang, H. Wu, C. Niu, J. Yang, and Y. C. Cao, "Surface-functionalization-dependent optical properties of II–VI semiconductor nanocrystals," *J. Am. Chem. Soc.* **133**(43), 17504–17512 (2011) [doi:10.1021/ja208337r].

[104] L. Turyanska, A. Patanè, M. Henini, B. Hennequin, and N. R. Thomas, "Temperature dependence of the photoluminescence emission from thiol-capped PbS quantum dots," *Appl. Phys. Lett.* **90**(10), 101913 (2007) [doi:10.1063/1.2711529].

[105] "Guide to streak cameras," *Hamamatsu*, 1–12 (2008).

[106] M. Gaponenko, A. Lutich, N. Tolstik, A. Onushchenko, A. Malyarevich, E. Petrov, and K. Yumashev, "Temperature-dependent photoluminescence of PbS quantum dots in glass: Evidence of exciton state splitting and carrier trapping," *Phys. Rev. B* **82**(12) (2010) [doi:10.1103/PhysRevB.82.125320].

[107] J. I. Pankove, *Optical processes in semiconductors*, Dover Publications (1971).

[108] A. Alivisatos, M. Arndt, and S. Efrima, "Electronic energy transfer at semiconductor interfaces. I. Energy transfer from two‐dimensional molecular films to Si (111)," *The Journal of chemical* **86**(11),.6540-6549 (1987).

[109] D. Basko, V. Agranovich, F. Bassani, and G. La Rocca, "Energy transfer from a semiconductor quantum dot to an organic matrix," presented at Physica Status Solidi a-Applications and Materials Science, 2000, 69–72.

[110] R. M. Kraus, P. G. Lagoudakis, J. Müller, A. L. Rogach, J. M. Lupton, J. Feldmann, D. V. Talapin, and H. Weller, "Interplay between Auger and ionization processes in nanocrystal quantum dots," *J. Phys. Chem. B* **109**(39), 18214–18217 (2005) [doi:10.1021/jp053671y].

[111] G. Brambilla, V. Finazzi, and D. Richardson, "Ultra-low-loss optical fiber nanotapers," *Opt Express* **12**(10), 2258–2263, Optical Society of America (2004).

[112] W. von Klitzing, R. Long, V. S. Ilchenko, J. Hare, and V. Lefevre-Seguin, "Frequency tuning of the whispering gallery modes of silica microspheres for CQED and spectroscopy," in *arXiv* **quant-ph** (2000) [doi:10.1364/OL.26.000166].

[113] A. Chiba, H. Fujiwara, J.-I. Hotta, S. Takeuchi, and K. Sasaki, "Resonant frequency control of a microspherical cavity by temperature adjustment,". *J. Appl. Phys.* **43**(9A), 6138–6141 (2004) [doi:10.1143/JJAP.43.6138].

[114] S. Spillane, T. Kippenberg, O. Painter, and K. Vahala, "Ideality in a Fiber-Taper-coupled microresonator system for application to cavity quantum electrodynamics," *Phys Rev Lett* **91**(4) (2003) [doi:10.1103/PhysRevLett.91.043902].

[115] D. Bäuerle, *Laser processing and chemistry (Advanced Texts in Physics)*, 3rd ed., Springer (2000).

[116] W. M. Cowan and E. R. Kandel, "Prospects for neurology and psychiatry.," *JAMA* **285**(5), 594–600 (2001).

[117] "Magnetic resonance imaging: physical principles and sequence design - E. Mark Haacke - Google Books" (2012).

[118] M. E. Raichle, "Positron emission tomography," *Annual review of neuroscience* **6**(1), 249–267, Annual Reviews 4139 El Camino Way, PO Box 10139, Palo Alto, CA 94303-0139, USA (1983).

[119] G. Muehllehner and J. S. Karp, "Positron emission tomography," *Phys. Med. Biol.* **51**(13), R117–R137 (2006) [doi:10.1088/0031-9155/51/13/R08].

[120] G. J. Stuart and L. M. Palmer, "Imaging membrane potential in dendrites and axons of single neurons," *Pflugers Arch - Eur J Physiol* **453**(3), 403–410 (2006) [doi:10.1007/s00424-006-0149-3].

[121] R. Fujii, M. Ichikawa, and M. Ozaki, "Imaging of molecular dynamics regulated by electrical activities in neural circuits and in synapses," *Neurosignals* **16**(4), 260–277 (2008) [doi:10.1159/000123037].

[122] L. A. Greene and A. S. Tischler, "Establishment of a noradrenergic clonal line of rat adrenal pheochromocytoma cells which respond to nerve growth-factor" *Proc. Natl. Acad. Sci. U. S. A.* **73**(7), 2424–2428 (1976).

[123] M. Buttiglione, F. Vitiello, E. Sardella, L. Petrone, M. Nardulli, P. Favia, R. d'Agostino, and R. Gristina, "Behaviour of SH-SY5Y neuroblastoma cell line grown in different media and on different chemically modified substrates," *Biomaterials* **28**(19), 2932–2945 (2007) [doi:10.1016/j.biomaterials.2007.02.022].

[124] V. M. Fridkin, *Ferroelectric semiconductors*, 1st ed., Springer (1980).

[125] E. L. Wooten, K. M. Kissa, A. Yi-Yan, E. J. Murphy, D. A. Lafaw, P. F. Hallemeier, D. Maack, D. V. Attanasio, D. J. Fritz, et al., "A review of lithium niobate modulators for fiber-optic communications systems," *IEEE J. Sel. Top. Quantum Electron.* **6**(1), 69–82 (2000).

[126] L. E. Myers and W. R. Bosenberg, "Periodically poled lithium niobate and quasi-phase-matched optical parametric oscillators," *IEEE J. Quantum Electron.* **33**(10), 1663–1672 (1997).

[127] D. Yudistira, S. Benchabane, D. Janner, and V. Pruneri, "Surface acoustic wave generation in ZX-cut LiNbO[sub 3] superlattices using coplanar electrodes," *Appl. Phys. Lett.* **95**(5), 052901 (2009) [doi:10.1063/1.3190518].

[128] M. E. Lines and A. M. Glass, *Principles and applications of ferroelectrics and related materials*, Clarendon Press, Oxford (1977).

[129] V. Gopalan and M. C. Gupta, "Origin and characteristics of internal fields in LiNbO 3crystals," *Ferroelectrics* **198**(1), 49–59 (1997) [doi:10.1080/00150199708228337].

[130] S. Elliott and S. R. Elliott, *The physics and chemistry of solids*, John Wiley & Sons Inc

(1998).

[131] K. G. Karapetyan, A. A. Kteyan, and R. A. Vardanyan, "Thermal reduction effect on Curie temperature of $LiNbO_3$ ferroelectrics," *Solid State Communications* **140**(9-10), 474–476 (2006) [doi:10.1016/j.ssc.2006.08.045].

[132] V. Gopalan, V. Dierolf, and D. A. Scrymgeour, "Defect–domain wall Interactions in trigonal ferroelectrics," *Annu. Rev. Mater. Res.* **37**(1), 449–489 (2007) [doi:10.1146/annurev.matsci.37.052506.084247].

[133] E. Kandel and J. Schwartz, *Neuroscience and behavior* (1999).

[134] J. E. Dowling, *Neurons and networks*, Belknap Press (2001).

[135] Y. Huang and P. Chen, "Nanoelectronic biosensing of dynamic cellular activities based on nanostructured materials," *Adv. Mater.* **22**(25), 2818–2823 (2010) [doi:10.1002/adma.200904235].

[136] J. G. Nicholls, A. R. Martin, P. A. Fuchs, D. A. Brown, and M. E. Diamond, "*From neuron to brain"*, Sinauer Associates (2011).

[137] C. L. Sones, A. C. Muir, Y. J. Ying, S. Mailis, R. W. Eason, T. Jungk, A. Hoffmann, and E. Soergel, "Precision nanoscale domain engineering of lithium niobate via UV laser induced inhibition of poling," *Appl. Phys. Lett.* **92**(7), 072905 (2008) [doi:10.1063/1.2884185].

[138] N. Niizeki, T. Yamada, and H. Toyoda, "Growth ridges, etched hillocks, and crystal structure of lithium niobate," *Jap. J. Appl. Phys* **6**, 318–327 (1967).

[139] S. Mailis, C. Riziotis, I. T. Wellington, P. G. R. Smith, C. B. E. Gawith, and R. W. Eason, "Direct ultraviolet writing of channel waveguides in congruent lithium niobate single crystals.," *Opt Lett* **28**(16), 1433–1435 (2003).

[140] C. E. Valdivia, C. L. Sones, J. G. Scott, S. Mailis, R. W. Eason, D. A. Scrymgeour, V. Gopalan, T. Jungk, E. Soergel, et al., "Nanoscale surface domain formation on the +z face of lithium niobate by pulsed ultraviolet laser illumination," *Appl. Phys. Lett.* **86**(2), 022906 (2005) [doi:10.1063/1.1849414].

[141] S. Mailis, "UV laser induced ferroelectric domain inversion in lithium niobate single crystals," *J. Opt.* **12**(9) (2010) [doi:10.1088/2040-8978/12/9/095601].

[142] J. Gartlon, A. Kinsner, A. Bal-Price, S. Coecke, and R. H. Clothier, "Evaluation of a proposed in vitro test strategy using neuronal and non-neuronal cell systems for

detecting neurotoxicity," *Toxicol. Vitro* **20**(8), 1569–1581 (2006) [doi:10.1016/j.tiv.2006.07.009].

[143] W.-C. Yang, B. J. Rodriguez, A. Gruverman, and R. J. Nemanich, "Photo electron emission microscopy of polarity-patterned materials," *J. Phys.: Condens. Matter* **17**(16), S1415–S1426 (2005) [doi:10.1088/0953-8984/17/16/012].

[144] X. Liu, K. Kitamura, and K. Terabe, "Surface potential imaging of nanoscale LiNbO[sub 3] domains investigated by electrostatic force microscopy," *Appl. Phys. Lett.* **89**(13), 132905 (2006) [doi:10.1063/1.2358115].

[145] C. Xie, L. Hanson, W. Xie, Z. Lin, B. Cui, and Y. Cui, "Noninvasive neuron pinning with nanopillar arrays," *Nano Lett.* **10**(10), 4020–4024 (2010) [doi:10.1021/nl101950x].

[146] T.-I. Chao, S. Xiang, J. F. Lipstate, C. Wang, and J. Lu, "Poly(methacrylic acid)-grafted carbon nanotube scaffolds enhance differentiation of hESCs into neuronal cells," *Adv. Mater.* **22**(32), 3542–3547 (2010) [doi:10.1002/adma.201000262].

[147] S. Kalinin and D. Bonnell, "Local potential and polarization screening on ferroelectric surfaces," *Phys. Rev. B* **63**(12) (2001) [doi:10.1103/PhysRevB.63.125411].